Alma Mater Studiorum – Università di Bologna

DOTTORATO DI RICERCA IN

CHIMICA

XXX Ciclo

Settore Concorsuale: 03/A2

Settore Scientifico Disciplinare: CHIM/02

Modelling of materials for organic electronics:

Nanoscale morphology, interfaces and charge transport properties

Presentata da: Andrea Lorenzoni

Coordinatore Dottorato

Prof. Aldo Roda

Supervisore

Prof. Claudio Zannoni

Co-Supervisore

Dr. Francesco Mercuri

Esame finale anno 2018

"*DON'T PANIC*"

Douglas N. Adams - The Hitchhiker's Guide to the Galaxy

Abstract

Progress in the development of advanced and multi-functional materials for organic and hybrid electronic and optoelectronic devices is often hampered by the lack of a detailed understanding of structure/property relationships, and especially of the link between molecular structure, nanoscale aggregation and electronic properties. This issue affects particularly interfaces among molecular layers in thin-film materials for organic devices, where the chemico-physical complexity of the system leads to difficult interpretation of experimental results.

The overall performance of the organic electronic and optoelectronic devices are related to the charge transport properties of the materials constituting the active layer, which, in turn, depend on the morphology at the interface between the layers. These properties are affected by several factors, such as the fabrication parameters, processing, and the interactions between the materials composing the layers.

In this thesis, the development of computational tools able to model the nanoscale morphology and the electronic properties of materials, in realistic environments, targeting specific interfaces for organic electronics, is outlined. These tools make use of methods at different scales, based on molecular dynamics (MD), density functional theory (DFT) and coarse-grain (CG) simulations. In this regard, high performance computing (HPC) infrastructures enable the widening of the domain of each method, allowing the simulation of large-scale systems.

In particular, MD simulations were performed for the modelling of materials used in organic electronic and optoelectronic devices, including organic semiconductors based on small molecules, polymer dielectrics, electrodes and 2D materials, investigating the growth and aggregation of organic materials and layered systems at the interfaces. These morphologies were then used to investigate electronic properties occurring between materials by performing DFT calculations. The CG method allows the extension of the length and time scales of the systems under investigation.

The approach proposed in this thesis enables a better understanding on the aggregation of organic materials in complex environments and the related electronic processes, by mimicking realistic processing techniques, and finally correlating the results with experiments.

Acknowledgements

The work presented in this thesis is the result of the last three years efforts (both computational and personal). This was possible thanks to, above all, some very important people, to which I would like to express my infinite gratitude.

First of all, I would like to thank Dr. Michele Muccini for giving me the opportunity to work in a multidisciplinary, evolving and stimulating research environment, always with his maximum support.

My heartfelt thanks to my supervisor, Prof. Claudio Zannoni, for his support, the fruitful scientific discussions and for always following me closely during my PhD, trying to find new ideas for my research activities.

A special thanks to Dr. Francesco Mercuri, for being a fundamental and constant presence before and during my PhD, and an integral part of all my work and publications. He always gave me his maximum support, he urged me to continually improve myself, contributing crucially to my scientific and computational evolution, teaching me never to stop at the surface of a problem (and nor at the interface). He gave me the opportunity to travel a lot during these years, allowing me to learn as much as possible by meeting other researchers from the rest of the world. He always left me a lot of freedom in developing my research ideas, and this thesis is the irrefutable proof. Without him, all this work would not have been possible.

Many thanks to Dr. Matteo Baldoni, for his great scientific and personal support, his patience and his continuous help during the last year. Even though I met him at the end of my PhD, he has been fundamental for my research.

I would like to thank the Computational Nanoscience group of the University of Nottingham, where I spent three months during my PhD. In particular, I would like to thank Prof. Elena Besley, for the opportunity to undertake a period of research abroad, very useful for my personal and scientific growth, and for her stimulating and contagious enthusiasm.

I would like to express my gratitude to all the collaborators whom, with their expertise, contributed decisively to my work, namely Alessandro Pecchia, Adriano Mosca Conte, Federico Gallino, Lara Querciagrossa, and to all my colleagues within the ISMN institute of CNR in Bologna.

Many thanks to the H2020 project MOSTOPHOS for funding, and especially to the coordinator, Prof. Denis Andrienko, for the scientific discussions and for his interest in my research activities.

I would also like to acknowledge the CINECA computing center and the PRACE initiative, for the availability of high performance computing resources and support.

Finally, I would like to thank my family, for their constant support.

Contents

Chapter 1

Introduction

Since the discovery, in 1977, that the conductivity of polyacetylene increases by several orders of magnitude upon doping with iodine[1], organic electronics attracted a lot of interest and research efforts. For this pioneering work and further research on conducting polymers, Heeger, MacDiarmid and Shirakawa were awarded with the Nobel prize in Chemistry in 2000. The first organic device was fabricated ten years later, in 1987, by C. W. Tang, who built a prototypical bilayer OLED device[2]. In the same year, Koezuka and co-workers reported the first organic field-effect transistor based on polythiophene[3]. The research on organic electronic devices raised and, with that, their application in common objects, like smartphones, TV and medical devices. The increased interest in organic devices is due to manifold factors. Firstly, the increased sensitivity towards social and energetic issues related to the use of non-renewable and difficult to extract inorganic materials, like silicon and lithium, commonly used for displays and batteries. Moreover, organic-based devices show a series of appealing features which can allow them to compete with their inorganic counterpart, such as the possibility to realize flexible large-area devices based on thin films, constituted by cheap, highly tunable materials. Organic materials can be bio-compatible, enabling applications concerning the interaction between organic devices and biological systems.

The main drawbacks of organic electronics, however, reside in the lower lifetimes of materials, due to degradation processes occurring when exposed to air and water, leading to lower charge transport properties and hence to lower efficiency and performance of the devices[4–8]. Nowadays, the research is focused on the improvement and enhancement of the materials composing the building blocks of the organic devices, in order to obtain better performance[9–12]. Above all, the research on these devices is not focused on the replacement of inorganic devices, but rather to fabricate devices for a range of applications in which the inorganic materials cannot be used. For example, sensors for health care, large-area low-consumption lighting devices, flexible devices, wearable electronics, bioelectronics[13–19].

The overall performance of the organic electronic devices are generally related to the morphological and charge transport properties of the semiconducting materials constituting the active layers. These two properties are tightly correlated. In fact, is now well known that charge transport in organic materials depends crucially on the molecular nanoscale morphology of materials in aggregates[10, 20–22]. These factors, in turn, are related to the device architecture, processing techniques, and physicochemical interactions with the environment

and other materials, occurring, for example, at the interfaces[23]. In particular, remarkable electronic and optical performances in organic devices can be achieved by active layers constituted by thin-films of crystalline or polycrystalline organic materials, where the growth of ordered aggregates is a prerequisite for optimal efficiencies[5, 6, 24, 25]. The potential occurrence of polymorphism in the formation of organic crystal aggregates, may impact further the overall device performances[26–28]. The relationship between the directionality and anisotropy of nanoscale crystalline aggregation and charge transport properties is particularly relevant in planar devices, such as organic transistors, where charge accumulation is essentially connected to the organic layers at the semiconductor/dielectric interface[6, 20, 29]. Accordingly, the properties of these devices depend critically on aggregation properties and crystallinity in the pseudo-bidimensional layers constituting the active thin-film[6, 20, 25]. Detailed investigations on aggregation phenomena in layered organic semiconductors and the link with charge transport properties constitute an essential element for the optimisation of devices and the comprehensive understanding of structure/property relationships.

The aggregation and crystallinity of organic layers is also greatly affected by the interaction with the underlying surface on which they are grown. Namely, the nature of the interactions between the materials at the interface, the morphology of the underlying surface, the deposition technique and parameters, dictate the morphology of the organic materials aggregated on the surface[5, 6, 10]. These factors must be optimised in order to obtain well-ordered crystalline aggregates and hence good charge transport properties. Experimental characterization techniques are employed to investigate the structure and morphology of these interfaces, at the microscopic scale[5, 30–34]. A detailed knowledge on the structure/properties relationship, together with a comprehensive understanding of the molecular process leading to the morphology at the interfaces between organic materials is a prerequisite for the fabrication of devices with enhanced performance. In this respect, computational models can provide useful tools to gain a better understanding about the nanoscale morphology of interfaces and charge transport properties, such as charge carriers mobility and charge injection rates.

In this thesis, computational modelling techniques at different scales were carried out to investigate the structure, dynamics and electronic properties of materials used in organic electronics. In particular, starting from a detailed knowledge of properties of the materials studied, the aim of this thesis was to develop computational tools enabling a better understanding on the morphologies of materials at the interfaces by performing molecular dynamics (MD) simulations, mimicking the experimental process for the fabrication of organic devices, and eventually correlate the results with available experimental data. Furthermore, the morphologies obtained by simulations were used to investigate the electronic properties in realistic aggregates by performing density functional theory (DFT) calculations, in order to understand the charge transport behavior of materials in real devices. The detailed atomistic information obtained were then used to develop coarse-grained models to scale-up the size and time scale of our simulations, approaching the device-like scales. The correlation between

the morphologies at the interface between materials and electronic properties enables the understanding of phenomena occurring at the nanoscale in real systems, such as degradation of materials, structure/properties relationship, and, in turn, by comparing our results with experiments, we could improve processes leading to better performance and hence enhancing the efficiency of organic electronic and optoelectronic devices.

In Chapter 2, an overview on the main features of organic electronics are described, from devices to molecular properties of materials used in organic electronics and the characterization techniques to investigate them.

In Chapter 3, the methods used for the simulations performed in this thesis are presented.

In Chapter 4 and 5, the morphology of 2D and 3D aggregates of PTCDI-C13, an n-type semiconductor used in organic field-effect transistor, were investigated, respectively. In particular, the phases of the materials in 2D aggregates were modeled and their structure and dynamics were studied by performing MD simulations. The structures obtained were then used to compute electronic properties by DFT calculations, obtaining the stability and charge transport properties of the 2D aggregates. These configurations were then used to model the 3D bulk phases of the material, by performing MD and metadynamics simulations in order to determine the most stable bulk structure, and then compute the charge transport properties. These investigation led us to gain a complete structural and electronic picture of the semiconducting material. These works have been already published [35, 36].

In Chapter 6, the atomistic information obtained by the previous works were used to develop a coarse-grained model of the PTCDI-C13 by the parametrization of atomistic potential, decreasing the complexity of the system. The structural properties of the coarse-grained models of PTCDI-C13 3D bulk phases were compared to the atomistic ones.

In Chapter 7, the morphology of PTCDI-C13 at the interface with different substrates was studied by performing MD simulations. In particular, the interface with a polymeric material commonly used as gate dielectric in organic devices, poly(methyl methacrylate) (PMMA), was investigated, applying computational approaches that mimic the fabrication process of organic devices. Furthermore, the interface with a model 2D material, graphene, was modeled and the results were compared with experiments.

In Chapter 8, the interface between a prototypical hole transport material and the anode electrode used in organic light-emitting diodes was modeled. In particular, in order to understand the process leading to the degradation of materials at the interface in these devices, a model of the interaction between an organometallic material and indium tin oxide (ITO), was developed, by applying advanced computational techniques to obtain realistic morphologies of the interface and compute charge injection rates at the interface.

In Chapter 9, the structure, dynamics and electronic properties of phosphorene at the interface with organic materials were studied, by performing MD and DFT calculations. Namely, the interaction with alkanes and with PMMA was investigated to study the structural and electronic changes of phosphorene at the interface with materials used in organic electronics.

Chapter 2

Organic Electronics: materials, processes and devices

Organic electronics is a branch of materials science that deals with devices constituted by organic small molecules or polymers. The progress of applied research in organic and hybrid electronics, nowadays, relies largely on the development of novel materials, with tailored properties, able to perform targeted, complex functionalities at the molecular level[9, 11]. In this respect, intense research efforts have been carried out, during the past few decades, to develop materials based on small organic molecules and polymers, constituting the active component of devices, such as organic light-emitting diodes (OLEDs), organic field-effect transistors (OFETs), organic light-emitting transistors (OLETs) and organic photovoltaics cells (OPVs)[37–44]. The main features of these devices are the materials used and the fabrication and processing techniques. Their development leads to progress and enhancement in the fabrication of high performance organic electronic devices. In particular, remarkable electronic and optical performances can be achieved by active layers constituted by thin-films of crystalline or polycrystalline organic materials, where the growth of ordered aggregates is a prerequisite for optimal efficiencies[9, 11, 12].

The ordered aggregation of these materials depends crucially on the interactions at the interface with other materials in devices. The morphology at these interfaces, in turn, affects the electronic properties of materials, hence determines the overall charge transport in organic electronic and optoelectronic devices[6, 22, 31, 45, 46].

In this chapter, an introduction on the most studied organic devices and their features is presented. Moreover, an analysis on the properties of the materials used for the fabrication of these devices, from the morphology in thin films to their charge transport properties, is described, together with the experimental techniques employed for the characterization of the structural and charge transport properties of materials. Finally, the organic and inorganic materials investigated for the scopes of this thesis are shown.

2.1 Organic light-emitting diodes

Organic light-emitting diodes (OLEDs) are devices in which the emission of light occurs from an excited molecule, called emitter. In the simplest example of an OLED, the emission layer lays between two electrodes, a cathode and an anode. Usually, the cathode is metallic (Al, Ca, Ba) and the anode is a transparent metallic oxyde (the most common is the indium-tin oxyde, ITO)[45, 48–50]. In the simplest OLED device, electrons are injected by the cathode to the lowest unoccupied molecular orbital (LUMO) of the organic semiconductor, while holes are injected by the anode on the highest occupied molecular orbital (HOMO) of the organic semiconductor. Electrons and holes recombine in the emitting region, forming an exciton. This exciton decays emitting a photon of energy $h\nu$, with an energy equal to the energy band gap between the HOMO and the LUMO, in the range of visible light. Hence, the emitting properties and overall performance of these devices depend on the HOMO and LUMO characteristics of the organic materials used, which are correlated to the conduction and valence bands of the inorganic semiconductors. OLEDs composed of cathode, anode and active layer present some performance issues. Namely, holes usually have a higher charge mobility than electrons, leading to an emission nearer to the cathode instead of the middle of the active region. Moreover, exciton-metal quenching can take place in the vicinity of electrodes. For these reasons, then, OLEDs are usually fabricated with a multilayer architecture. In particular, layers for the charge injection and trasport can be inserted between the electrodes and the active layer, in order to improve efficiency of charge injection and to balance electrons and holes transport in the emitting layer (see Figure 2.1a). Nowadays, OLEDs are fabricated in stacks, called stacked or tandem OLEDs[47, 49, 51, 52], in which the whole device is formed by cells functioning as a single OLED (see Figure 2.1b). Every cell of the stack emits light of a different colour and works at a fraction of the voltage required. Therefore, with this architecture the degradation of materials and the high voltage due to the high current density within the device layers are reduced. Applications of OLEDs range from smartphones displays, TV screens,

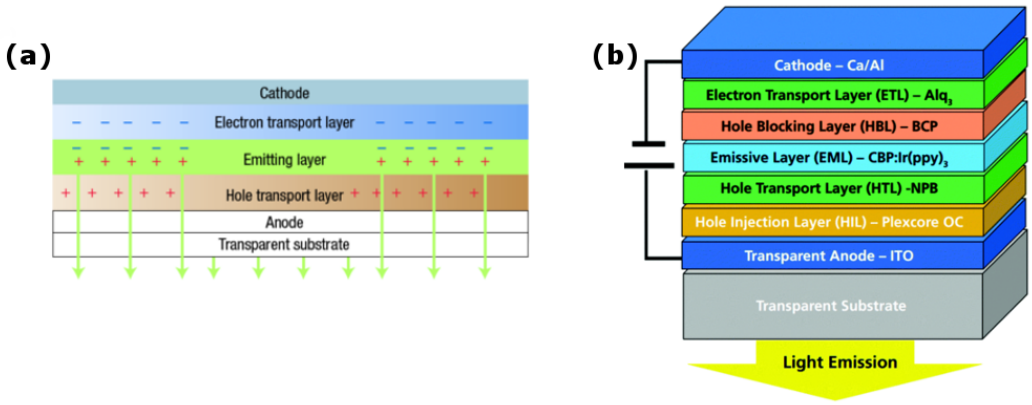

FIGURE 2.1: Organic light-emitting diode in multilayer (a) and stacked (b) architectures. Adapted from Ref. [12, 47].

computers, to lighting. Compared to LEDs, OLEDs present lower production costs, lightweight and flexibility, enhanced brightness and wider viewing angle, less energetic consumption and the possibility to fabricate large-area devices. Due to the layered stacked architecture of OLEDs, one of the crucial aspects that affects greatly the performance of the devices is related to the processes leading to degradation of materials constituing the layers of OLEDs, mostly occuring at the interfaces[23, 51, 53, 54]. In this respect,computational models provide useful tools to gain a better understanding about the nanoscale morphology of interfaces and the charge injection from metallic electrodes to the organic semiconductor layer, in order to develop devices with enhanced performances[55–57]. This issue will be addressed in Chapter 8. The active layer in OLEDs is usually composed by small organic molecules or by organometallic complexes. The use of organometallic complexes as host materials is due to the efficiency of the decay mechanisms. The formation of an exciton statistically populates the singlet (S_1) and triplet (T_1) states at 25% and 75%, respectively. Organic molecules usually decay by fluorescence with the transition $S_1 \rightarrow S_0$. The T_1 state is usually poorly populated in organic materials because the inter system crossing (ISC) $S_1 \rightarrow T_1$ is energetically unfavourable, since it requires a spin flip. The internal quantum efficiency (IQE) is therefore limited to 25% in organic materials. Organometallic complexes present spin-orbit coupling, which allows easier spin flipping and hence increases the inter system crossing. Excited states in these complexes can decay by phosphorescence with the transition $T_1 \rightarrow S_0$. If this transition is radiative, both S_1 and T_1 can decay in a radiative process, leading to a potential IQE of 100%.

2.2 Organic field-effect transistors

Organic field-effect transistors (OFETs) are commonly constituted by three electrodes (the gate, the source and the drain), a gate dielectric layer and an organic semiconducting layer (see Figure 2.2). These devices can be fabricated in the top-gate configuration, in which the gate electrode lays on top of the semiconducting layer, or in bottom-gate configuration, in which the semiconducting layer is on top of the dielectric layer with an underlying gate electrode. Source and drain electrodes, in turn, can be deposited on top of the semiconducting layer (top-contact) or on top of the dielectric layer (bottom-contact). In Figure 2.2 a bottom-gate top-contact OFET is represented. In this architecture, when no voltage is applied between gate and source electrodes, the device is in the "off" state. The application of a gate voltage (V_G) generates charge polarization in the semiconducting layer, at the interface with the dielectric layer. In particular, for negative V_G, holes are generated in the semiconducting layer at the interface with the gate dielectric (p-channel devices), while positive V_G causes accumulation of electrons in the semiconducting layer (n-channel devices). By applying another voltage between source and drain (V_{SD}), the charge carriers migrate across the semiconductor and are collected in the drain electrode. This is called the "on" state of the device. Initially, when $V_{SD} < V_G$, the OFET operates in a linear current regime, following the equation:

$$I_{SD} = \frac{W}{L}\mu\, C \left(V_G - V_T - \frac{V_{SD}}{2} \right) V_{SD} \tag{2.1}$$

where W and L are the width and the length of the channel, respectively, μ is the feld-effect mobility, C is the capacitance of the gate dielectric and V_T is the threshold voltage. When V_{SD} becomes higher than V_G ($V_{SD} > V_G$), the transistor operates in the saturation regime:

$$I_{SD} = \frac{W}{2L}\mu\, C(V_G - V_T)^2 \tag{2.2}$$

The current flow in OFET devices can be therefore modulated by modulating the magnitude of both V_G and V_{SD}. When V_G is applied, the majority of

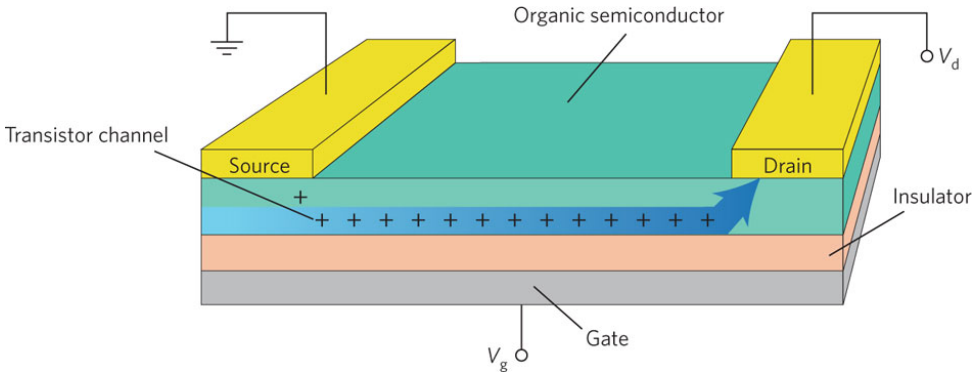

FIGURE 2.2: OFET device in bottom-gate top-contact architecture. Adapted from Ref.[21].

charge carriers are collected within the first few molecular layers of the organic semiconductor at the interface with the dielectric layer. For this reason, the growth and the order of these interfacial semiconducting layers determine the transistor performance. The degree of order and the morphology of aggregates at the interface depend on several factors, such as deposition technique, deposition rates, substrate surface chemistry and surface roughness[5, 6, 58–63]. An increase in the deposition rate increases the nucleation density and leads to smaller crystallites[5, 6, 24]. If the rate is extremely high, the growth becomes completely kinetic and amorphous films are formed[6]. A decrease of the deposition rate should also decrease the nucleation density and increase the size of the grains in polycrystalline materials[5, 6, 24]. Another factor affecting the aggregation of organic materials on the dielectric layer is the substrate temperature. A high substrate temperature allows the organic molecules to diffuse more on the surface, finding the lowest energy sites and forming more regular grains[6, 63]. An excessive increasing of the temperature, however, can lead to a difficult nucleation. Thus, the substrate temperature should not be above the organic material sublimation temperature. For desirable grain morphology and 2D growth, the substrate temperature should be as high as possible, provided that desorption does not dominate and that nucleation is still possible[5, 6]. The aggregation and structure of organic materials at the interface in these devices will be investigated in this thesis. The performance of OFETs are characterized by the mobility, which is the drift velocity of the charge carrier per unit applied field, the on-off ratio (the difference in source/drain current in the "on" and "off" states), often related to the purity of the semiconductor and threshold voltage (the voltage at which the transistor turns from the "off" to the "on" state), which depends on the quality of the interface between the organic semiconductor and the gate insulator.

2.3 Organic light-emitting transistors

Organic light-emitting transistors (OLETs) are ambipolar transistors in which the active region is formed by an organic semiconductor able to transport both holes and electrons. These devices emit light via charge recombination. Excitons are created by the in-plane moving of holes and electrons current, controlled by the gate electrode. An example of an OLET device is represented in Figure 2.3. The electroluminescence intensity is tuned by the gate and drain voltage. Compared to OLEDs, OLETs present more control over charge injection, balance of the holes and electrons current, higher charge carriers density which leads to a higher mobility, improving lifetime and efficiency of devices. While in OLEDs the charge carriers have to move few tens of nm to recombine, in OLETs they have to move hundreds of nm. For this reason, in OLETs the charge transport properties of the active materials must be optimised. Moreover, formation of both electrons and holes should occur at a similar V_T and recombine in a defined region of the active layer. In order to improve efficiency in these devices, usually the active layer is formed by three layers, one composed of a n-type (electrons conductor) semiconductor, one of a p-type (holes conductors) semiconductor and between them a recombination layer, which should have a high emission efficiency. Holes and electrons are formed in the p- and n-type semiconducting layers, respectively, and recombine in the recombination layer upon application of a V_{SD}, emitting light. A key aspect for an efficient charge recombination in these devices is the energy levels alignment of the materials. Namely, the LUMO (HOMO) energy of the n-type (p-type) semiconductor should be similar to the LUMO (HOMO) energy of the material constituting the recombination layer. Another key aspect is represented by the interfaces between organic materials composing the active layer, since the nanoscale morphology at the interface affects the charge transport and therefore the performance of the devices[12, 64].

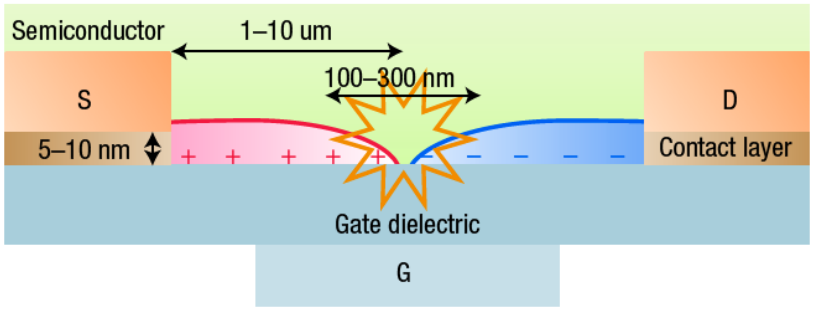

FIGURE 2.3: Representation of an organic light-emitting transistor. Adapted from Ref.[12].

2.4 Organic photovoltaics cells

Solar cells are devices that directly convert light energy into electrical energy. Organic photovoltaics (OPVs) cells cover a range of photovoltaic device architectures that contain at least one organic material in the functional light-absorbing layer. In p-n heterojunction solar cells, the active layer is sandwiched between a high work function anode and a low work function cathode. The active layer is composed of two light-absorbing semiconductors, one p-type and one n-type. These organic semiconductor materials can be deposited as separate layers, with contacts at the p-n interface (bilayer heterojunction), or form a blend in which p-n interactions are extended throughout the active layer (bulk heterojunction, BHJ). In these devices, light absorption occurs at the active layer upon solar irradiation, forming an exciton. The exciton diffuses within the active layer until it reaches the donor-acceptor interface, where it dissociates forming free charge carriers, which diffuse to the anode (holes) and the cathode (electrons) electrodes. At the electrodes, charge is collected. Due to the device architecture and functioning, charge transport and thus performance are strongly affected, among other factors, by the nanoscale morphology at the organic/electrode and organic/organic interfaces and molecular packing of materials constituting the active layer[65, 66].

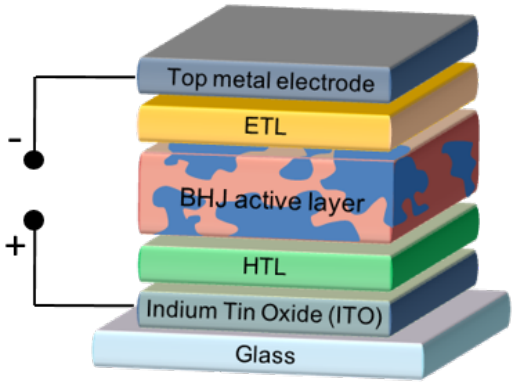

FIGURE 2.4: Organic photovoltaic cell bulk heterojunction.

2.5 Materials for organic electronics

Organic materials for electronic and optoelectronic applications should have specific properties, depending on which role they perform in the device operations. These properties can be manifold, such as optical properties, electrical properties, morphological properties, chemical and thermal stability, and process compatibility. For example, electrodes should ensure ohmic contacts and provide high conductivity to ensure charge injection to the active layer. The gate dielectric must exhibit good dielectric properties to ensure charge carriers accumulation in the active channel upon application of the gate voltage. Organic semiconductors are the most important materials in an organic electronic device, therefore their properties are the most important. In particular, a good organic semiconductor should present good thermal and chemical stability, molecular packing that favor the migration of electrons, hence favor the charge transport in the device.

2.5.1 Organic semiconductors

The most important property of semiconducting materials for organic electronic devices is the conduction of charges. Charge transport properties in these materials determine the performance of the whole device. A key characteristic which affects the electronic properties of organic materials is the intermolecular order adopted by the molecules in the solid state. Good electronic performance requires strong electronic coupling between adjacent molecules, that in turn depends on the aggregation of the material.

The main differences between organic and inorganic semiconductors reside in the charge transport mechanism. In particular, in inorganic materials charges are fully delocalized in the valence and/or conduction bands and transport is driven by strong electronic couplings. Organic materials are packed via weak van der Waals interactions and charges are commonly transported via hopping between conjugated systems.

In single bonds, the electrons of the outer shells occupy hybridized sp^3 orbitals, forming σ orbitals. In double bonds, instead, the orbitals are hybridized sp^2, in which two p orbitals form the σ orbitals, while the third, p_z, is orthogonal to the linking bond, and overlaps with p_z orbitals of neighboring atoms, forming the π orbitals. A conjugated system presents alternating single and double C bonds. The electrons of π orbitals are delocalized over the whole conjugation of the system, hence they can move from one bond to another. The conjugation can take place even if the carbon backbone is interrupted by single N or S atoms. The whole filled π-molecular orbitals can be associated to the valence bands in inorganic materials, while the unoccupied π-molecular orbitals can be associated with the conduction bands. The HOMO and LUMO energies of a material determine its electronic properties. The energy difference between HOMO and LUMO is called band gap, and usually is in the order of a few eV. Charge carriers in organic materials tipically induce a relatively large local polarization and lattice distortion. The carrier together with the induced polarization is considered as one entity, called polaron. A polaron is defined as a quasiparticle composed of a charge plus its accompanying polarization field.

In organic electronics, the semiconducting materials can be composed by either small molecules or polymers. Small molecule semiconductors are easy to purify and usually form crystalline thin films, which is an important characteristic for layered organic devices. Polymer semiconductors have good electronic properties, processability and flexibility. The charge transport in polymers can be interchain (via π-π stacking interactions) or intrachain (faster than interchain). We can also distinguish between amorphous and crystalline organic semiconductors, with the former presenting a disordered packing, while the latter aggregating in ordered packed structures. Crystalline organic semiconductors packs in two main motifs: the herringbone, with aromatic cores disposed edge-to-face, and the cofacial (or coplanar), with aromatic cores disposed face-to-face, typically with some degree of displacement along the long and short axes of the molecules.

Organic semiconductors are mainly classified as p-type or n-type, which means that they conduct holes or electrons, respectively. This classification arises from the specific properties of the materials. Molecules with low electron affinity (i.e. electron donating) transport holes, whereas molecules with high electron affinity (i.e. electron accepting) transport electrons. In addition, organic semiconductors that are able to transport both holes and electrons are called ambipolar.

p-type semiconductors

The p-type semiconductors discussed in this section are represented in Figure 2.5. The most commonly used p-type organic semiconductors are acenes, heteroacenes and thiophenes, in both small molecules and polymers. Naphthalene (**1**) and anthracene (**2**) are the less extended acenes, but, due to their poor electronic properties, they are not significantly used for device applications. Increasing the dimension of the aromatic core, the intermolecular overlap of the electron cloud increases, resulting in a larger electronic coupling, hence better electronic properties. The most studied p-type organic small molecule semiconductor is certainly pentacene (**3**), due to its efficient charge transport and highly ordered herringbone molecular packing (up to 1.5 $cm^2V^{-1}s^{-1}$)[67]. Pentacene has been widely investigated in the last years, as prototypical p-type semiconductor for organic electronics, by both the morphological and the electronic point of view[46, 68–70]. Nevertheless, pentacene presents also some important drawbacks, such as oxidative instability and absorption in visible spectra[71], hence limiting its application in electronic devices requiring ambient stability and optical transparency. All the acenes exhibit a typical the classic herringbone packing[9]. By functionalizing the molecular aromatic cores, the molecular packing usually change, leading to a cofacial motif[72] which can in principle increase the charge mobility. An example is rubrene (**4**), a tetracene derivative, which shows high charge carriers mobility, due to the strong π-stacked arrangement in the solid state[73, 74]. Other examples are porphyrins (**5**) and phthalocyanines (**6**), which present strong π-π interactions between cores, and coronenes (**7**), which aggregate in a discotic columnar liquid crystalline phase[75]. Another very important class of p-type materials are the oligothiophenes, which

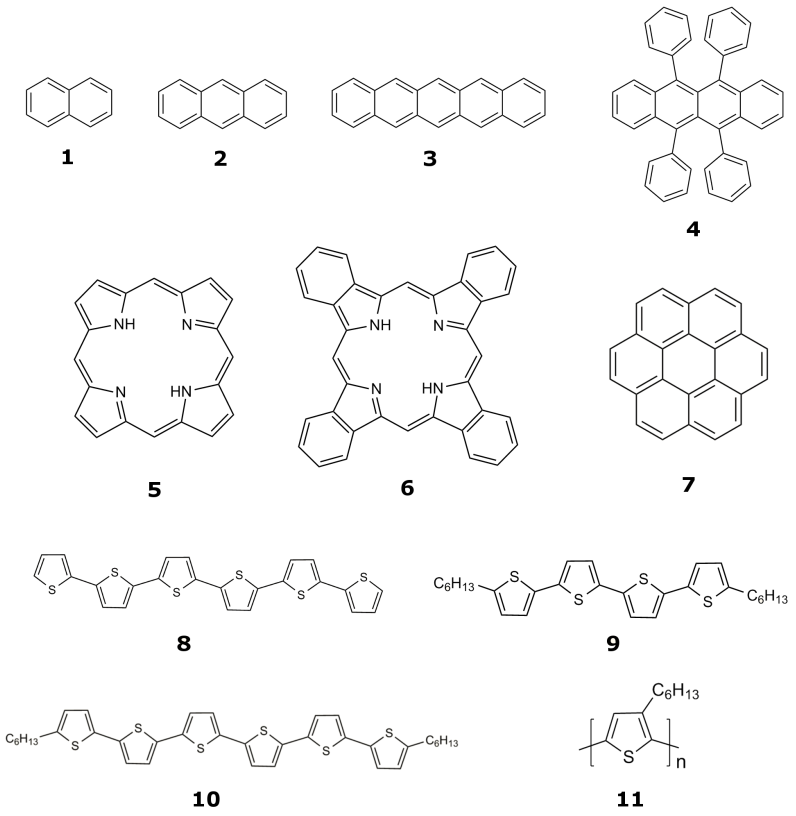

FIGURE 2.5: Organic p-type semiconductors.

have attracted attention because of their planar structures and ease of tunability. The functionalization of oligothiophenes with alkyl groups could also improve the field-effect performance of organic compounds. This is due to the stand-up configuration adopted by the molecules, i.e. solid state arrangement arrangement with their long axis perpendicular to the substrates[26]. Among the p-type semiconductors based on thiophene ring, the most studied are the sexithiophene (6T) (**8**), the DH-4T (**9**) and the DH-6T (**10**) [9, 64]. The p-type polymer polythiophene was used to build the first OFET device[3] (see Chapter 1). A derivative of polythiophene, which is one of the p-type polymeric semiconductor most used in device applications, is the poly(3-hexylthiophene) (**11**), known as P3HT[61, 76–79]. P3HT shows high mobility, good crystalline packing[77], with lamellar structures which enhance charge transport[79].

n-type semiconductors

n-type organic semiconductors (Figure 2.6) are usually less studied than p-type counterparts, mostly due to their instability in the presence of air and water. To achieve good electron injection from electrodes to n-type semiconductor, the electron affinity of the semiconductor should be close to the Fermi energy of the electrode. The introduction of electron-withdrawing groups like halogens, cyano and carbonyl groups can efficiently lead the LUMO energy level closer to the work function of electrodes. Among the halogens groups, the most used to functionalize organic semiconductors is the fluorine atom, because

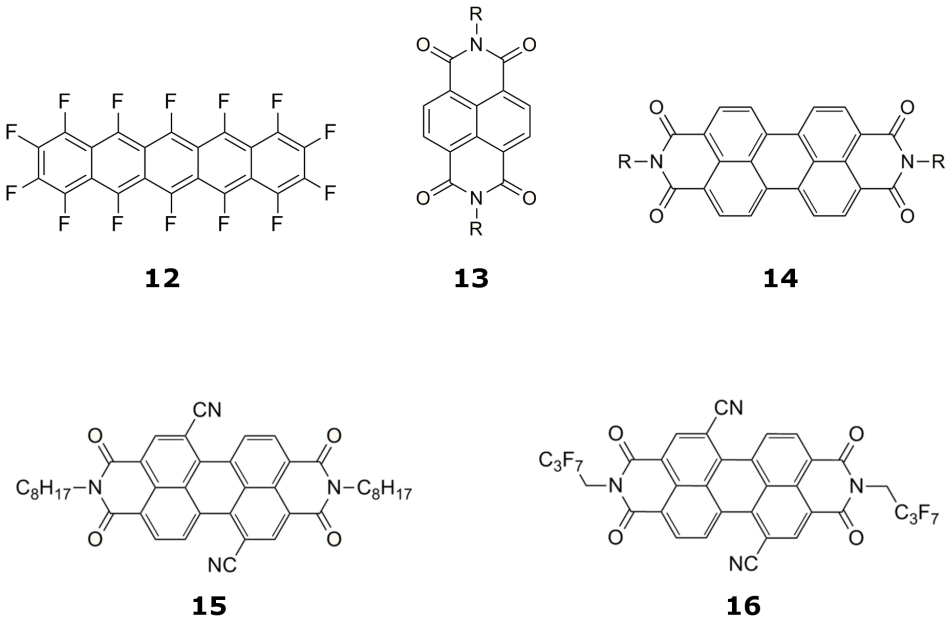

FIGURE 2.6: Organic n-type semiconductors.

it enhances the charge mobility and stability of organic semiconductors. For example, the pentacene derivative functionalized with fluorine atoms, perfluoropentacene (**12**), shows n-type characteristics[80]. One of the most important classes of n-type semiconductors are imides. The most common compounds of this group are naphthalene tetracarboxylic diimide (NTCDI) (**13**) and perylene tetracarboxylic diimide (PTCDI) (**14**) [9, 11, 24, 25, 31–34, 37, 58, 69, 70, 81–85]. These compounds can be functionalized by introducing substituents to the nitrogen or/and to the bay area of the aromatic cores, leading to a fine tuning of the molecular packing, stability and charge mobilities. NTCDI derivatives functionalized at the nitrogen show good electron mobilities[86, 87]. PTCDI derivatives are commonly used in organic devices as n-type semiconductors due to their high electrons conductivity, the strong π-π interactions leading to highly ordered molecular packing in thin-films, high photochemical stability, good absorption properties and mechanical robustness. For these reasons, perylene diimide derivatives are good candidates for OPVs and OFETs applications[9, 11, 24, 33, 34, 82, 84, 85, 88–90]. PTCDI derivatives present good electron mobilities for both substitution at the nitrogen and at the aromatic cores. Two widely studied PTCDI derivatives functionalized at the nitrogen are PTCDI-C8 and PTCDI-C13 (see Figure 2.8a) [5, 24, 25, 33, 34, 59, 63, 85]. PTCDI-C13 is also a semiconducting material studied in this thesis (see section 2.12). The functionalization at the bay area, on the other hand, is usually made by cyano and halogens groups, which usually improves the air-stability of PTCDI, whereas it affects the molecular packing of the materials in thin films, lowering the charge mobility. Some examples of these functionalization, are PDI8-CN_2 (**15**) [31, 91, 92] and PDIF-CN_2 (**16**) [82, 93, 94]. Similarly to the case of p-type semiconductors, several polymers based on n-type semiconductors have been synthesized

during the last years[95].

2.5.2 Gate insulators

The crucial parameter of a gate insulators for applications in organic devices, is the dielectric constant, which should be high in order to scale down the device dimensions, lowering the driving voltage of the overall device. The mostly used materials for gate dielectric is SiO_2[5, 31, 58, 63, 66, 70, 96–99]. Nevertheless, because of the high operating voltage applied to achieve good conductivity, the high costs and the inorganic nature of this material, recent research has been focusing on the development of organic polymeric materials to be used as gate dielectric in organic electronic devices[10]. Organic polymers exhibit ideal flexibility for flexible electronics and promote intimate contact with the organic semiconductors. Among these, the polymers usually employed as gate insulators are polystyrene (PS), polyvinyl-phenol (PVP), polymethyl-methacrylate (PMMA), polyvinyl-alcohol (PVA)[7, 10, 29, 61, 81, 100].

2.5.3 Electrodes

The materials used for the electrodes are critical for the fabrication of high performance organic devices. Materials for applications as electrodes should present high conductivity, high stability, good adhesion with the organic semiconductors and a work function aligned with the organic semiconductors energy levels. The most widely used metallic electrode is certainly Au[9, 25, 59, 101, 102]. However, because o f its high cost, alternative materials such as conductive polymers (polyaniline, polypyrrole and PEDOT:PSS)[10, 103], and other metals like Al and Ag-nanoparticles, have been used. The most widely used anode electrode is indium tin oxide (ITO)[45, 48–50], which is also one of the materials studied in this thesis.

2.6 Techniques of fabrication of thin film materials

The morphology at the interface in organic electronic and optoelectronic devices depends on the materials used (and the nature of their interactions), the fabrication methods and the processing techniques. In this section, the main fabrication processing techniques used to grow organic materials on substrates are presented.

2.6.1 Vacuum thermal evaporation

Vacuum thermal evaporation (VTE) is a technique for the growth of thin films that makes use of an ultrahigh vacuum environment to deposit and purify small-molecule organic semiconductors on a substrate. In particular, the organic semiconductor is placed in a vacuum chamber at a pressure of 10^{-3} Pa. The organic material is then heated to its melting or sublimation temperature, with the substrate placed above the vacuum chamber, allowing the formation and growth of the organic semiconducting layer. The organic materials grown with this technique are required to be thermally stable. The main advantages of this technique are the control of the purity, thickness and structural properties of the film deposited, obtained by controlling the deposition rate and the substrate temperature. If needed, two or more materials can be evaporated in sequence or at the same time. Films deposited by vacuum evaporation have generally good homogeneity and structural properties. The main disadvantages of this technique, however, are the high costs of instrumentation, the longer times for deposition, the difficult control over the film thickness uniformity and dopant concentrations and the impossibility to scale up for industrial applications.

2.6.2 Organic vapor phase deposition

In order to overcome the issues related to the VTE deposition technique, organic vapor phase deposition (OVPD) has been demonstrated as an alternative technique that significantly improves control over doping, and is adaptable to rapid, particle-free, uniform deposition of organics on large-area substrates[104]. In OVPD, the evaporation area and the deposition area are physically separated and can be independently optimised. The organic compound, placed in the evaporation area, is thermally evaporated into a diluting, non-reactive gas stream (for example nitrogen), and then transported in a hot-walled deposition are toward a cooled substrate where the condensation occurs. This technique allow the deposition of organic materials at lower pressure respect to the high vacuum of VTE. Moreover, flow patterns in OVPD may be engineered to achieve a substrate-selective, uniform distribution of organic vapors, resulting in a very uniform coating thickness and minimized materials waste. Also, the inert gas stream prevents contaminations.

2.6.3 Liquid phase deposition techniques

Liquid phase processes are among the most important for the fabrication of organic electronic devices. Many organic semiconductor materials have been functionalized and engineered to increase their solubility, in order to make easier their growth. The most important liquid phase techniques are spin-coating, drop-casting and inkjet printing. Spin-coating is a widespread technique used to obtain uniform thin films on substrates[28, 41, 88, 105]. The spin-coating technique consists in the coating of a substrate with an organic material thin film, diluted in a solvent. When the substrate is coated, it rotates (spin) at high speed (usually about 600 rpm), pulling the solvent to the sides exploiting the centrifugal forces. Airflow then dries the remaining solvent, leaving a plasticised thin film on the substrate. The processing parameters in spin-coating are crucial in order to obtain good aggregated thin films. In this regard, the spinning velocity and drying times are two of the parameters that mostly affect the final morphology of the films obtained. The main advantages of spin-coating are the ease of the process set-up, with which uniform thin film coating can be achieved. The disadvantages are the high waste of material (usually about 90%) with the rest being flung off the side and wasted, which is not convenient for industrial applications, the fast drying times leading to lower performance of materials which require longer time to self-assemble or crystallize, and finally the possibility to coat one substrate at a time, resulting in a low throughput technique. The drop casting technique consists in the dropping of a solution containing the organic material on a substrate, followed by evaporation of the solvent and subsequent formation of the thin film. This technique is usually carried out at room temperature, even if the temperature can be increased to speed-up the evaporation or to improve the morphology of the film. This is a really simple technique, with a very low waste of material, but it can cover a low area of substrate and the thickness and uniformity of the film are hardly controllable.

Research efforts are now focusing on the development of large-area liquid deposition techniques, enabling industrial fabrication of organic electronic and optoelectronic devices based on thin-films. In particular, inkjet printing represents an accurate and reproducible technique for the preparation of thin films[106]. This technique in based on the ejection of droplets of material from a nozzle, which subsequently coalesce on a substrate, forming printing patterns that depend on the size and spacing between droplets. This approach allows the control of the size of the droplets ejected and the patterns of the final film by modulating the specific parameters.

Another large-area fabrication technique is the roll-to-roll technique, which, as the name suggests, fabricates electronic devices on a roll of flexible plastic or metal foil, or can be used for the application of coatings to flexible devices[107–109].

2.7 Growth of organic materials at interfaces

The growth of an organic material on a substrate can be affected by several factors, such as the deposition rate, the growth technique, the process temperature. The growth mode of an organic material on a substrate, though, is mainly determined by the molecule/substrate and molecule/molecule interaction energies. The stronger the molecule/substrate interactions, the greater the tendency to 2D growth, and vice versa. Three dimensional growth at the interface with the surface can give rise to voids in the film with consequent formation of grain boundaries, affecting the charge mobility and thus the efficiency of the device. Three main growth mode can be observed at the molecule/substrate interface:

- Frank-van der Merwe (layer-by-layer growth): organic molecules with strong interactions with the substrate form smooth layers, leading to a 2D growth, in which the subsequent layers are formed only when the previous layer is already fully grown (Figure 2.7a). This growth is usually associated with higher mobility of the organic semiconductors.

- Volmer-Weber (island growth): the molecule/substrate interactions are low, enabling the molecules to move freely on the surface and form large, isolated islands of crystal after deposition, causing the 3D growth of rough multi-layer films on the substrate (Figure 2.7b).

- Stranski-Krastanov (layer-plus-island growth): molecule/substrate interactions are not too strong or too weak. Substrate can impose crystallinity to the organic molecules without preventing self-organization, letting molecules to aggregate. Transition from the 2D (layer-by-layer) to 3D (islands formation) growth occurs at a critical layer thickness which is highly dependent on the molecule and substrate (Figure 2.7c).

Thus, the stronger the molecule/substrate interactions, the more 2D will be the growth, whereas the stronger the molecule/molecule interactions, the more 3D will be the growth. This is a phenomenological classification, based on observation and calculations, mainly performed on inorganic materials. In organic materials, many more features must be considered, with the molecule/molecule and molecule/substrate interactions being one of the most important, but not the only one. Therefore, there cannot be a unified classification of growth modes for organic materials, but these can be regarded as a good base to understand the molecular features of interfaces.

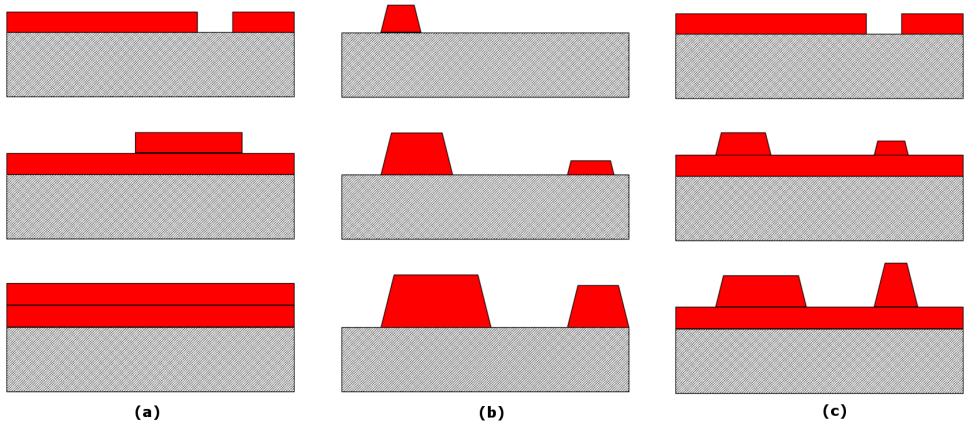

FIGURE 2.7: Representation of the different growth modes of organic materials on a substrate: (a) layer-by-layer growth, (b) island growth, (c) layer-plus-island growth.

2.8 Characterization of organic materials

Film morphology and growth modes of organic materials at the interfaces can be investigated by a series of techniques with which the film morphology and molecular structural parameters can be obtained, including scanning probe techniques, such as atomic force microscopy (AFM) and scanning tunneling microscopy (STM). Detailed information about the structure, orientation and growth of materials can be obtained by spectroscopic techniques like x-ray diffraction (XRD) and grazing-incidence x-ray diffraction (GIXD). Spectroscopic techniques, such as absorption, photoluminescence and electroluminescence, can also provide information about the nature of the materials and the aggregation at the solid state.

2.8.1 Scanning probe techniques

Atomic force microscopy

In atomic force microscopy (AFM), a sharp tip at the free end of a cantilever interacts with a surface. The forces imposed to the tip by the sample surface can be used to form a three-dimensional image (topography) at the nanometric resolution. AFM can be operated in contact mode, in which the tip is always in contact with the surface, following the surface topography, or in tapping mode, where the cantilever oscillates at or near its resonance frequency at a certain distance from the surface, with a laser beam positioned at the back of the cantilever sending the signal to a detector. When the tip interacts with the surface, changing its oscillation frequency, the detector collects the changes in the cantilever oscillation. The resulting tapping AFM image is produced by imaging the force of the intermittent contacts of the tip with the sample surface. From an AFM image, several quantitative parameters can be obtained. For example, information about island formations on a substrate can be extracted, like the step height, providing information about the growth modes and morphology of

aggregates, or the skewness and kurtosis, which measure the symmetry and the tailing of the data, respectively. AFM can be performed during the growth of an organic semiconductor material on a substrate in order to obtain morphological information at low-coverage. This technique can then be useful to obtain information about the morphology of interfaces and growth modes in organic electronic devices.

Scanning tunneling microscopy

Scanning tunneling microscopy (STM) is a high-resolution (in the order to 0.1 nm) imaging technique based on quantum tunneling. The resulting image carries information on the distribution of electrons on the surface of the sample, which usually follows closely the surface topology. To obtain a STM image, the tip of STM is firstly brought near to the sample surface. Then, a voltage bias is applied, allowing the electrons to tunnel between the tip and the sample, creating a tunneling current, which is collected. Similar to AFM, STM can be carried out in two modes: in the constant height mode the height and voltage of the tip are kept constant, resulting in an image of the charge density of the surface, while in the constant current mode a piezoelectric controls the height of the tip depending on the measured tunneling current, resulting in a topography of the surface. This technique is commonly used to investigate the molecular packing of organic semiconductors at the interface with a substrate, giving detailed atomistic information.

2.8.2 X-ray crystallography

X-ray crystallography has been extensevely used to obtain atomic and molecular information about bulk crystalline structure of organic materials. This technique is based on the diffraction of an x-ray beam caused by atoms in the sample. By measuring the angles and intensities of the diffracted beams, a crystallographer can produce a three-dimensional picture of the density of electrons within the crystal, determining the atomic position, the lattice parameters the disorder and presence of impurities of the sample. Information about lattice parameters and orientation of molecules in a crystal are usually obtained by x-ray powder diffraction. Grazing incidence x-ray scattering, instead, permits to study the surface and interface of thin films.

X-ray powder diffraction

X-ray powder diffraction (XRD) is a technique used to identify the phase and unit cell of a crystalline organic material, based on the constructive interference of monochromatic X-rays and a crystalline sample. The interaction of the incident rays with the sample produces constructive interference (and a diffracted ray) when conditions satisfy Bragg's Law ($n\lambda = 2d\ sin\theta$). These diffracted X-rays are then detected, processed and counted. By scanning the sample through a range of 2θ angles, all possible diffraction directions of the lattice are obtained. Conversion of the diffraction peaks to d-spacings allows identification of the lattice parameters of the organic sample. With this technique is possible

to identify which phase is present in a polycrystalline sample, or to define the lattice parameters, used as reference to further correlate this result with AFM and STM imaging, for example.

Grazing incidence x-ray scattering

Grazing incidence x-ray scattering (GIXD) is a technique used to investigate the molecular packing and orientation of organic materials in thin films. GIXD is done with a very low incidence angle x-ray beam, $\alpha < 1°$. In this way, signal losses caused by the absorption of x-ray beams from the substrate are avoided. Therefore, reducing α allows more x-rays to be absorbed by the sample thin film, increasing the signal yield. By setting the α below the critical incidence angle α_c, the x-rays will be totally reflected from the sample surface, obtaining information about the morphology of the thin film surface. To obtain information about the bulk structure of the thin film, instead, α should be higher than α_c.

2.8.3 Spectroscopic techniques

Absorption spectroscopy

Absorption spectroscopy refers to a spectroscopic technique used to investigate at which wavelength a sample absorbs the incident radiation. Namely, the sample is irradiated by a large range of radiation frequencies, resulting in an absorption spectrum, which is determined by atomic and molecular composition of the material, hence providing information about the molecular nature of the sample. Moreover, the intensity of light absorbed by the sample gives information about its morphology and molecular packing at the solid state. In particular, ultraviolet–visible spectroscopy (UV-Vis) is an absorption spectroscopic technique that works in the ultraviolet-visible spectral region. This absorption spectroscopy is particularly important in the field of organic materials for devices since the π-conjugated molecules absorb light in the UV-Vis range.

Photoluminescence and electroluminescence

Photoluminescence (PL) is the light emitted from a sample after the absorption of radiation. The emission can occur by fluorescence of phosphorescence, where the former refers to a fast relaxation of the excited state at lower energy than the original photons absorbed, while the latter indicates a slower relaxation of the excited states, comprising mechanism like intersystem crossing, particularly important in the case of OLEDs, as described in section 2.1. This technique can be used to investigate the purity, aggregagation and degradation processes of organic semiconducting materials in devices. Electroluminescence (EL) is the emission of light generated upon injection of charges in the form of electric current or electric field.

2.9 Charge transport in organic materials

The nanoscale morphology of organic semiconductors in thin films is closely related to the charge transport properties. In particular, the charge transport properties of organic semiconductors depend on the molecular packing, disorder, presence of impurities and defects. The charge carriers mobility can thus change largely as a function of the sample quality.

π-conjugated systems present a significant delocalization of π electrons, moving within the system via a hopping mechanism. This mechanism occurs, in polymers, along the conjugated chains, while in small molecules π orbitals can delocalize over different neighboring molecules, which are packed via π stacking. This hopping mechanism will be highly anisotropic, depending on the orientation and packing of π cores between which the charges are transported. Hopping transport can be described as a series of successive electron-transfer reactions between neutral and charged molecular or polymeric repeat units, i.e. between local neutral and polaronic ground states. The rate of hopping of a charge carrier between two sites depends on the overlap of the electronic wave functions of these two sites, which allows tunneling from one site to another.

Charge mobility in organic materials

Charge carriers mobility is one of the most important features in the development of organic electronic devices with enhanced performances. In particular, mobility is often defined in terms of phenomenological models. For example, in the Drude model mobility is expressed in terms of the charge density n which has to flow from an electrode to the other under the effect of an electric field $\mathbf{F}$ passing through a conducting medium. This model is described by the equation of motion of a gas of electrons within a metal in which a friction term is inserted to describe the electron scattering:

$$m\dot{v} + \frac{m}{\tau} v_D = -e\mathbf{F} \tag{2.3}$$

where m is the electron mass, τ is the scattering time (that is the avearage time between two nucleus-electron collisions), e is the electron charge, and v_D is the drift velocity induced by the electric field, which is added to the thermal velocity v_{therm}. The total velocity of the electron becomes:

$$v = v_D + v_{therm} \tag{2.4}$$

In the stationary case, v is a constant and is defined as the drift mobility of the charge carrier (μ) as:

$$\mu = \frac{v_D}{F} = -\frac{e\tau}{m} \tag{2.5}$$

The charge carrier mobility is then defined as the ratio between the drift velocity and the applied electric field and is correlated to the scattering time of the electron. Experimentally, charge transport properties are characterized by the charge carrier mobilities. When the electric field is not applied, charge transport

is purely diffusive and is expressed by:

$$\left\langle x^2 \right\rangle = nDt \tag{2.6}$$

where $\langle x^2 \rangle$ is the mean-square displacement, D is the diffusion coefficient, t is the time and n is a size-dependent variable (equal to 2,4 or 6 for 1D,2D and 3D, respectevely). The charge mobility μ is then obtained by the Einstein-Smoluchowski equation

$$\mu = \frac{eD}{k_B T} \tag{2.7}$$

where k_B is the Boltzmann constant. Diffusion is defined as the displacement of a charge around an average position, while drift is the displacement of the average position. Drift is the effect that dominates the migration of the charge carrier across the organic layer in devices.

2.10 Experimental measurements of mobility

Time-of-flight

In time-of-flight (TOF) measurements, the organic layer is sandwiched between two electrodes. A laser pulse irradiates the organic material at a certain wavelength, generating charge carriers near one electrode. Depending on the polarization of the laser pulse and the corresponding electric field, the charge carriers will be holes or electrons, which migrate towards the other electrode. The current at the second electrode is recorded as a function of the transit time t_{tr}. Ordered organic materials result in sharp signals, while in disordered materials a broadening in the signal occurs. With this technique, the charge carriers mobility μ is obtained directly via the equation:

$$\mu = \frac{v_D}{F} = \frac{d}{F t_{tr}} = \frac{d^2}{V t_{tr}} \tag{2.8}$$

where d is the distance between the electrodes, F is the electric field, t is the average transient time and V is the applied voltage.

Field effect transistor configuration

The field effect transistor (FET) configuration can be used to extract the charge carriers mobilities of the device. The operation of the FET can be described by two different regimes. In the *linear regime*, i.e. when $V_{SD} < (V_G - V_T)$, the drain current I_D increases linearly with the applied V_{SD} according to equation 2.1. At higher V_{SD}, when $V_{SD} > (V_G - V_T)$, the FET operates in the *saturation regime*, and I_D varies quadratically with V_G following the equation 2.2. The field effect mobility μ can then be extracted from the slope of the I_D vs V_G in the linear regimeand I_D vs V_G^2 in the saturation regime, with the equations:

$$\begin{aligned} \mu_{lin} &= \frac{L}{W}\frac{1}{C}\frac{\partial I_D}{\partial V_G} \\ \mu_{sat} &= \frac{L}{W}\frac{2}{C}\left(\frac{\partial \sqrt{I_D}}{\partial V_G}\right)^2 \end{aligned} \tag{2.9}$$

2.11 Modelling of materials and interfaces for organic electronics

Experimental techniques, including microscopic, spectroscopic and electrical characterization, enable investigations on the morphology of materials in thin films, on growth modes and nanoscale aggregation, and to evaluate electronic and optoelectronic properties of devices, as described above. However, these techniques lack in the detailed understanding of atomistic phenomena, in particular those occurring at the interfaces of organic electronic devices hampering the accurate definition of structure/property relationship.

In this regard, computer simulations can provide useful tools to link the molecular information to the device performance. Indeed, computational modelling techniques are often used to study the structural and electronic properties of organic and inorganic materials at the nanoscale, allowing the investigation of phenomena occurring at scales where no experimental techniques can venture. Moreover, the atomistic information obtained by these techniques can be used to predict the behavior of materials in device-like scales.

Like the characterization techniques, several accurate computational modelling tools are currently available, each one dealing with different characteristic time and length scales, as will be described in details in the next Section.

In the last years, with the development of computational infrastructures, and especially the HPC facilities, the capabilities of computational modelling techniques has increased exponentially. The main limitation of computer experiments targeting the properties of matter with atomistic resolution remain, however, the characteristic time and length scales of simulations, usually much smaller with respect to the ones needed to cover all the phenomena occurring in materials in devices.

For this reason, each computational technique is usually applied to the study of specific properties and phenomena of materials. In order to bridge the scales of different phenomena, usually multiple simulation methods must be applied, obtaining different kind of information which, once gathered, can lead to a meaningful description of the system under investigation. The interlink between computational tools is the core of multiscale modelling techniques, as it will be described in the next Section.

Quantum chemical calculations explicitly treat the electronic structure of the systems under investigation. These techniques are often used to evaluate the electronic and charge transport properties of materials [35, 36, 89, 110–122]. In particular, the energy levels, molecular binding energy, stability, the charge transport properties of materials, and even excited state properties, including absorption and emission spectra, can be obtained by using these techniques. Moreover, they can also be used to develop force fields for molecular mechanics [57, 114, 123–125].

Molecular mechanics methods are employed to simulate the time evolution of position, velocities and forces on atoms or groups of atoms using classical force fields. This is a widely used method to simulate the morphology of materials in realistic environments [35, 36, 57, 122, 125–128], the deposition of organic materials on surfaces [129, 130] and the structural and dynamical properties

of the materials at the interfaces [46, 124, 129–137]. Predicting the realistic morphology of an organic material is a challenging task, especially if the material is crystalline. For this reason, morphologies obtained by these methods are often validated against experimental results.

Large-scale morphologies can be simulated by developing coarse-grained models of the systems [57, 127, 138–145]. These models represent groups of atoms as a single particle which interact with other particles with a potential obtained by the parametrization of defined atomistic properties.

The computational methods presented above have been successfully used in the last decades by theoretical and computational research groups, in the field of modelling of materials, processes and devices for organic electronics and optoelectronics, leading to an enhanced development of the techniques and to better understanding on the properties and phenomena investigated.

These methods will be treated in more details in the next Section, with a particular emphasis on the techniques applied in this thesis.

2.12 Materials used in this thesis

In this section, the materials modeled and studied in this thesis are described. In particular, several materials for organic electronics were modeled and studied, ranging from small molecules and polymers to organometallic complexes, metal oxides and 2D materials.

Small molecule organic semiconductors

During the PhD period, both p-, n-type and ambipolar small molecule organic semiconductors materials were modeled. In particular, the structure and morphology of the ambipolar organic semiconductor 2,2'-(2,2'-bithiophene-5,50-diyl)bis(5-butyl- 5H-thieno[2,3-c]pyrrole-4,6)-dione, also referred to as NT4N[27, 146], was simulated by performing MD simulations. Moreover, perylene diimide derivatives were also modeled. Namely, two n-type small molecules for bio-devices applications, N,N'-1H,1H'-perfluorobutil dicyanoperylene diimide (PDIF-CN_2) and (N,N'-bis(n-octyl)-dicyanoperylene-3,4:9,10-bisdicarboximide) (PDI8-CN2), were modeled and their interaction with water was investigated (publication in progress). Another material used for bio-electronics applications is the PDI-Lys, which is a perylene diimide functionalized at the nitrogens with lysine. The morphology and structure of this material in thin films were simulated in a collaborative work with the experimental group within the ISMN-CNR institute[147].

The most widely studied organic semiconducting material in this dissertation is a prototypical n-type perylene diimide derivative. Perylene diimide derivatives are commonly used in organic devices as n-type semiconductors. In particular, one of the most widely studied PDI derivatives is the N,N'-ditridecylperylene-3,4,9,10-tetra carboxylic diimide (PTCDI-C13), functionalized with C13 alkyl chains (see Figure 2.8a). Experimentally, a huge increase in the mobility (from 0.58 to 2.1 $cm^2V^{-1}s^{-1}$) is observed by thermal annealing at 140 °C the PTCDI-C13 film[25], due to an improvement in the molecular packing of PTCDI-C13 molecules upon annealing[5, 24, 59]. Vasseur *et al.*[5], for example, observed a dependence of the molecular packing of PTCDI-C13 to the deposition rate during the growth process. They also observed that PTCDI-C13 grow on SiO_2 following a Stranski-Krastanov growth type (described in section 2.7), with a 2D-like growth in the first few layers, with a subsequent 3D-like growth. A lot of studies on the growth of PTCDI-C13 observed the formation of needle-like islands of PTCDI-C13 during the growth[5, 24]. Tatemichi et al. [25] characterized the PTCDI-C13 bulk and thin film by performing x-ray crystallography, reporting a cofacial configuration with a dimeric unit cell. The aggregation, structure and dynamics of PTCDI-C13 will be addressed in Chapter 4, 5, 6 and 7.

The hole transport layer (HTL) of an OLED device was simulated by modelling an organometallic material, in particular an iridium-complex, used as hole transport and emitting material in real OLED devices. The usage of organometallic complexes in OLED devices is explained in section 2.1. Tris[(3-phenyl-1H-benzimidazol-1- yl-2(3H)-ylidene)-1,2-phenylene]Ir (DPBIC) is an Iridium based complex, used as hole-conducting and electron-blocking material in

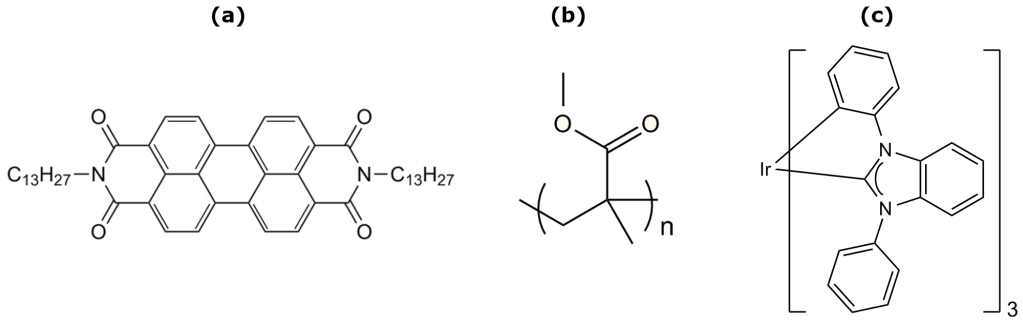

FIGURE 2.8: Structures of PTCDI-C13 (a), PMMA (b) and DPBIC (c).

OLEDs and OPVs (see Figure 2.8c)[57, 148]. The particular spherical structure of DPBIC makes it an amorphous material in aggregates. This morphological and electronic properties of this material will be investigated in Chapter 8.

Polymeric gate insulators

The morphology at the interface between organic semiconducting materials and the gate dielectric layer in organic devices, especially in OFETs, is one of the crucial aspects affecting the performance of devices, as also stressed before in this dissertation. Hence, realistic models of a gate dielectric layer are needed in order to investigate the properties of these interfaces. In this regard, common polymeric insulator materials, used as gate dielectric in organic electronics, were modeled. In particular, a study on the detailed atomistic structure of polyvinyl-phenol (PVP) and polymethyl-methacrylate (PMMA) was carried out[126]. Furthermore, in a perspective of organic bio-devices application, a polymeric insulator based on silk fibroin protein was also modeled. Silk fibroin was reported as a gate insulator for technological and biomedical applications [44, 149, 150]. In this thesis, the PMMA models obtained in previous work were used as gate dielectric layer.

PMMA is a transparent thermoplastic polymer used as coating layer or as dielectric layer in organic devices. PMMA is composed of methyl methacrylate monomers, whose structure is represented in Figure 2.8b. The material was first brought to market in 1933 by the Rohm and Haas Company under the trademark Plexiglas. PMMA presents mechanical strength, is transparent, UV tolerant, easy to process and cheap. PMMA has a density of 1.18 g/cm^3, melting temperature of 433 K and glass transition temperature (T_g) ranged between 363 and 393 K[151]. PMMA is an insulating material, which is why is often employed as dielectric layer in organic devices, mostly in OFETs. PMMA usually leads to better transport properties in organic devices, being capable to associate a good compatibility with organic materials and an ease processability at a high dielectric constant (4.5) in thin films. The morphology of a PMMA slab was obtained as described in previous work[126]. Namely, a periodic model of PMMA chains, with 32 monomer units each, with 10x10 nm lateral size and a thickness of 5 nm, was relaxed by MD simulations at room temperature.

Electrodes

The morphology at the interface between conducting and semiconducting materials and electrodes is crucial in all organic devices. In particular, in this thesis, the morphological and injection properties of the interface between an hole transport material and the anode electrode was studied and will be described in Chapter 8. In particular, as electrode, a doped metal oxide commonly used as anode electrode in OLED devices was modeled.

Indium tin oxide (ITO) is one of the most widely used transparent conducting oxides in organic electronic devices. In particular, ITO is commonly used as anode layer in OLEDs and OPVs, due to its electrical conductivity, optical transparency and ease of processability[152, 153]. ITO is obtained by doping indium oxyde with 5-10 wt% of Sn atoms. A model of ITO will be used as electrode to study the interface between the hole transport layer and the anode layer in OLEDs in Chapter 8.

2D materials

Among the 2D materials, graphene is certainly the most famous, with applications as electrode and substrate in a wide range of organic electronic devices[9, 102, 135, 154, 155]. This interest is due to its electronic properties, showing high electron conductivities and good structural properties for applications in organic devices. A lot of studies have been carried out also on the aggregation of organic materials on graphene surface[100, 155–157]. In this thesis, graphene was used as a prototypical 2D material for the study of aggregation of PTCDI-C13 (see Chapter 7).

Another 2D material, emerging for its excellent semiconducting properties is phosphorene. Phosphorene is obtained by exfoliation of black phosphorus (BP), exhibiting a natural bandgap, unique anisotropy and extraordinary physical properties[158]. In analogy to other layered materials, such as graphite, BP is composed of vertically stacked 2D atomic sheets, held together by van der Waals interactions[159]. In BP, however, the sp^3 hybridization leads to localization of a lone pair of electrons on phosphorus atoms, which results in a puckering of individual layers and to an asymmetric P-P intra-layer bonding pattern. The properties of phosphorene are related to the surface morphology of BP, including strong in-plane anisotropy, due to the surface puckering, which, unlike other layered materials, are reflected in its electronic, thermal and mechanical properties[118, 160–163]. The bonding asymmetry in phosphorene layers is commonly described in terms of armchair (AM) and zigzag (ZZ) directions, referred to the orthogonal vectors in the crystal unit cell[164]. The strong structural in-plane anisotropy in phosphorene layers is reflected in a dramatic difference between several physical properties in the two principal directions, including tensile and shear modulus and thermal transport[118, 159, 164, 165]. Another peculiar property of phosphorene is the occurrence of a sizeable direct electronic band gap, which has been estimated to be about 1.5 eV[159, 164], thus much larger than in BP (0.3 eV)[166]. The band gap of BP is in fact correlated to the number of layers, leading to tunability of the electronic properties of few-layers phosphorene materials, enabling a wide range of applications

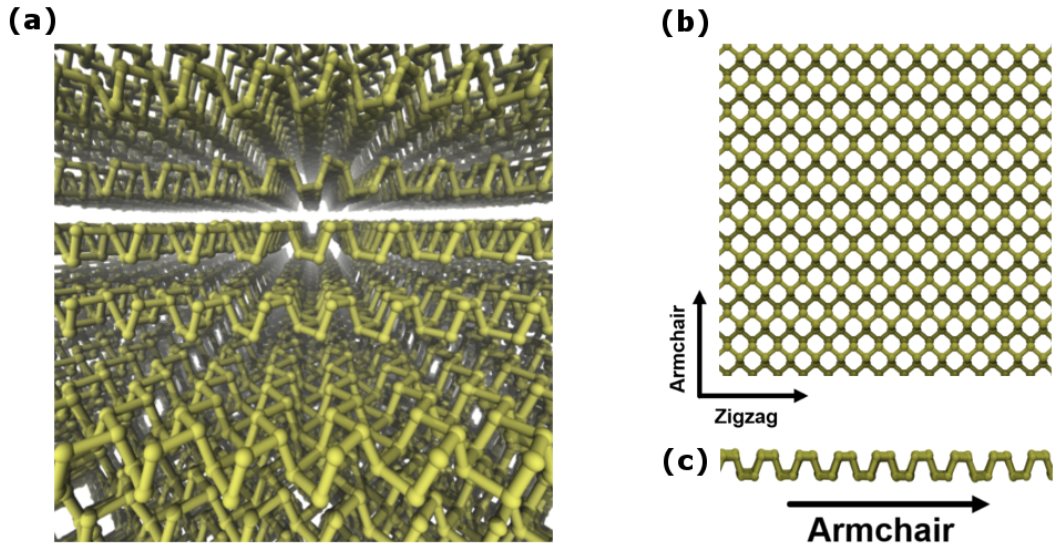

FIGURE 2.9: Black phosphorous bulk structure (a), top view (b) and side view (c) of phosphorene monolayer.

in electronics and optoelectronics[159, 161, 164, 167–169]. Namely, the large, tunable electronic band gap and high hole mobilities at room temperature (up to 10^3 cm^2 V^{-1} s^{-1})[164] make phosphorene an ideal candidate as the active material for field-effect devices. Accordingly, previous work has demonstrated the possibility of fabricating OFETs based on phosphorene, with high on/off ratio and operating in the radio-frequency range. However, a few issues must be addressed before exploitation of phosphorene in large-scale applications, the most relevant of which concerns intrinsic degradation phenomena. Indeed, the phosphorus lone pairs exposed on phosphorene surface are prone to chemical attack by external agents, including oxygen and water, which lead to degradation of structural and electronic properties, as observed recently[159, 164, 170, 171].

Chapter 3

Computational methods

Multiscale modelling refers to a computational approach which intends to bridge multiple models at different scales to investigate the properties of a system. This approach is applied when these properties have to be analysed at different time and length scales, different methods and complexity. Nevertheless, the models used in a multiscale investigation are connected. The multiscale approach outlined in this thesis is addressed mainly in the applications of different methods at different length and time scales to study the properties of the materials used in organic electronics, mostly investigating the morphology and electronic properties at the interfaces, comparing the results with experimental findings. To do so, the methods applied ranged from the atomistic to the mesoscale, trying to elucidate the occurring of phenomena involved in the fabrication processing of organic devices. In this regard, high performance computing (HPC) is of fundamental importance to investigate properties of organic materials, exploiting the potential and reaching the limit of each method used for these investigations. In this chapter, the computational methods used for the scope of this thesis are presented.

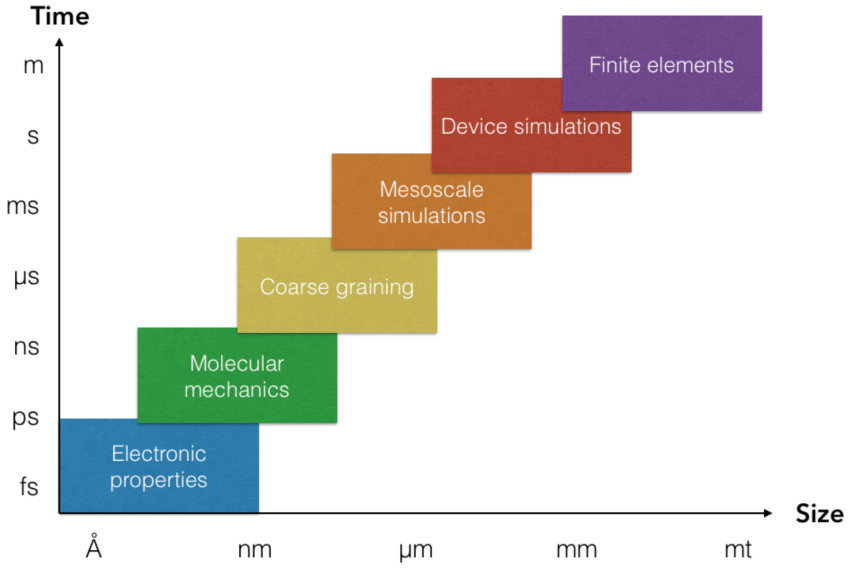

FIGURE 3.1: Representation of the different methods at the different length and time scales.

3.1 Wave function methods

3.1.1 The Schrödinger equation

The electronic properties of an atom or molecule is determined by the time-independent Schrödinger equation[172]:

$$\hat{H}\Psi = E\Psi \tag{3.1}$$

where $\hat{H}$ is the Hamiltonian operator, E is the energy of the system and Ψ is the wave function. The wave function is a central quantity in quantum mechanics. It contains all the spatial and spin coordinates of the particles and it includes all the information about the system. The wave function is such that $|\Psi|^2$ corresponds to the probability distribution of the system in the space defined by spatial and spin coordinates. The operator $\hat{H}$ is the Hamiltonian of the system and it is composed by a kinetic and a potential energy part including nucleus-electron attraction, nucleus-nucleus and electron-electron repulsion terms. In atomic units, the Hamiltonian for N electrons and M nuclei (described by position vectors $\mathbf{r}_i$ and $\mathbf{R}_A$, respectively) is:

$$\hat{H} = -\frac{1}{2}\sum_{i=1}^{N}\nabla_i^2 - \frac{1}{2}\sum_{A=1}^{M}\frac{1}{M_A}\nabla_A^2 - \sum_{i=1}^{N}\sum_{A=1}^{M}\frac{Z_A}{r_{iA}} + \sum_{i=1}^{N}\sum_{j>i}^{N}\frac{1}{r_{ij}} + \sum_{A=1}^{M}\sum_{B>A}^{M}\frac{Z_A Z_B}{R_{AB}} \tag{3.2}$$

where $r_{iA} = |\boldsymbol{r}_i - \boldsymbol{R}_A|$, $r_{ij} = |\boldsymbol{r}_i - \boldsymbol{r}_j|$ and $R_{AB} = |\boldsymbol{R}_A - \boldsymbol{R}_B|$. In the specific case of molecular systems, exact solutions of the equation (3.1) are known for mono-electronic systems. Several approximations schemes are therefore applied to solve such an equation for polyelectronic systems.

3.1.2 The Born-Oppenheimer approximation

A common approximation for the simplification of the problem cited above, is due to Born and Oppenheimer[173]. Since the nuclei are much heavier than electrons, they move more slowly. Hence, one can approximate that the electrons move within a stationary field of fixed nuclei. Within this approximation, the kinetic energy of the nuclei can be neglected and the repulsion between the nuclei can be considered as a constant. The remaining terms define the electronic Hamiltonian:

$$\hat{H}_{el} = -\sum_{i=1}^{N}\frac{1}{2}\nabla_i^2 - \sum_{i=1}^{N}\sum_{A=1}^{M}\frac{Z_A}{r_{iA}} + \sum_{i=1}^{N}\sum_{j>i}^{N}\frac{1}{r_{ij}} \tag{3.3}$$

We can then write the electronic part of equation (3.1) as:

$$\hat{H}_{el}\Psi_{el}(\mathbf{r}_i;\mathbf{R}_A) = E_{el}(\mathbf{R}_A)\Psi_{el}(\mathbf{r}_i;\mathbf{R}_A) \tag{3.4}$$

where Ψ_{el} is the electronic wave function which describes the motion of the electrons.

3.1.3 The Hartree-Fock method

Since there is no analytical solution to the many-body electronic repulsion term in the electronic Schrödinger equation, in the Hartee-Fock method the electron-electron interactions are treated in a mean field approximation, i.e. each electron is considered to move in the mean field due to all other electrons. The Hartree–Fock method also assumes that the ground state N-electron wave function of the system can be approximated by a single Slater determinant.

3.2 Density functional theory

Density functional theory (DFT) is a quantum mechanical method used to investigate the electronic ground state of molecules. The idea at the center of DFT method is that there is a relationship between the total electronic energy and the electronic density. This method also enables the calculation of electronic properties of organic materials and aggregates. In this thesis, DFT calculations were performed by using the softwares SIESTA[174], CRYSTAL09[175, 176], ADF[177] and QUANTUM ESPRESSO[178].

3.2.1 Hohenberg-Kohn Theorem

The Hohenberg-Kohn theorem[179] states that *the ground-state energy and all other ground-state electronic properties are uniquely determined by the electron density $\rho(\mathbf{r})$.* The total electronic energy of the system can therefore be expressed as a functional of the electron density:

$$E[\rho] = T[\rho] + V_{ee}[\rho] + V_{en}[\rho] \tag{3.5}$$

where T[ρ] represents the kinetic energy of the system, while V_{ee} and V_{en} are electron-electron and electron-nucleus interactions, respectively. The latter term can be also written as:

$$V_{en}[\rho] = \int \rho(\mathbf{r}) V_{ext}(\mathbf{r}) d\mathbf{r} \tag{3.6}$$

where $V_{ext}(\mathbf{r})$ is the external potential. V_{ee} can also be expressed as the sum of a classical Coulombic contribution $J[\rho]$ and a non-classical term, containing electronic correlation and exchange terms. The electronic energy can then be written as:

$$E[\rho] = F_{HK}[\rho] + \int \rho(\mathbf{r}) V_{ext}(\mathbf{r}) d\mathbf{r} \tag{3.7}$$

where $F_{HK} = T[\rho] + V_{ee}[\rho]$ is known as the universal functional of the electronic density. The Hohenberg-Kohn variational theorem states that *for a trial density ρ'$(\mathbf{r})$, the energy functional $E_0[\rho']$ cannot be less that the true ground-state energy of the molecule.*

3.2.2 Kohn-Sham equations

Kohn and Sham equations[180] consider a set of one-electron equations that generate the same density of some system of interacting particles. Kohn and Sham divided the energy functional $E[\rho(\mathbf{r})]$ as:

$$E[\rho] = T_s[\rho] + J[\rho] + \int d\mathbf{r} \rho(\mathbf{r}) V_{ext}(\mathbf{r}) + E_{XC}[\rho] \tag{3.8}$$

where $T_s[\rho]$ is the kinetic energy of non-interacting electrons, which can be defined in terms of Kohn-Sham (KS) orbitals ψ_i for each electron:

$$T_s[\rho] = -\frac{1}{2}\sum_{i=1}^{N}\langle\psi_i|\nabla^2|\psi_i\rangle \tag{3.9}$$

the electronic density for such system is:

$$\rho(\mathbf{r}) = \sum_i |\psi_i(\mathbf{r})|^2 \tag{3.10}$$

$J[\rho]$ represents the Coulomb energy:

$$J[\rho] = \frac{e^2}{2}\int d\mathbf{r}\int d\mathbf{r'}\frac{\rho(\mathbf{r})\rho(\mathbf{r'})}{|\mathbf{r}-\mathbf{r'}|} \tag{3.11}$$

E_{XC} is the exchange-correlation energy, including exchange and correlation effects between electrons. A variation of the total energy with respect to ρ leads to the following expression for the effective potential:

$$V_{eff}(\mathbf{r}) = V_{ext}(\mathbf{r}) + \frac{\delta J[\rho]}{\delta\rho(\mathbf{r})} + \frac{\delta E_{XC}[\rho]}{\delta\rho(\mathbf{r})} \tag{3.12}$$

where the last term is the exchange-correlation potential:

$$V_{XC}(\mathbf{r}) = \frac{\delta E_{XC}[\rho]}{\delta\rho(\mathbf{r})} \tag{3.13}$$

Since there is no explicit form for V_{XC}, approximations have to be done.

3.2.3 Exchange-correlation energy functionals

By assuming that electrons move on a positive background charge distribution like a uniform electron gas, in the local density approximation (LDA) the $E_{XC}[\rho]$ is expressed as:

$$E_{XC}[\rho] = \int \rho(\mathbf{r})\varepsilon_{XC}[\rho(\mathbf{r})]d(\mathbf{r}) \tag{3.14}$$

where $\varepsilon_{XC}[\rho]$ is the exchange-correlation energy per electron of a homogeneous electron gas of density ρ. $\varepsilon_{XC}[\rho]$ is calculated once, then E_{XC} can be calculated from the equation 3.14. This method results reliable also for solid state systems, even if their electron density is strongly inhomogeneous. An extension of the LDA method is the generalized gradient approximation (GGA) which also includes a gradient term for the density.

3.2.4 Hybrid functionals

Hybrid functionals incorporate the exact HF exchange contribution into the DFT functional. This is useful since the exchange contributions are significantly larger than the correlation effects, thus an accurate expression for the exchange energy is a crucial requirement for a good functional. One of the most used exchange-correlation hybrid functionals is the B3LYP[181, 182], which stands for Becke, 3-parameter, Lee-Yang-Parr, and follows the proportion:

$$E_{xc}^{B3LYP} = E_x^{LDA} + a_0(E_x^{HF} - E_x^{LDA}) + a_x(E_x^{GGA} - E_x^{LDA}) + E_c^{LDA} + a_c(E_c^{GGA} - E_c^{LDA}) \tag{3.15}$$

where $a_0 = 0.20$, $a_x = 0.72$, and $a_c = 0.81$. E_x^{GGA} and E_c^{GGA} are generalized gradient approximations, and E_c^{LDA} is the local-density approximation to the correlation functional.

3.3 Molecular dynamics

Molecular dynamics (MD) is an atomistic simulation method for the investigation of the molecular properties of the system under study. Starting from initial positions and velocities of a set of particles interacting in specific conditions, this method applies the Newton equation of motion to compute the new set of coordinates and velocities for each integration step. Particles are moved in the new positions, forces are updated and equations reintegrated. With this method, trajectories describing the dynamical evolution of the system over time are obtained. From these trajectories is possible to derive the time-dependent properties of the system as statistical averages. The time scale of MD simulations range from picoseconds (10^{-12} s) to nanoseconds (10^{-9} s). Equations of motion are integrated using very short time steps, usually in the order of femtoseconds, to avoid integration numerical errors, which could lead to a significant energy deviations of the system. The MD simulations presented in this thesis were performed by using the GROMACS[183] and LAMMPS[184] packages.

Phase space

In a dynamic system, the phase space is defined as the space in which all the possible states of the system are represented. For a system containing N particles, 6N values are needed to define the system state (3 coordinates for each atom and 3 for each momentum). Each combination of the 3N atoms and 3N momenta define a point in the 6N-dimensional space and that point describes the dynamic state of a certain particle in the system. For this reason, a point in the phase space can be defined as a microstate of the system. Therefore, an ensemble can be considered a set of points in the phase space. Molecular dynamics generates a sequence of points in the phase space, each of them connected over time.

3.3.1 Equations of motion

Molecular dynamics is based on the integration of the Newton's equations of motion over time for a set of N particles:

$$\begin{aligned} \frac{d^2\mathbf{r}_i}{dt^2} &= \frac{\mathbf{F}_i}{m_i}(\mathbf{r}_1, \mathbf{r}_2, ...\mathbf{r}_N) \\ \mathbf{F}_i(\mathbf{r}_1, \mathbf{r}_2, ...\mathbf{r}_N) &= -\nabla_{r_i} V_i(\mathbf{r}_1, \mathbf{r}_2, ...\mathbf{r}_N) \end{aligned} \tag{3.16}$$

where $\mathbf{r}_i$ is the position vector of the particle i, m_i is the mass, $\mathbf{F}_i$ is the total force acting on the particle i and V_i is the potential energy by which force is calculated. By solving these equations, the total energy of the system is conserved and the time averages obtained during the simulations result equivalent to the averages of the microcanonical ensemble (NVE), in which the number of particles N, the volume V and the energy E are constant. There are other ensembles that can be used, i.e. the canonical ensemble NVT (constant number of

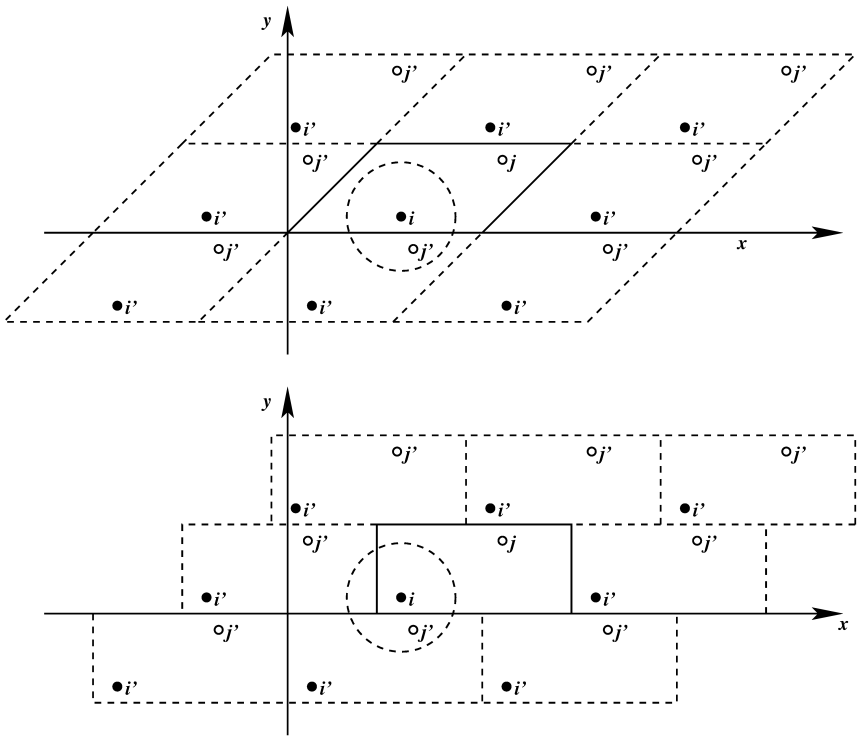

FIGURE 3.2: Periodic boundary conditions in the two dimensions.

particles N, volume V and temperature T), isothermal-isobaric ensemble NPT (where P is the pressure) and the grand canonical ensemble μVT (where μ is the chemical potential). The knowledge of the microstates of the system allows to determine thermodynamic properties, like energies, temperature, pressure, densities, which can, in turn, be correlated with experimental data or can be used to predict molecular properties for which the experimental data is unknown.

3.3.2 Periodic boundary conditions

To minimize the edge effects in a finite system periodic boundary conditions are applied. The dimensions of the box containing the particles constituting the system under study, called unit cell, are defined by three vectors ($\mathbf{b}_1$,$\mathbf{b}_2$,$\mathbf{b}_3$) which represent the three basis vectors of the periodic box. The atoms of the system to be studied are inserted into the simulation box, which is surrounded by translated copies of itself. Therefore, the system has no boundaries. If the simulated system is a crystal, these periodic conditions reflect the real conditions of the system, whereas if the system is non-periodic, like a liquid or a solution, they could cause artifacts. These artifacts can be evaluated comparing the properties variation at different system sizes. They are expected to be less severe compared to the errors resulting from an unnatural boundary with vacuum. There are several possible shapes for the simulation box. Some of them are more indicated for macromolecules in solution (like the rhombic dodecahedron and the truncated octahedron), since fewer solvent molecules are

required to fill the box given a minimum distance between macromolecular images. Nevertheless, a periodic system based on the rhombic dodecahedron or the truncated octahedron it's equivalent to a system based on a triclinic unit cell. This is the most general unit cell and comprises all possible shapes.

3.3.3 Integration of the equations of motion

Leapfrog integration algorithm

One of the integrators of the equations of motion in molecular dynamics simulations is based on the Leapfrog algorithm, which is time reversible. It generates trajectories in the NVE ensemble, in which the energy is conserved. This algorithm, using positions r at time t and the velocities v at time $t - \frac{1}{2}\Delta t$, updates the positions and velocities using the forces $\mathbf{F}(t)$ determined by the positions at time t:

$$\begin{aligned} \boldsymbol{r}\ (t + \Delta t) &= \boldsymbol{r}(t) + \Delta t \boldsymbol{v}\left(t + \frac{1}{2}\Delta t\right) \\ \boldsymbol{v}\left(t + \frac{1}{2}\Delta t\right) &= \boldsymbol{v}\left(t - \frac{1}{2}\Delta t\right) + \frac{\Delta t}{m}\ \mathbf{F}(t) \end{aligned} \tag{3.17}$$

Molecular dynamics simulations normally require properties that depend on position and velocity *at the same time* (such as the sum of potential and kinetic energy). In the Leapfrog algorithm the velocity at time t is obtained from the average of the velocities half a timestep either side of time t:

$$\boldsymbol{v}(t) = \frac{1}{2}\left[\boldsymbol{v}\left(t - \frac{1}{2}\Delta t\right) + \boldsymbol{v}\left(t + \frac{1}{2}\Delta t\right)\right] \tag{3.18}$$

3.3.4 Thermostats

To ensure that the average system temperature is maintained close to a defined temperature (T_{ext}), the system can be coupled to a thermostat. When this is done, the equations of motion are modified and the system no longer samples the microcanonical ensemble. Two different thermostats are generally used to simulate systems in NVT and NPT ensemble: Nosé-Hoover and Berendsen.

Nosé-Hoover thermostat

In the Nosé-Hoover algorithm[185, 186] Newton's equations of motion are modified by introducing a thermal reservoir and a friction term:

$$\frac{d^2\mathbf{r}_i}{dt^2} = \frac{\mathbf{F}_i}{m_i} - \frac{\zeta}{Q}\frac{d\mathbf{r}_i}{dt} \tag{3.19}$$

where the friction parameter ζ is controlled by the equation:

$$\frac{d\zeta}{dt} = (T - T_0) \tag{3.20}$$

where T_0 is the reference temperature, while T is the instantaneous temperature of the system. $Q = (N_f k_B T_0 \tau_T^2)$ is the effective 'mass' of the thermoststat, τ_T is the time constant and N_f is the number of degrees of freedom in the system.

Berendsen themorstat

One of the possible thermostats that can be used is the Berendsen thermostat, which simulates a weak coupling with a first order kinetic to an external bath at an assigned temperature T_0. Temperature variations over time starting from T_0 are corrected by the equation:

$$\frac{dT}{dt} = \frac{T_0 - T}{\tau_T} \tag{3.21}$$

The temperature deviation decays exponentially with a time constant τ_T. This time constant, then, controls the oscillation of the thermostat. The Berendsen algorithm conserves the total momentum but not the energy.

3.3.5 Barostats

The size and shape of the simulation box can be dynamically adjusted by coupling the system to a barostat in order to obtain a desired average pressure (P_{ext}).Two different barostats are commonly used to simulate system in NVT and NPT ensemble: Berendsen and Parrinello-Rahman.

Berendsen barostat

In the NPT ensemble, the dimensions and the shape of the simulation box can be controlled by coupling a barostat to the system. In the Berendsen barostat, a pressure term is added to the equations of motion:

$$\frac{dP}{dt} = \frac{P_0 - P}{\tau_P} \tag{3.22}$$

where τ_P is the time constant of the barostat.

Parrinello-Rahman barostat

The Parrinello-Rahman barostat[187] approach is similar to the Nosé-Hoover temperature coupling, and usually they are combined. The box vectors are represented by the matrix **b**:

$$\frac{d\mathbf{b}^2}{dt^2} = V\ \mathbf{W}^{-1} b'^{-1} (\mathbf{P} - \mathbf{P}_{ref}) \tag{3.23}$$

here V is the volume of the box, W is a matrix parameter determining the strength of the coupling, while $\mathbf{P}$ and $\mathbf{P}_{ref}$ are the current and reference pressures, respectively. With the Parrinello-Rahman algorithm, the equations of motion become:

$$\begin{aligned} \frac{d^2\mathbf{r}_i}{dt^2} &= \frac{\mathbf{F}_i}{m_i} - \mathbf{M}\frac{d\mathbf{r}_i}{dt} \\ \mathbf{M} &= \mathbf{b}^{-1}\left[\mathbf{b}\frac{d\mathbf{b}'}{dt} + \frac{d\mathbf{b}'}{dt}\mathbf{b}\right]\mathbf{b}'^{-1} \end{aligned} \tag{3.24}$$

3.3.6 The Force Field

The force field is the set of functions needed to define the interactions in a molecular system. These may have a wide variety of analytical forms, with some basis in chemical physics, which must be parametrized to give the correct energy and forces. A correct parametrization of the force field is crucial for MD simulations to describe the interactions in the system investigated. The total configuration energy of a molecular system may be written as:

$$\begin{aligned} U(\boldsymbol{r}_1, \boldsymbol{r}_2, \ldots, \boldsymbol{r}_N) = &\sum_{i_{bond}=1}^{N_{bond}} U_{bond}(i_{bond}, \boldsymbol{r}_a, \boldsymbol{r}_b) \\ &+ \sum_{i_{angle}=1}^{N_{angle}} U_{angle}(i_{angle}, \boldsymbol{r}_a, \boldsymbol{r}_b, \boldsymbol{r}_c) \\ &+ \sum_{i_{dihed}=1}^{N_{dihed}} U_{dihed}(i_{dihed}, \boldsymbol{r}_a, \boldsymbol{r}_b, \boldsymbol{r}_c, \boldsymbol{r}_d) \\ &+ \sum_{i=1}^{N-1}\sum_{j>i}^{N} U_{pair}(i, j, \mid \boldsymbol{r}_i - \boldsymbol{r}_j \mid) \\ &\ldots \end{aligned} \tag{3.25}$$

where U_{bond}, U_{angle}, U_{dihed}, U_{pair} are empirical interaction functions representing chemical bonds, valence angles, dihedral angles and pair-body. The first three are regarded as *intra*-molecular interactions and the last as *inter*-molecular interaction. The position vectors $\boldsymbol{r}_a$, $\boldsymbol{r}_b$, $\boldsymbol{r}_c$ and $\boldsymbol{r}_d$ refer to the positions of the atoms specifically involved in a given interaction. The numbers N_{bond}, N_{angle} and N_{dihed} refer to the total numbers of these respective interactions present in the simulated system, and the indices i_{bond}, i_{angle} and i_{dihed} uniquely specify an individual interaction of each type, all of which must be individually cited. The indices i and j appearing in the pair-body term indicate the atoms involved in the interaction. In general, it is assumed that the pair-body terms arise from van der Waals and/or electrostatic (Coulombic) forces. The former are regarded as short ranged interactions and the latter as long ranged. The non-bonded pair interactions are calculated using a Verlet neighbour list[188], which is reconstructed at defined intervals during the simulations. This list records the indices of all 'secondary' atoms within a cut-off radius (r_{cut}) from each 'primary' atom.

Bonded interactions

Bond potential

Bond interactions are usually described by two potential forms, one anharmonic (or Morse) and one harmonic. The Morse potential is characterized by an asymmetrical potential well and null forces at infinite distance. The function is described by the equation:

$$V_{morse}(r_{ab}) = D_{ab}\ [1 - \exp\ (-\beta_{ab}\ (r_{ab} - r_0))]^2 \tag{3.26}$$

where D_{ab} is the depth of the well, β_{ab} defines the steepness of the well, and r_0 is the equilibrium distance. The steepness parameter β_{ab} can be expressed in terms of the reduced mass of the two bonded atoms, the fundamental vibration frequency ω and the well depth D_{ab}:

$$\beta_{ab} = \omega_{ab}\ \sqrt{\frac{\mu_{ab}}{2D_{ab}}} \tag{3.27}$$

Since $\omega = \sqrt{\frac{k_{ab}}{\mu}}$, where k_{ab} is the bond force constant, β_{ab} can be written as:

$$\beta_{ab} = \sqrt{\frac{k_{ab}}{2D_{ab}}} \tag{3.28}$$

Since the Morse potential needs the definition of three parameters and usually bonds do not deviate significantly during molecular mechanics calculations, the harmonic potential is commonly used. In this potential, the energy varies with the square of the equilibrium distance displacement of the bond:

$$V(r_{ab}) = \frac{1}{2}\ k_{ab}(r_{ab} - r_0)^2 \tag{3.29}$$

This potential correctly approximates the shape of the energy curve potential in the well area, where the molecules are at the equilibrium, whereas it loses accuracy as it moves away from the equilibrium.

Angle potential

The deviation of bonded angle interactions from the reference value is usually described by a harmonic potential:

$$V(\theta_{abc}) = \frac{1}{2}\ k^{\theta}_{abc}(\theta_{abc} - \theta_0)^2 \tag{3.30}$$

where θ_0 is the equilibrium value of the angle, k^{θ}_{abc} is the force constant and θ_{abc} is the angle formed between the atoms $\mathbf{r}_a$, $\mathbf{r}_b$ and $\mathbf{r}_c$. The force constants k_{abc} for angles are usually weaker than the bonded ones.

Dihedral potential

The existence of energy barriers at the chemical bonds rotation is crucial in order to understand the structural and conformational properties of the molecules.

The torsional potential (or dihedral) describes the interaction resulting from the torsional forces within the molecules and is applied to four atomic positions. Torsion angles in a molecule can be defined with two different dihedral potentials: proper and improper. The proper dihedral interactions are described by the function:

$$V(\phi_{abcd}) = k_\phi(1 + cos(n\phi - \phi_0)) \tag{3.31}$$

where k_ϕ represents the height of the energy barrier, ϕ and ϕ_0 are the torsion angle and the equilibrium torsion angle, respectively. This proper potential is known as *periodic*. Another potential for the proper dihedrals is described by the Ryckaert-Bellemans function:

$$V_{rb}(\phi_{abcd}) = \sum_{n=0}^{5} C_n(cos(\psi))^n \tag{3.32}$$

where $\psi = \phi - 180°$.
Improper dihedrals are meant to keep planar the planar groups, such as aromatic cores, or to prevent that chiral molecules convert into their specular image. The improper dihedral potential can be written as:

$$V_i(\xi_{abcd}) = \frac{1}{2}\ k_\xi(\xi_{abcd} - \xi_0)^n \tag{3.33}$$

Non-bonded interactions

Non-bonded interactions are divided in weak interactions (Van der Waals), expressed via potentials containing repulsion and dispersion terms (Lennard-Jones and Buckingham), and electrostatic interactions (Coulomb). These interactions are calculated for each neighbouring particle that are within a certain radius.

Lennard-Jones potential

The most familiar van der Waals pair interaction potential is the Lennard-Jones:

$$V_{LJ} = 4\epsilon\left[\left(\frac{\sigma}{r_{ij}}\right)^{12} - \left(\frac{\sigma}{r_{ij}}\right)^{6}\right], r_{ij} > r_{cut-off} \tag{3.34}$$

where r_{ij} is the distance between two interacting particles i and j, ϵ is the depth of the potential well and σ is the distance at which V_{LJ}=0. This potential is repulsive at short range and attractive at long range. To avoid excessive computational costs, this potential is truncated at a specific distance $r_{cut-off}$.

Buckingham potential

The Buckingham potential[189] has a more flexible and realistic repulsion term than the Lennard-Jones interaction, but is also more expensive to compute.

The potential form is:

$$V_B(r_{ij}) = A_{ij}\exp(-B_{ij}r_{ij}) - \frac{C_{ij}}{r^6} \tag{3.35}$$

where A_{ij},B_{ij} and C_{ij} are constants. The two terms on the right-hand side constitute a repulsion and an attraction, because their first derivatives with respect to r_{ij} are negative and positive, respectively.

Coulomb potential

Electrostatic interactions between two particles within the $\mathrm{r}_{cut-off}$ are calculated as the sum of the interactions between two point charges with the Coulomb potential:

$$V_c = \frac{1}{4\pi\varepsilon_0}\frac{q_i q_j}{r_{ij}} \tag{3.36}$$

where q_i and q_j are the charges of the two particles i and j, r_{ij} the distance between them and ε_0 the vacuum dielectric constant.

Ewald sum

The Ewald sum is a computational technique for calculating electrostatic interactions in a periodic (or pseudo-periodic) system[188]. The basic model for a neutral periodic system is a system of charged point ions mutually interacting via the Coulomb potential:

$$E_C = \frac{1}{2}\sum_{|n|=0}\sum_{i=1}^{N}\sum_{j=1}^{N}\frac{q_i q_j}{4\pi\varepsilon_0|\mathbf{r}_{ij}+\mathbf{n}|} \tag{3.37}$$

The Ewald method divides the electrostatic calculations in a *short-range* and a *long-range* part. The *short-range* part is evaluated in real space, calculating the effect of a potential generated by a distribution of point charges, which quickly decays at long distances, converging rapidly in the real space. The *long-range* part, instead, is solved as a Fourier series in reciprocal space. An efficient implementation of the Ewald sum is the particle mesh Ewald (PME) scheme[190]. Here, Fourier calculations are made by using a fast Fourier transform (FFT) on a discrete mesh. This improves the computational efficiency, in fact PME scales as $\mathcal{O}(NlogN)$ whereas the direct sum as $\mathcal{O}(N^2)$.

Cutoff restrictions

The minimum image convention implies that the cutoff radius used to truncate non-bonded interactions must not exceed half the shortest box vector:

$$R_c < \frac{1}{2}\min(|\,\boldsymbol{a}\,|,|\,\boldsymbol{b}\,|,|\,\boldsymbol{c}\,|), \tag{3.38}$$

otherwise more than one image would be within the cutoff distance of the force. When a macromolecule, such as a protein, is studied in solution, this restriction does not suffice. In principle a single solvent molecule should not be able to

'see' both sides of the macromolecule. This means that the length of each box vector must exceed the length of the macromolecule in the direction of that edge *plus* two times the cutoff radius R_c. It is common to compromise in this respect, and make the solvent layer somewhat smaller in order to reduce the computational cost. For efficiency reasons the cutoff with triclinic boxes is more restricted. For grid search the extra restriction is weak:

$$R_c < \min(a_x, b_y, c_z) \tag{3.39}$$

3.4 Coarse-grained models

Atomistic models provide a detailed description of the interactions between atoms, but at high computational cost. Therefore, the use of atomistic models limits the size of the samples and the time scale of the simulations, usually shorter than relevant processes occurring in materials at the nanoscale. Coarse-graining (CG) thecniques are commonly applied to extend the MD simulations both in time- and length- scales[57, 138–145]. Namely, the number of degrees of freedom of a molecular system is reduced by reducing the interaction sites, i.e. substituting groups of atoms with a single particle with shape, dimensions and properties related to the atomistic counterpart, resulting in a model that is computationally less expensive than the equivalent fully atomistic model. The choice of the beads constituting the coarse-grained model depends basically on the class of molecule considered. However, the same molecules can be represented by beads comprising more or less atoms, leading to models with compromises between accuracy and transferability, i.e. models capable of describing the general dynamics of systems with different compositions and different configurations [191]. Coarse-grained models are widely employed for simulating polymers and peptides, but also for small organic molecules (see Chapter 6). An example of the coarse-graining of a polymer is presented in Figure 3.3. Effective bonded and non-bonded interactions are typically derived by fitting the interaction potential of an atomistic trajectory by applying a Boltzmann inversion.

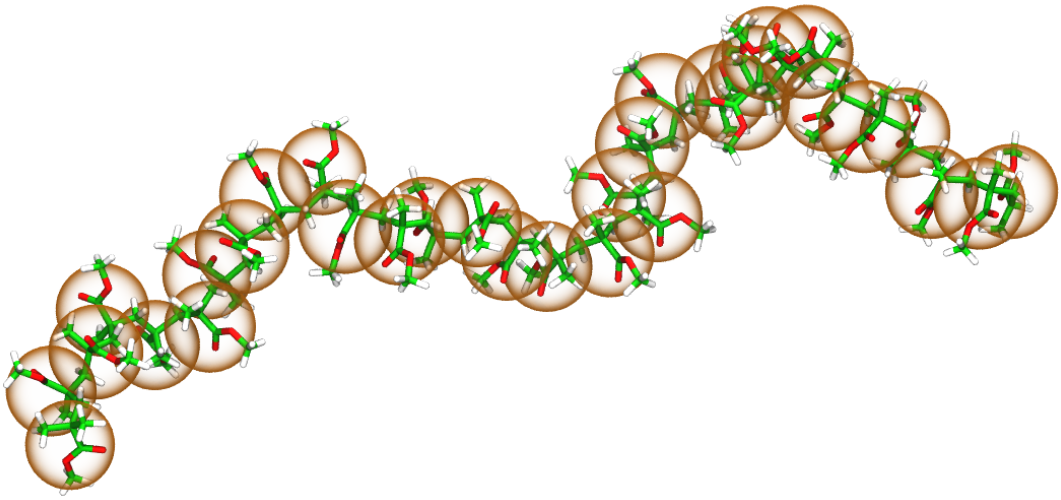

FIGURE 3.3: Example of the coarse-graining of a PMMA chain. In this figure, each polymer group is represented by an orange CG spherical bead.

Boltzmann inversion

The probability of a certain configuration in the canonical ensemble is Boltzmann distributed with respect to a degree of freedom q, such as:

$$P(q) = \frac{\exp(-\beta U(q))}{Z} \tag{3.40}$$

here $U(q)$ is a potential, $\beta = 1/k_B T$ and Z is the partition function given by $Z = \int(-\beta U(q))dq$. The probability distribution P is known by atomistic trajectories, then it is possible to invert the equation 3.40 in order to obtain the potential:

$$U(q) = -k_B T \ \ln(P(q)) \tag{3.41}$$

hence, extracting an atomistic property from a trajectory, the interaction potential is obtain by fitting the data given by the equation 3.41. Usually, a single Boltzmann inversion is used for bonded potentials.

Iterative Boltzmann inversion

An implementation of this method is the iterative Boltzmann inversion (IBI). In this method, the potential obtained by a single Boltzmann inversion U_i is compared to a reference value and the estimation of the final potential is improved iteratively by the equation:

$$U_{i+1} = U_i - k_B T \ln\left(\frac{P_i(q)}{P_{ref}(q)}\right) \tag{3.42}$$

until the potential obtained by the Boltzmann inversion is in good agreement with the reference. This method is mostly used for non-bonded interactions.

Gay-Berne potential

The Gay-Berne (GB) pair potential[192] is a simple one-site attractive–repulsive interaction, used in simulations of liquid crystalline systems. The GB potential is an anisotropic form of the Lennard-Jones 6-12 potential and can be written as:

$$\begin{aligned} U(\hat{\mathbf{u}}_\mathrm{i}, \hat{\mathbf{u}}_\mathrm{j}, \hat{\mathbf{r}}_\mathrm{ij}) &= 4\varepsilon(\hat{\mathbf{u}}_\mathrm{i}, \hat{\mathbf{u}}_\mathrm{j}, \hat{\mathbf{r}}_\mathrm{ij}) \\ &\times \left[\left(\frac{\sigma_c}{r_{ij} - \sigma(\hat{\mathbf{u}}_\mathrm{i}, \hat{\mathbf{u}}_\mathrm{j}, \hat{\mathbf{r}}_\mathrm{ij}) + \sigma_\mathrm{c}}\right)^{12} - \left(\frac{\sigma_c}{r_{ij} - \sigma(\hat{\mathbf{u}}_\mathrm{i}, \hat{\mathbf{u}}_\mathrm{j}, \hat{\mathbf{r}}_\mathrm{ij}) + \sigma_\mathrm{c}}\right)^{6}\right] \end{aligned} \tag{3.43}$$

where $\hat{\mathbf{r}}_\mathrm{ij}$ is the intermolecular distance between the particles i and j, $\hat{\mathbf{u}}_\mathrm{i}$ and $\hat{\mathbf{u}}_\mathrm{j}$ are unit vectors representing the orientations of the molecules. The function $\varepsilon(\hat{\mathbf{u}}_\mathrm{i}, \hat{\mathbf{u}}_\mathrm{j}, \hat{\mathbf{r}}_\mathrm{ij})$ defines the angular dependent potential well depth and also depends on the interaction parameters ε_x, ε_y and ε_z, which are directly related to the potential well depths for two GB particles approaching with fixed parallel orientations along the three Cartesian directions. $\sigma(\hat{\mathbf{u}}_\mathrm{i}, \hat{\mathbf{u}}_\mathrm{j}, \hat{\mathbf{r}}_\mathrm{ij})$ represent

the anisotropic contact term which approximates the geometrical contact distance between two ellipsoids and depends on the axes lengths σ_x, σ_y, σ_z. This potential is commonly used to model the non-bonded interactions between aromatic cores. In this thesis, this potential was used to model the CG interactions between perylene cores of PTCDI-C13.

3.5 Metadynamics

Metadynamics is a technique used for reconstructing the free-energy surface of a system as a function of few selected degrees of freedom, referred to as the collective variables (CVs)[36, 117, 193–195]. In metadynamics, sampling is accelerated by a history-dependent bias potential, which is adaptively constructed in the space of the CVs. In particular, during the simulation, a positive Gaussian potential is added to the real energy landscape of the system, discouraging it to come back to the previous point. During the evolution of the simulation, more and more Gaussians sum up, until the system explores the full energy landscape. At this point the energy landscape can be recovered as the opposite of the sum of all Gaussians. Metadynamics is often performed to study system characterized by configurations separated by high energy barriers, so that classical MD timescale cannot sample them, or that the transition between two configurations is determined by rare events. Metadynamics does not require an initial estimate of the energy landscape to explore, but the choice of the correct CV to investigate is crucial in order to investigate the free energy of the system correctly. This choice, however, is not always trivial, mostly for complex systems. Let $S(q)$ to be the selected degree of freedom of the system, i.e. the CV, the metadynamics bias potential at the time t can be written as:

$$V_G(S,t) = \int_0^t dt' \omega \exp\left(- \sum_{i=1}^{d} \frac{(S_i(q) - S_i(q(t')))^2}{2\sigma_i^2} \right) \tag{3.44}$$

where ω is an energy rate and σ_i correspond to the width of the Gaussian for the ith CV. The energy rate is constant and can be expressed in terms of a Gaussian height W and a deposition stride τ:

$$\omega = \frac{W}{\tau} \tag{3.45}$$

The effect of the metadynamics bias potential (V_G) is to push the system away from local minima to visit new regions of the phase space, exploring all the free energy surface (FES). In the long time limit, V_G provides and unbiased estimate of the underlying free energy:

$$V_G(S, t \to \infty) = -F(S) + C \tag{3.46}$$

The free energy F(S) is defined as:

$$F(S) = -\frac{1}{\beta}\, ln \left(\int dq\ \delta(S - S(q))\ e^{-\beta U(q)} \right) \tag{3.47}$$

where $\beta = (k_B T)^{-1}$, k_B is the Boltzamnn constant, T the temperature of the system and U(q) the potential energy function. In standard metadynamics, Gaussians of constant height are added for the entire course of a simulation. As a result, the system is eventually pushed to explore high free-energy regions and the estimate of the free energy calculated from the bias potential oscillates around the real value. In well-tempered metadynamics, the height of the Gaussian is decreased with simulation time according to:

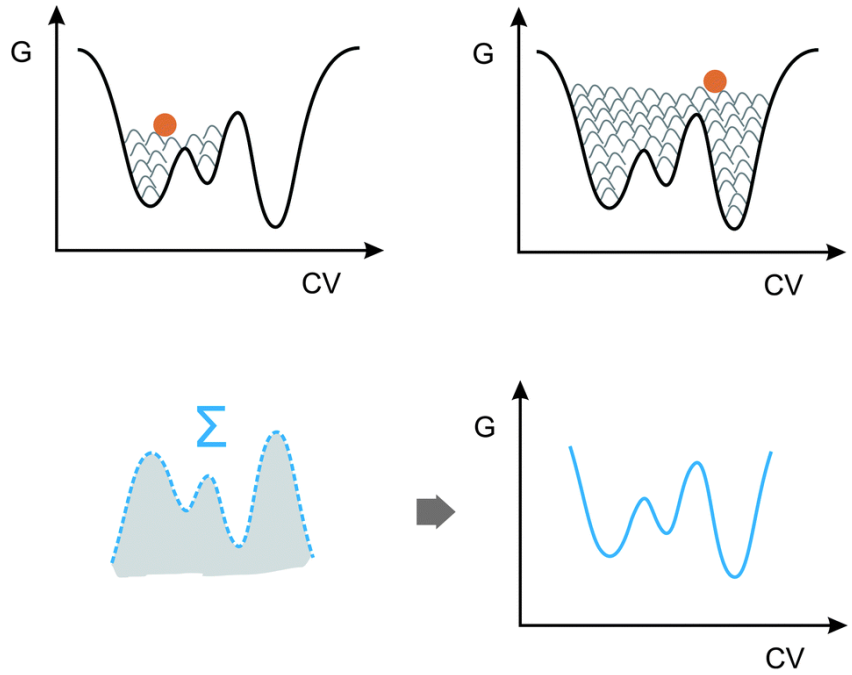

FIGURE 3.4: Schematic representation of the metadynamics technique. Adapted from Ref.[193].

$$W = \omega\tau_G e^{-\frac{V_G(S,t)}{k_B \Delta T}} \tag{3.48}$$

where $\omega\tau_G$ is an initial Gaussian height, Δ T an input parameter with the dimension of a temperature, and k_B the Boltzmann constant. With this rescaling of the Gaussian height, the bias potential does not fully compensate the underlying free energy, but it converges to:

$$V_G(s, t \to \infty) = -\frac{\Delta T}{T + \Delta T} F(S) + C \tag{3.49}$$

where T is the temperature of the system. In the long time limit, the CVs sample an ensemble at a temperature T + ΔT which is higher than the system temperature T. In particular, ΔT = 0 corresponds to standard molecular dynamics, whereas $\Delta T \to \infty$ corresponds to standard metadynamics. In well-tempered metadynamics, the *biasfactor* is the ratio between the temperature of the CVs (T + ΔT) and the system temperature (T):

$$\gamma = \frac{T + \Delta T}{T} \tag{3.50}$$

The biasfactor should thus be carefully chosen in order for the relevant free-energy barriers to be crossed efficiently in the time scale of the simulation. In this thesis, metadynamics calculations were performed using the Plumed plugin[196] included in the LAMMPS package[184].

3.6 Modelling of charge transport

In organic materials, a charge carrier residing on a molecular site tends to polarize its neighboring region, leading to the formation of quasi-particles, *polarons*, in which the electronic charge is dressed by phonon clouds. Phonons are quantized modes of vibrational energy arising from the collective oscillations of atoms within a crystal[116]. Unlike inorganic materials, in these materials the interactions between electrons and phonons are comparable or even larger than the electronic interactions. The charge transport properties in organic semiconductors are affected by several factors, including the system environment, the molecular geometry, the intermolecular distance, and the molecular packing [116], hence to the small deviation of atoms respect to their equilibrium position, referred to as electron-phonon coupling. This can be subdivided in *local* and *nonlocal* coupling. The former refers to the modulations of site energies within the organic crystal, while the latter refers to the modulation of the transfer integrals by lattice phonons. Another parameter strongly affecting the charge transport properties in organic materials is the electronic coupling, which is connected to the overlap between the orbitals of the dimers participating in the charge transfer reaction, and hence is very sensitive to relative molecular positions and orientations of the dimers. The electronic coupling element (t_{ab}) between two species, a and b, can be evaluated as $t_{ab} = \langle \Psi_a | H | \Psi_b \rangle$, where H is the Hamiltonian of the system, Ψ_a and Ψ_b are the wavefunctions of two charge-localized states. The most simple method used to determine electronic coupling values is called energy splitting in dimers (ESID) method, based on the assumption that, at the transition state, the energy difference E_2 - E_1 between the adiabatic states Ψ_1 and Ψ_2 corresponds to $2t_{ab}$, then $t_{ab} = \frac{(E_2 - E_1)}{2}$. By applying the Koopmans' theorem[197], the method becomes the KT-ESID and the transfer integral for electron [hole] transfer from the electronic coupling is obtained by:

$$t = \frac{\epsilon_{L+1[H]} - \epsilon_{L[H-1]}}{2} \tag{3.51}$$

where $\epsilon_{L[H]}$ and $\epsilon_{L+1[H-1]}$ are the energies of LUMO and LUMO+1 [HOMO and HOMO-1] levels taken from the closed-shell configuration of the neutral state of a dimer.

Electron-transfer theory

Electron transfer processes are driven by electron-electron and electron-vibration interactions. In particular, an electron is transferred from an initial orbital to a final orbital. According to the perturbation theory, the probability of the transition between an initial state ψ_i to a final state ψ_f, driven by a perturbation V, can be written as:

$$P_{if} = \frac{1}{\hbar^2} |\langle \psi_i | V | \psi_f \rangle|^2 \left[\frac{sin(\omega_{fi}\ t/2)}{\omega_{fi}\ /2} \right]^2 \tag{3.52}$$

where t denotes the time, ω_{fi} the transition energy between the electronic states i and f, $\hbar$ is the Planck constant and $\langle \psi_i | V | \psi_f \rangle$ is the electronic coupling matrix

element. The charge transport properties in organic materials depend strongly on the extent of the electronic coupling, defined by the matrix element $V_{if} = \langle\psi_i|V|\psi_f\rangle$. If the final state has a continuous distribution of final electronic states, the density of the final state $\rho(\mathrm{E}_f)$ can be introduced. The transition probability per unit time, or transition rate (k_{if}), adopts the Fermi's Golden Rule:

$$k_{if} = \frac{2\pi}{\hbar}|V_{if}|^2\rho(E_f) \tag{3.53}$$

and the expression for the rate obtained within the Franck-Condon approximation becomes:

$$k_{if} = \frac{2\pi}{\hbar}|V_{if}|^2(FCWD) \tag{3.54}$$

here FCWD is the Franck-Condon weighted density of states. When assuming that all vibrational modes are classical ($\hbar\omega_i << k_BT$), the FCWD follows a standard Arrhenius type equation:

$$FCWD = \sqrt{\frac{1}{4\pi k_BT\lambda}}\exp\left[-\frac{(\Delta G^0+\lambda)^2}{4\lambda k_BT}\right] \tag{3.55}$$

hence the transition rate takes the semiclassical Marcus theory expression:

$$k_{if} = \frac{2\pi}{\hbar}|V_{if}|^2\sqrt{\frac{1}{4\pi k_BT\lambda}}\exp\left[-\frac{(\Delta G^0+\lambda)^2}{4\lambda k_BT}\right] \tag{3.56}$$

where λ represents the reorganization energy induced by the electron transfer and $\Delta\mathrm{G}^0$ is the variation of the Gibbs free energy during the transition. The reorganization energy λ is expressed as the sum of an inner and an outer contributions. The inner (intramolecular) reorganization energy arises from the change in equilibrium geometry of the donor and the acceptor sites upon the electron transfer. The outer reorganization energy, instead, depends on the electronic and nuclear polarization/relaxation of the surrounding medium.

Chapter 4

Morphology and electronic properties of two-dimensional PTCDI-C13 aggregates

The outstanding charge mobilities observed in devices[25] are usually ascribed to the peculiar molecular structure of PTCDI-C13 (see Figure 2.8a). Moreover, the interplay between the supramolecular arrangement of alkyl chains and the π-π stacking interactions among perylene diimide cores can be expected to represent the primary phenomenon behind the formation of ordered PTCDI-C13 layered aggregates, observed in several experiments[198–200]. Despite the large amount of work performed on the characterization of PTCDI-C13 thin films at heterointerfaces[5, 7, 24, 63, 199, 201], the details of crystal formation and packing, at the molecular level, still remain elusive. Indeed, the typical polycrystallinity of organic layered aggregates[198–200] hinders the accurate characterization of in-plane packing in PTCDI-C13 thin-films by standard XRD techniques[24, 25, 202, 203]. The most accurate available structural information to date suggests formation of ordered island of PTCDI-C13 with a typical terrace height that is compatible with molecules arranged in a stand-up configuration[7, 24]. The resulting morphology of PTCDI-C13 thin-films in best-performing devices consists essentially of compact layers of quasi-2D polycrystalline aggregates[63], with molecules oriented in a direction that is favourable to charge transport. However, details on the peculiar realization of the intermolecular π-stacking, a comprehensive rationalization of structural and dynamical aspects of aggregation of PTCDI-C13 layers and the relationships with growth conditions and processing are still missing. A detailed knowledge of the structure of the involved crystalline aggregates, at the atomistic level, constitutes thus a pivotal field of investigation for the optimisation of materials and devices. In this chapter, the study on morphological and electronic properties of 2D strucures of PTCDI-C13 is presented. To this end, three putative crystal structures of PTCDI-C13 layers, differing essentially in the relative orientation of the perylene cores, were modeled. The arrangement of PTCDI-C13 molecules in each of these tentative structures has been inferred from the known crystal structure of thin-films of similar organic systems[11]. Namely, 2D crystals with perylene cores arranged in a cofacial (CF), staggered (ST) and herringbone (HB) configuration, respectively, commonly observed in perylenes, were considered[25, 85,

204–206]. Investigations on 2D structures elucidate the morphology of PTCDI-C13 in monolayers and in layer-by-layer growth, that is, in aggregation conditions that can be considered as the most favourable to charge transport. Indeed, although the nature and morphology of the substrate, as well as growth conditions and material processing, are known to greatly affect the aggregation of organic overlayers[5, 7, 25, 203], detailed studies on ideal 2D structures can assess the intrinsic propensity of PTCDI-C13 to form ordered layers at interfaces. The analysis of the 2D crystal structures, their morphology and dynamics, and the relationship with the resulting electronic properties allows to understand how these parameters impact on the performances of devices.

The work presented in this chapter has been published in Ref. [35].

4.1 Morphology of 2D structures of PTCDI-C13

The structures of the different 2D crystals of PTCDI-C13 considered were initially investigated by MD simulations and analysed in terms of structural parameters. To this end, models of the three (CF, ST and HB) structures were initially prepared by inserting dimers in a monoclinic (CF, HB) and orthorhombic (ST) unit cell, as in Figure 4.1. The initial cell parameters of the CF phase (Z=2) were taken from Tatemichi *et al.*[25]. From these parameters, a 2D supercell was built, by replicating the experimental unit cell along the [1 0 0] and [0 1 0] directions. The simulation replicated box contained 24 molecules. Similar model systems were built for the ST and HB phases. Periodic boundary conditions in 3 dimensions were used for the simulation of 2D systems, by inserting a vacuum region (about 20 Å) along the z direction. Electrostatic interactions were treated by the particle-mesh Ewald (PME) method and a cut-off of 10.0 and 14.0 Å was used for Coulomb and van der Waals interactions, respectively. The Nose–Hoover thermostat[185, 186] was used for simulations in the canonical (NVT) ensemble, and the Parrinello–Rahman barostat[187] was added in variable-cell (NPT) simulations, with time constants of 1.0 ps and 10.0 ps, respectively. All the MD simulations were performed by using the GROMACS package[183]. Structures were initially relaxed to the local energy minimum by steepest descent optimisation, then equilibrated at 300 K in NPT ensemble for 1 ns and, in analogy with experimental processing[5, 7, 25, 63, 198, 203], annealed at 400 K for 1 ns. Annealed structures were then relaxed and equilibrated to 300 K for 1 ns. All parameters of the two dimensional cell (a, b, and γ) were allowed to relax during NPT simulations. A further cooling to negligible kinetic energies and final steepest descent relaxation led to optimised structures, used to evaluate structural parameters (shown in Table 4.1) and as input for DFT calculations. The supercells of all 2D crystals exhibit remarkable long-range

TABLE 4.1: Cell parameters for PTCDI-C13 crystals (a,b:Å; γ:degrees and surface densities (mol nm^{-2}) obtained by MD simulations.

Structure	a	b	γ	Density
CF	8.78	8.51	81.49	2.71
ST	7.48	8.62	84.72	3.06
HB	7.81	8.76	72.49	3.07

translational crystal order upon MD relaxation at room temperature and can be reduced to a unit cell with Z=2. The optimised 2D structures of PTCDI-C13 are shown in Figure 4.2. Notably, the computed cell parameters of the CF and ST crystals are compatible with available experimental data[25]. The computed surface densities, which can be related to molecular packing in 2D aggregates, are 2.71 mol/nm^2, 3.06 mol/nm^2 and 3.07 mol/nm^2 for the CF, ST and HB models, respectively (see Table 4.1). The slightly larger surface density

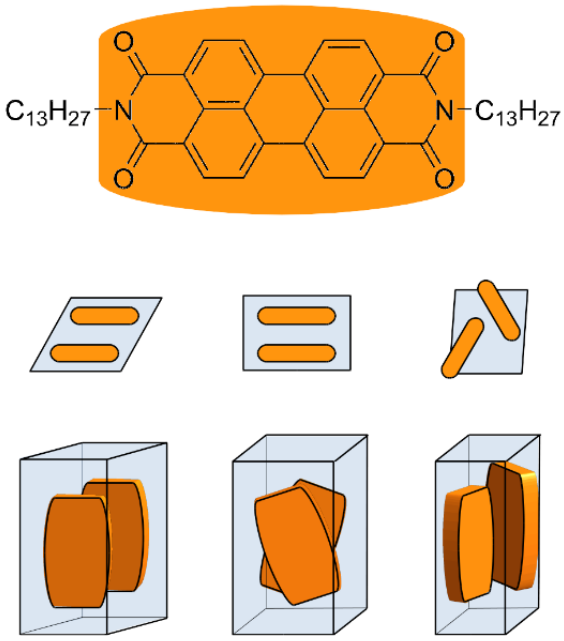

FIGURE 4.1: Structure of the PTCDI-C13 molecule (top) and cartoons of the initial two-dimensional crystals of the CF (bottom left), ST (bottom center) and HB (bottom right) crystals. Adapted from Ref. [35].

of the ST and HB polymorphs can be ascribed to the peculiar relative orientation of the perylene cores, allowing the minimization of the steric hindrance of the alkyl chains and, in the ST crystal, to strong π-stacking interactions. Inversely, the more symmetric CF structure leads to less effective space filling and, consequently, to a lower surface density.

4.2 Structural parameters

The molecular packing in 2D crystals was further assessed by computing the radial pair distribution function g(r) between centers of mass of PTCDI-C13 molecules. The computed g(r) of the relaxed 2D crystals for models of the three structures considered is shown in Figure 4.3a. The most intense peaks of the g(r) (3.75 Å, 4.55 Å and 5.85 Å for the ST, CF and HB structures, respectively) correlate with the crystal packing of PTCDI-C13 molecules along the [1 0 0] crystallographic direction, which coincides with the axis of main π-π stacking, perpendicular to the aromatic rings, for the CF and ST structures. Less intense g(r) peaks, between 7.5 and 9.5 Å, correspond to crystal packing along the [0 1 0] direction for CF and ST structures, and to a combination of [1 0 0] and [0 1 0] ordering for the more isotropic HB crystal. The preferential crystal packing of CF and ST structures along the [1 0 0] direction agrees with the observed needle-like growth of nanoscale perylene aggregates[5, 199, 207]. However, charge transport properties of materials based on the perylene

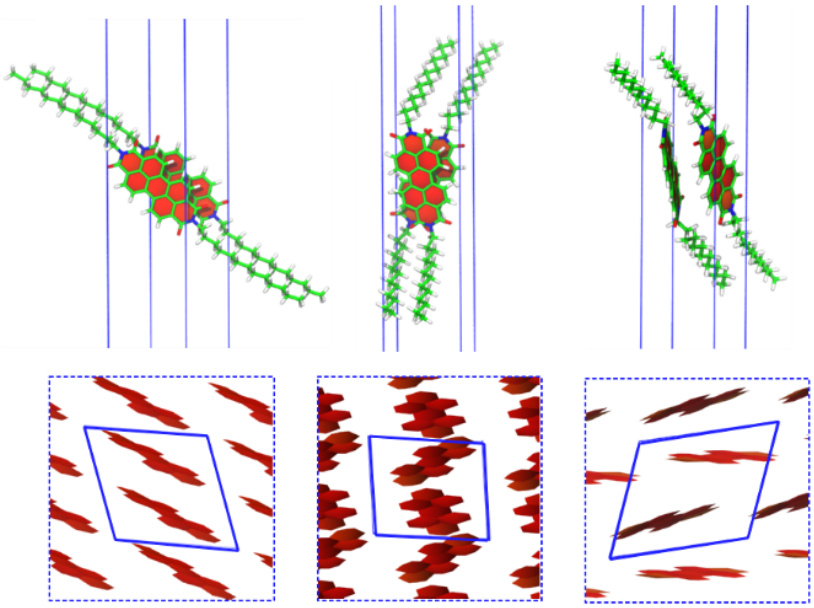

FIGURE 4.2: Optimised structures of the CF (left), ST (center) and HB (right) 2D crystals of PTCDI-C13. Adapted from Ref. [35].

diimide unit are also greatly affected by the relative orientation of neighboring π-cores[128]. The relative orientation of neighboring molecules in 2D PTCDI-C13 aggregates was evaluated in terms of two order parameters, defining the twist (θ) and tilt (φ) angles between the two planes of the perylene cores, respectively, as shown in the inset of Figure 4.3b. According to this definition, the pair of angles [θ,φ] results about [0, 0], [30, 0] and [0, 30] for the CF, ST, and HB structures, respectively (see Figure 4.3b). The angular structural parameters [θ, φ] can be used to identify the different PTCDI-C13 2D crystals, thus allowing a detailed analysis of morphology and structural modifications in both layers and nanoaggregates.

4.3 Stability of 2D aggregates

To explore the thermal stability of PTCDI-C13 crystals, NPT simulations at higher temperatures were also performed. The structure of the CF crystal is essentially unchanged by relaxation at 500 K for about 2 ns. Also, no relevant structural changes was observed upon annealing of the HB crystal at 500 K. However, variable-cell MD relaxation of the ST structure at 500 K leads to a complete phase transition to the CF crystal, suggesting a viable low-energy dynamical path for the interconversion between these two forms. To further assess the stability and the dynamical behavior of the different 2D structures and in realistic finite-size systems, MD simulations on small planar (about 3x3 nm) non-periodic clusters of PTCDI-C13 were also performed in non-periodic conditions. Clusters of the CF crystal were found to be stable under MD at

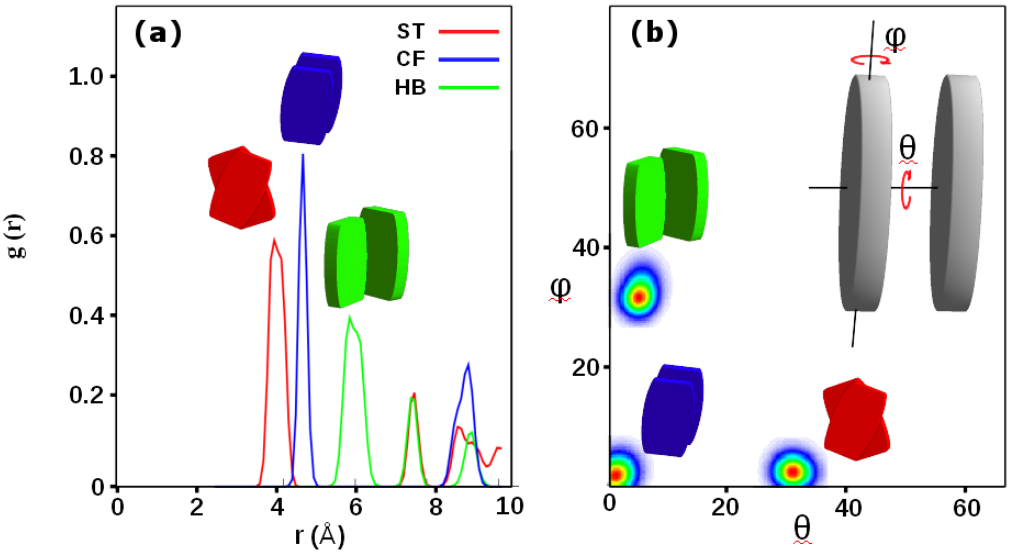

FIGURE 4.3: Radial distribution function (a) and angular order parameters (b) for the three PTCDI-C13 2D crystals considered (CF: blue; ST: red; HB: green) at 300 K. Adapted from Ref. [35].

annealing temperatures higher than 500 K on timescales of about 10 ns. However, the analysis of the structure obtained by annealing the CF cluster to 700 K reveals a still relatively ordered arrangement of PTCDI-C13 molecules, with coexistence of aggregates in liquid-crystal CF and ST forms, as shown in Figure 4.4a. Likewise, annealing the HB cluster at high temperature (about 700 K) induces molecular aggregation into a similar polycrystalline structure composed of CF and ST phases (see Figure 4.4b). Inversely, the ST cluster undergoes a thermally-induced rearrangement to the CF form, as observed for the periodic system, by annealing at 400 K (see Figure 4.4c), thus at temperatures lower than those generally used to anneal PTCDI-C13 thin-films[69]. Therefore, at high temperatures the free energy basins corresponding to both the CF and ST configurations are sampled, whereas relaxation toward the global minimum configuration is observed at lower temperatures. The remarkable crystal ordering at room temperature in 2D crystals, the coexistence of CF and ST liquid crystal phases at high temperatures and the abrupt interconversion from the ST to the CF structure at relatively low temperatures indicate the CF crystal as the most stable and suggest the occurrence of a relatively low energy barrier for transition from the ST metastable phase. Moreover, the HB crystal constitutes a high-energy metastable form of PTCDI-C13 and, as such, not likely to be observed in 2D aggregates. Accordingly, the CF crystal is expected to dominate in the thermodynamically controlled growth of aggregates, whereas both CF and ST forms may coexist in particular environments. These findings agree with recent experiments, where formation of cofacial aggregates of PTCDI-C13 is commonly observed[25, 203, 207]. It must be pointed out that the energy landscape sampled by MD simulations, referring to 2D layers and clusters in

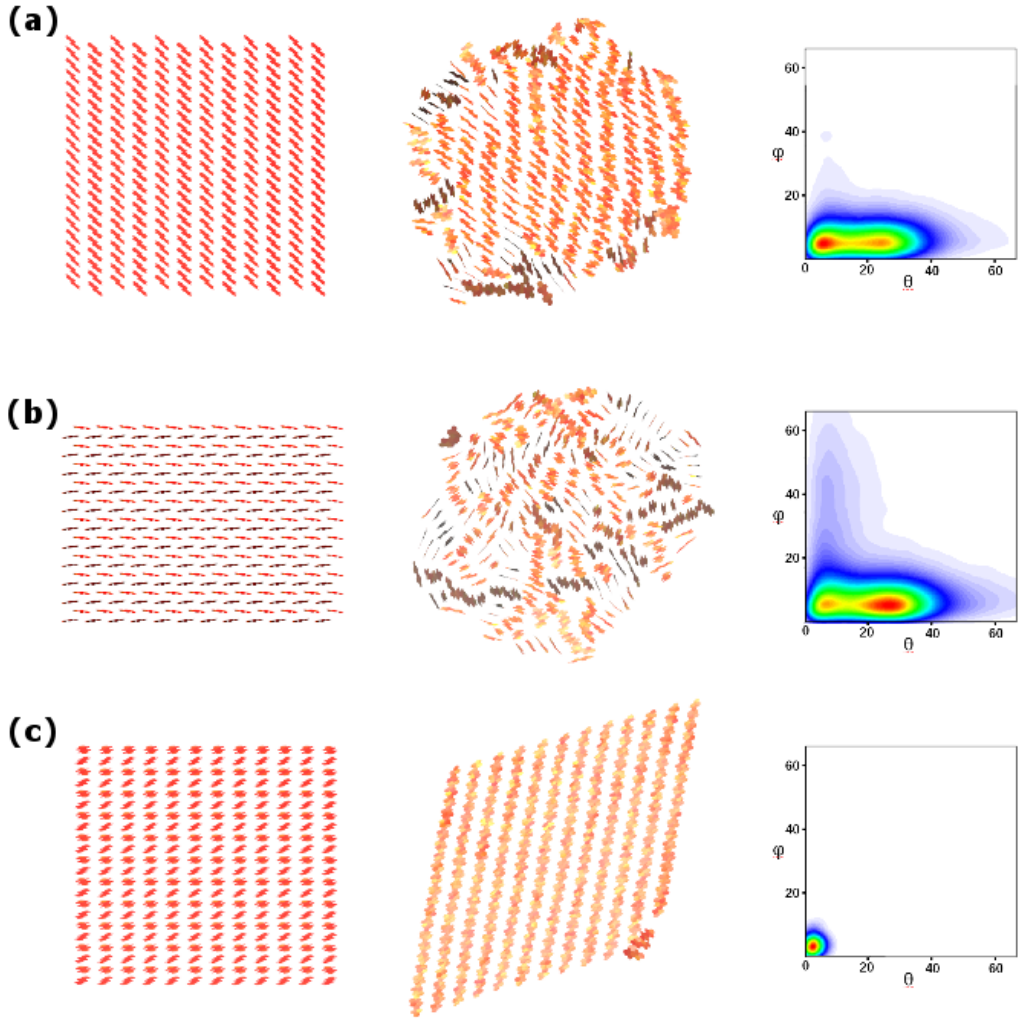

FIGURE 4.4: Initial (left) and final (center) structures of non-periodic PTCDIC13 clusters and angular order parameters for the final structure (right) for (a) relaxation of the CF cluster at 700 K; (b) relaxation of the HB cluster at 700 K; (c) relaxation of the ST cluster at 400 K, inducing a phase transition to the CF phase. Adapted from Ref. [35].

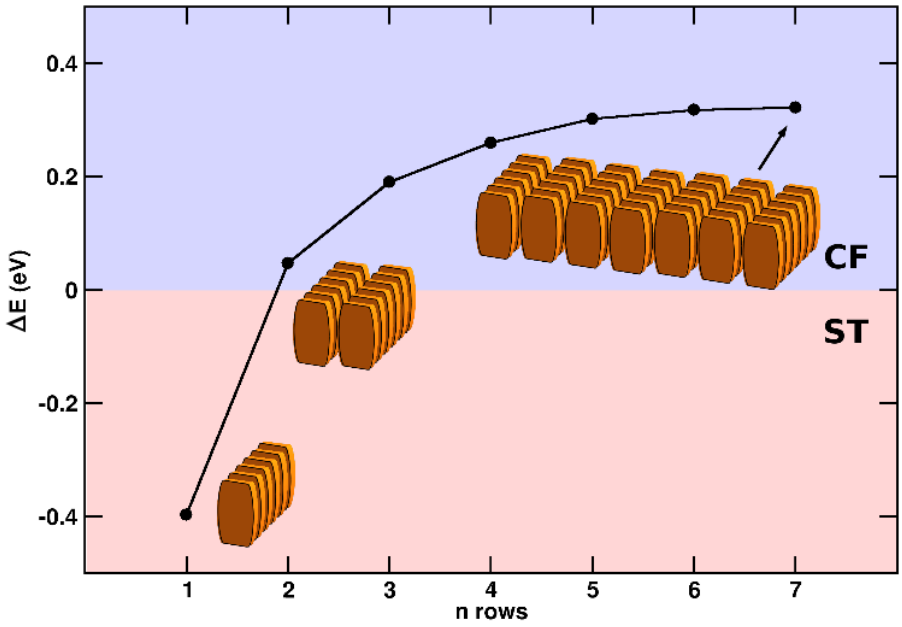

FIGURE 4.5: Difference between the mean potential energies (at 300 K) of the CF and ST nanorods, with periodicity along the main axis only, as a function of the number of rows along the in-plane non-periodic direction. Adapted from Ref. [35].

vacuum, may significantly be altered upon interaction with a substrate. However, the propensity to ordered aggregation and the relative stability of the structures considered can be expected to hold also in several practical cases, for example for growth of PTCDI-C13 on smooth surfaces and for relatively weak molecule–substrate interactions. The factors behind 2D aggregation in PTCDI-C13 crystals were further investigated by modelling nanorod-like[208] systems with periodicity in one dimension. To this end, MD simulations were performed on quasi-1D supercells of the CF and ST structures, respectively, with periodicity along the [1 0 0] direction of the corresponding 2D crystal and a variable number of replica along the orthogonal in-plane non-periodic direction. The mean potential energy at 300 K of PTCDI-C13 CF and ST aggregates composed by 1 to 7 supercells along the non-periodic direction of the system is shown in Figure 4.5.

For a single stack of PTCDI-C13 molecules, the ST structure is energetically more stable, as a consequence of the reduced steric hindrance of the alkyl chains with respect to the CF phase. However, the stability of the CF structure increases with the size of the system along the [0 1 0] direction of the corresponding 2D crystal, as a consequence of the more favourable 2D packing of the perylene cores. The relative stability of CF and ST quasi-1D planar structures, as a function of their width along the [0 1 0] direction, can be related to the relative propensity to form aggregates in thermodynamically- and kinetically-controlled growth conditions. Namely, in kinetically-controlled growth of PTCDI-C13 the effect of terms associated to entropy, related mainly to the conformation of flexible alkyl chains, dominates the total free energy of the system. In these

conditions, aggregation of needle-like molecular stacks in the ST conformation, characterized by higher flexibility of alkyl chains and consequent lower steric hindrance, can be observed. Inversely, the thermodynamically-controlled growth of aggregates, induced by low initial molecular kinetic energy in the deposition process or by annealing/quenching cycles, is expected to lead to formation of extended 2D layers in the most stable CF form, as also suggested by the phase transition discussed above.

4.4 Electronic properties

To assess the energetics and the electronic properties of the PTCDI-C13 structures in more detail, DFT calculations were performed on 2D crystal systems starting from the structures obtained by MD simulations. In particular, DFT calculations were carried out using the CRYSTAL09 package[175, 176]. The exchange-correlation contributions to the total energy were treated using the hybrid B3LYP functional with 20% of exact Hartree–Fock exchange[209, 210]. The all-electron Gaussian-type basis sets adopted were 6-31(d1) for oxygen[211], nitrogen[212] and carbon[213], and 31(p1) for hydrogen[211]. Long-range dispersion interactions were accounted for by a post-DFT dispersive contribution, suggested by Grimme[214], to the computed ab-initio total energy and gradients. For each optimised structure, the charge transfer integrals in dimers, τ, were computed as:

$$\tau = \frac{J_{ij} - S_{ij}\frac{(e_{ii}+e_{jj})}{2}}{1 - S_{ij}^2} \tag{4.1}$$

where J_{ij}, S_{ij} and eii, ejj are the transfer integral, the overlap integral and the site energies, respectively:

$$\begin{aligned} J_{ij} &= \langle \varphi_i | h_{ks} | \varphi_j \rangle \quad S_{ij} = \langle \varphi_i | \varphi_j \rangle \\ e_{ii} &= \langle \varphi_i | h_{ks} | \varphi_i \rangle \quad e_{jj} = \langle \varphi_j | h_{ks} | \varphi_j \rangle \end{aligned} \tag{4.2}$$

with φ_i the frontier molecular orbital (i.e. HOMO or LUMO) of the i-th molecule and h_{ks} the Kohn–Sham Hamiltonian of the molecular dimer. For each crystal structure, the reported τ were computed as the average of values obtained for the two nonequivalent closest dimers in the 2D system. DFT variable-cell full geometry optimisations indicate the CF crystal as the most stable, with a total electronic energy of 244 and 301 meV per cell lower with respect to the ST and HB crystals, respectively (see Table 4.2). The DFT optimised lattice parameters for the PTCDI-C13 crystal structures considered, also shown in Table 4.2, are in good agreement with force-field results, with a slight increase of surface densities. On the basis of the DFT wavefunctions, charge transport properties of the PTCDI-C13 crystals were evaluated by computing transfer integrals τ. Despite the less dense packing, the CF structure exhibits a much larger electron transfer integral (τ_e) with respect to the ST and HB 2D crystals (see Table 4.3). This difference can be ascribed to the more favourable overlap of LUMO orbitals of PTCDI-C13 molecules stacked along the [1 0 0]

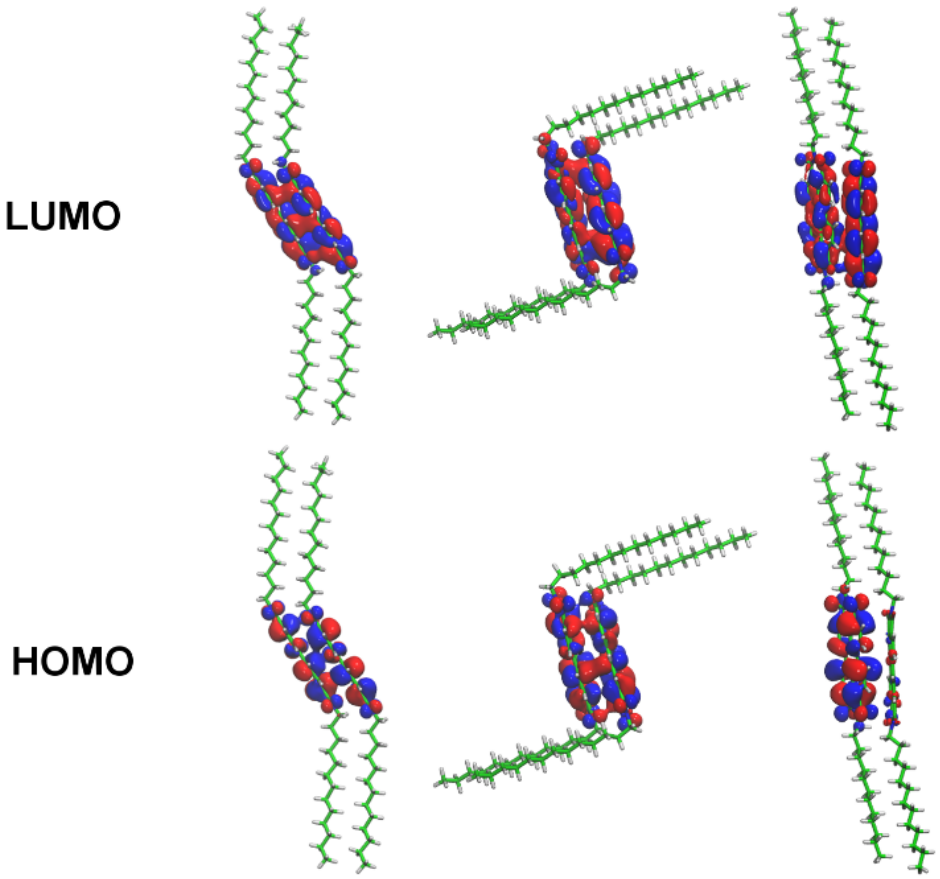

FIGURE 4.6: Topology of the LUMO (top) and HOMO (bottom) orbitals for PTCDI-C13 dimers in the configuration of the CF (left), ST (middle) and HB (right) DFT optimised crystal structures. Adapted from Ref. [35].

TABLE 4.2: Cell parameters for PTCDI-C13 crystals (a,b:Å; γ:degrees and surface densities (mol nm^{-2}) obtained by DFT calculations.

Structure	a	b	γ	Density
CF	8.62	8.57	82.74	2.73
ST	7.36	8.65	85.94	3.15
HB	7.11	8.91	74.50	3.28

TABLE 4.3: Relative energies (meV) and transfer integrals (meV) for holes and electrons computed at the DFT level.

Structure	ΔE	τ_h	τ_e
CF	0	92	235
ST	244	44	37
HB	301	2	46

direction in the CF crystal, as shown by the orbital topologies of Figure 4.6. Indeed, even small orbital misalignments are known to impact greatly on the transfer integrals in perylene diimide derivatives [214]. Inversely, the computed hole transfer integral (τ_h) for the CF structure is about three times lower than the τ_e and only two times larger than that of the ST crystal, confirming the low propensity to p-type transport in perylene diimide derivatives[24, 215], as also suggested by the negligible τ_h for the HB structure.

4.5 Conclusions

In summary, an integrated approach based on MD and DFT simulations was applied to investigate the relationship between crystal structure, stability, dynamics and charge transport properties in 2D PTCDI-C13 aggregates. MD simulations indicate a remarkable long-range stability for different putative 2D crystals. The thermodynamically most stable crystal structure corresponds to a face-to-face interaction between the π-cores of the perylene moieties, thus confirming experimental evidences. Moreover, a metastable 2D crystal phase of PTCDI-C13, with perylene cores arranged in a staggered configuration, was also observed. The relative stability of the two lowest-energy 2D phases, however, is reversed in quasi-1D nanorods, suggesting a likely role of side-to-side interactions in stabilizing 2D aggregates. The local ordering of aggregates was analysed in terms of radial and angular structural parameters. The latter, in particular, can be related to the relative orientation of the π-cores. Moreover, transfer integral calculations based on DFT suggested a strong correlation between molecular morphology and charge transport properties. Namely, the most stable 2D structure of PTCDI-C13 is found to be also the most effective for electron transport. Our results suggest a likely dependence of the molecular aggregation in nanostructures with environment, growth conditions and thermal treatments, affecting dramatically charge transport properties in devices. In particular, a controlled aggregation of PTCDI-C13 towards long-range-ordered 2D layers in the thermodynamically stable cofacial phase is expected to lead to most efficient in-plane charge transport.

Chapter 5

Morphology and electronic properties of three-dimensional PTCDI-C13 aggregates

The structural properties of bulk and bilayer ordered aggregates of PTCDI-C13 were investigated by performing molecular dynamics (MD) simulations. The relationship between morphology and charge transport was then evaluated by computing electron transfer integrals at the density functional theory (DFT) level. In particular, we relaxed putative structures of 3D aggregates of PTCDI-C13 by atomistic MD. Relaxed structures were used to carry out metadynamics calculations in the space of suitable collective variables, identifying global and local minima and computing the related free energy. The structures of the predicted stable and metastable configurations were also used to evaluate total energies and electron transfer integrals in 3D ordered aggregates at the DFT level. The effect on the charge transport properties of the disorder induced by interactions of the organic layer with substrates, as in the case of organic/dielectric interfaces, was further assessed by evaluating transfer integrals of aggregates of PTCDI-C13 in contact with a model surface. As observed previously (Chapter 4), the PTCDI-C13 molecule exhibits two low-energy packing configurations in planar two-dimensional (2D) aggregates, with the perylene cores arranged according to a symmetric cofacial (CF) or staggered (ST) configuration, respectively. Moreover, aggregates of molecules with a planar π-core and long tail substituents may exhibit various degrees of interdigitation of alkyl chains, which assists formation of regularly packed structures[78, 126, 216]. We therefore focused our simulations on bulk and bilayer aggregates of the CF 2D crystal of PTCDI-C13, which is the thermodynamically most stable structure at ambient conditions, considering both interdigitated and non-interdigitated configurations. Furthermore, calculations were also performed on the 3D aggregation of PTCDI-C13 in the ST configuration, which is likely to occur in kinetically-controlled growth conditions (Chapter 4). The integration between atomistic MD, metadynamics simulations, DFT total energy calculations, evaluation of electronic transfer integrals and the comparison with available experimental data, guides us in assessing the structure of PTCDI-C13 in nanoaggregates as a function of growing conditions, correlating molecular structure to potential performances in devices.

The work presented in this chapter has been published in Ref. [36].

5.1 Morphology of bulk phases

Simulation models were prepared basing on the configurations of the perylene diimide cores taken from equilibrated 2D (monolayer) CF and ST layer phases, as described in Chapter 4. Initially, the flexible C13 alkyl chains of PTCDI-C13 were arranged to form, in the direction orthogonal to that of π-stacking, a fully-interdigitated 3D bulk crystal. The degree of interdigitation was progressively decreased, by changing the cell parameter orthogonal to the π-stacking plane, relaxing again the system by variable-cell MD, obtaining the lay-on configuration. Both interdigitated and lay-on CF and ST phases were initially relaxed to the nearest energy minimum by steepest descent optimisation and subsequently equilibrated at 300 K, in the NPT ensemble, for 4 ns. Stable configurations were then cooled to negligible kinetic energies and optimised. Electrostatic interactions were evaluated by the particle-mesh Ewald (PME) method, using cut-off of 10.0 Å for both Coulomb and van der Waals interactions. The Nose-Hoover thermostat[185, 186] was used for simulations in the NVT ensemble, with a time constant of 1.0 ps, and the Parrinello-Rahman barostat[187] added in variable-cell (NPT) simulations, with a time constant of 10.0 ps. All the MD simulations were performed by using the GROMACS package[183]. Simulations converged to four stable configurations at room temperature, corresponding to a fully-interdigitated and a lay-on structure for both the CF and the ST crystals, shown in Figure 5.1, together with their equilibrated unit cells. To assess the relative stability of the relaxed structures, and to explore the underlying free energy landscape, further MD simulations were performed. Namely, the equilibrated 3D bulk structures were annealed at 500 K for 2 ns. No relevant structural changes were observed for the CF lay-on structures in the timescale of MD simulations. However, annealing of the relaxed ST lay-on and interdigitated structures at 400 K for 2 ns led to interconversion to the CF lay-on configuration. The interconversion mechanism from ST lay-on and interdigitated structures to the CF lay-on configuration suggests a larger stability for this latter, in complete analogy with the case of PTCDI-C13 monolayers.

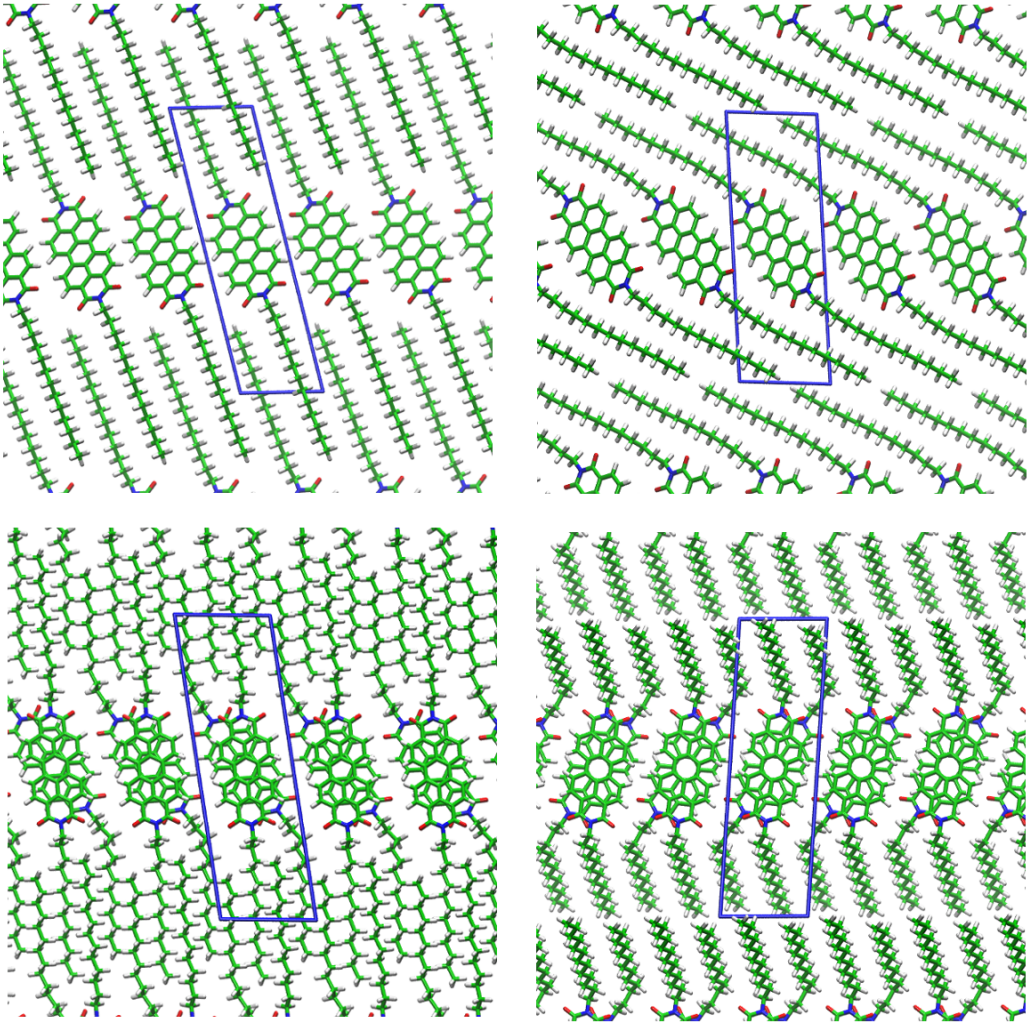

FIGURE 5.1: Relaxed structures for the bulk CF (top) and ST (bottom) crystals of PTCDI-C13 in the interdigitated (left) and lay-on (right) configurations. Adapted from Ref. [36].

5.2 Morphology of bilayer structures

The same equilibration protocol was performed on bilayers of the equilibrated bulk configurations. To model the bilayers, the bulk phases obtained previously were replicated along the z axis and 50 Å of vacuum were inserted along the z direction of the box. The MD equilibration resulted in configurations similar observed in the bulk phases, as shown in Figure 5.2. In bilayers, however, the topmost and bottommost alkyl chains of PTCDI-C13 lean towards the π-cores, in analogy to what is observed in monolayers. The tilted configuration of the C13 chains can thus be considered a structural feature of the topmost layers in ordered PTCDI-C13 aggregates, corresponding to the surfaces exposed to scanning-probe techniques, or at heterointerfaces. Notably, the computed inter-layer distance for the CF layon bulk configurations (25.2 Å) agrees remarkably well with the height of the PTCDI-C13 unit cell (25.3 Å) obtained by XRD experiments[5, 24, 25]. In addition, the slight increase of the inter-layer distance in bilayers (25.6 Å) is compatible with the larger d-spacing observed in thin-films (25.6 – 26.1 Å)[5, 24]. Unlike other substituted perylene derivatives, exhibiting interdigitated stable structures, the relatively short inter-layer distance in PTCDI-C13 thin-films, with respect to the end-to-end length of a relaxed isolated molecule (about 43 Å), can be related to the tilted configuration assumed by molecules on the xy plane.

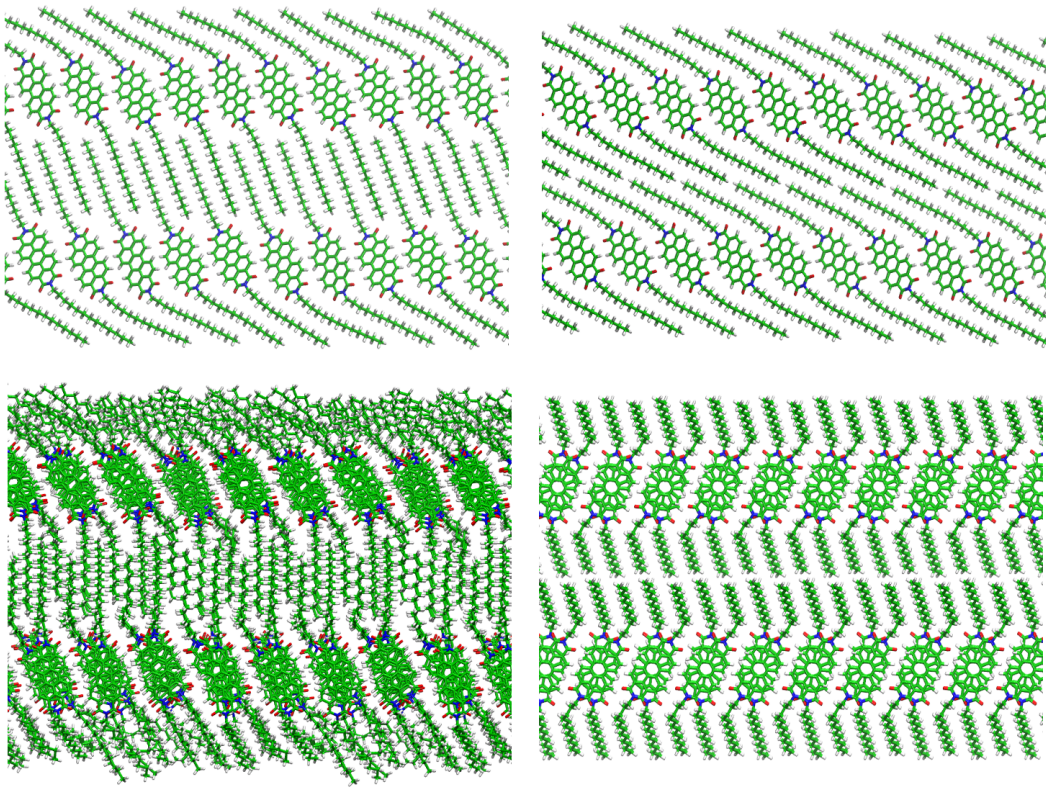

FIGURE 5.2: Relaxed structures for bilayers of PTCDI-C13 in the CF (top) and ST (bottom) configurations in the interdigitated (left) and layon (right) configurations. Adapted from Ref. [36].

5.3 Free energy calculations

Further assessments of the equilibrated structures of Figure 5.1 and quantitative estimates of the related Gibbs free energy surface were carried out by predictive structural simulations using metadynamics. These calculations were performed using the Plumed plugin[196] for LAMMPS package[184]. As collective variable for these calculations, the z component of the distance (d_z) between the terminal carbon atoms of contiguous alkyl chains was used (see Figure 5.3). Free energy calculations were performed by adding Gaussian functions to the metadynamics potentials with a frequency of 1000/step, a height of 10^{-3} kJ mol^{-1} and a width sigma of 0.10 kJ mol^{-1}. These calculations were only performed on the CF configuration, since it was found to be the most stable one, in order to evaluate the local minima of interdigitated and lay-on configurations, and also the energy barrier for the phase transition between them. The CF interdigitated bulk structure of PTCDI-C13, which, for the above considerations, is expected to constitute a local free energy minimum, was used as the starting configuration for metadynamics. Namely, in order to avoid undesired effects due to the supercell, metadynamics calculations were applied on a system composed of a single molecule. The defined collective variable accounts for structural changes from interdigitated to lay-on configurations. The resulting Gibbs free energy surface, as a function of the selected collective variable (see Figure 5.3), confirms the occurrence of two main basins of attraction, corresponding to the fully-interdigitated ($d_z = 1.15$ nm) and to the layon ($d_z = -0.13$ nm) CF configurations, respectively. The CF lay-on structure results more stable than the corresponding fully-interdigitated configuration, with a difference in free energy of about 20 kJ mol^{-1} at 300 K and a barrier for interconversion that is estimated to be about 45 kJ mol^{-1}. The main contribution to the observed free energy difference can be ascribed to the coulombic repulsion between alkyl C13 chains, which is significantly larger in the interdigitated configuration. Therefore, from our observations, alkyl chains assist interlayer ordered packing, despite a low propensity to interdigitation. Remarkably, the broader free energy basin corresponding to the interdigitated configuration lies closely to a local minimum, located at $d_z = 0.83$ nm. This minimum corresponds to the partial slipping of interdigitated PTCDI-C13 molecules from each other, sterically controlled by the hindrance of -CH_2- and -CH_3 groups. The transition state connecting the interdigitated and layon structures is located at an intermediate value ($d_z = 0.37$ nm) on the computed free energy surface, with a structure corresponding to an incompletely-interdigitated configuration.

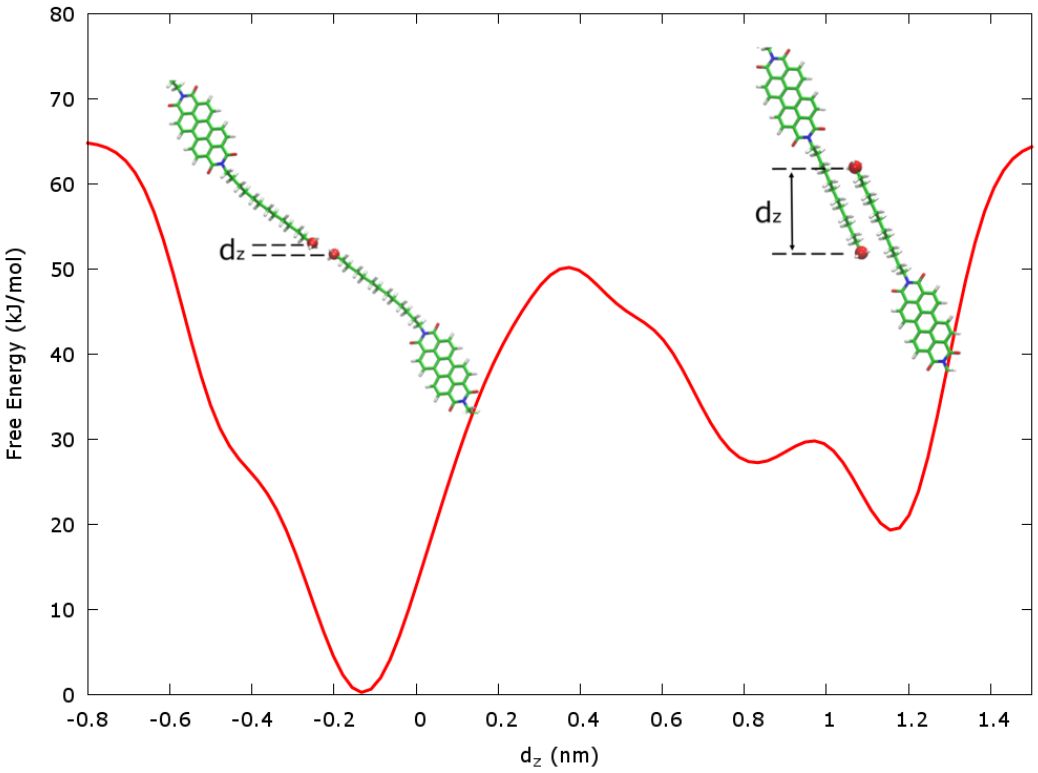

FIGURE 5.3: Gibbs free energy, in kJ mol^{-1}, for bulk PTCDI-C13 at 300 K in the space of the collective variable representing the z-component of the distance between the terminal carbon atoms of contiguous alkyl chains. Adapted from Ref. [36].

5.4 Electronic properties

More detailed information about the structure and energetics of PTCDI-C13 crystals were obtained by DFT calculations. Periodic DFT calculations on bulk model systems were carried out with the SIESTA package[174] (version 4.0), by applying the PBE[209] gradient-corrected approximation to DFT, using a basis set of double-ζ plus polarization quality for orbital expansion and a cut-off of 150 Ry for density expansion. Van der Waals interactions were accounted for by including a Grimme[214] dispersion potential. A reciprocal space mesh of 3x3x1 k-points was used in periodic calculations. Geometries were optimised by relaxing all the nuclear degrees of freedom until convergence to a maximum force of 0.02 eV/Å on atoms and 1 GPa on cell stress. The structural parameters for the configurations in Figure 5.1, optimised at the DFT level and corresponding total DFT electronic energies are reported in Table 5.4. Calculations indicate the CF lay-on configuration as the most stable, with the ST lay-on configuration lying about 44 kJ mol^{-1} above in energy. Moreover, interdigitated crystals are generally less stable than the corresponding layon structures by more than 65 kJ mol^{-1}. Therefore, it can be concluded that the CF lay-on configuration corresponds to the global energy minimum configuration for PTCDI-C13 crystals. This picture is confirmed by the excellent agreement between the DFT computed interlayer distance, corresponding to the c value of the cell paramater (25.9 Å) and the value observed by XRD and AFM experiments (between 25.6 and 26.1 Å) in PTCDI-C13 aggregates[5, 24]. Other computed CF lay-on lattice parameters are in agreement with experiments[25]. To shed light on the relationship between morphology and charge transport properties of PTCDI-C13, the intermolecular transfer integrals were computed on nearest neighbor dimers extracted from DFT-optimised structures and from equilibrated MD configurations. Transfer integrals were evaluated on dimers extracted from the DFT periodic calculations described above using the charge transfer integrals module of the ADF program package[177]. Electronic couplings for electrons and holes were computed by the PW91[217] exchange-correlation functional and a triple-ζ plus-polarization basis set. The resulting transfer integrals are reported in Table 5.2. The proposed multiscale approach is able to guide us to a better understanding of the structure/properties relationship in molecular aggregates of organic materials. In particular, starting from the molecular modelling of 3D bulk and layered phases, we are able to correlate morphology to charge transport through electronic structure calculations. This, in turn, allows us to speculate on the electronic behaviour of materials in thin-film devices. In the case of crystalline aggregates of PTCDI-C13, the computed values of transfer integrals were found in line with previous calculations on substituted PTCDI systems[89, 110]. Despite the relatively large transfer integrals, the poor hole conducting properties of PTCDI derivatives are usually ascribed to the deep ionization potential[125]. As expected, computed transfer integrals suggest significant charge transport in the direction of the π-stacking (values shown in Table 5.2) for crystalline aggregates. The CF structures exhibits comparable transfer integrals for electrons in the lay-on and interdigitated configurations. Although less stable, the interdigitated structures were found to shows higher

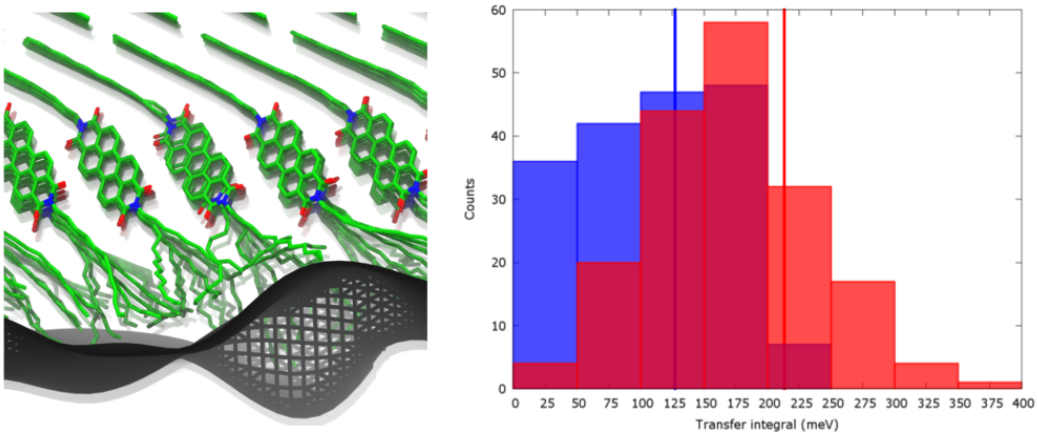

FIGURE 5.4: Snapshot of an equilibrated PTCDI-C13 bilayer in the CF layon configuration at the interface with a model surface (left) and the distribution of transfer integrals for electrons (blue) and holes (red) for the first PTCDI-C13 layer equilibrated at room temperature at the interface with the model surface (right). Vertical lines indicate the value of transfer integrals of DFT crystal structures for electrons (blue) and holes (red). Adapted from Ref. [36].

values of transfer integrals with respect to the lay-on ones. Transfer integrals for the ST structures are generally lower than for the CF configurations, as a result of the tilted π-stacking, similarly to the case of monolayers (Chapter 4). Besides crystalline ideal structures, the effect of more realistic environments on charge transport properties was assessed by computing the distribution of transfer integrals for a bilayer of the most stable PTCDI-C13 phase (CF lay-on) equilibrated at room temperature and at the interface with a model surface with a morphology resembling that of a typical substrate for the growth of organic thin-films. The periodic model surface was first generated by constructing a 5x5 nm regular square-lattice of dummy atoms with 0.1 nm spacing, and assigning a random value, within selected boundaries, for the z (i.e., orthogonal to the molecular plane) component of the coordinates. The z component was then changed iteratively by averaging the first derivative of neighboring sites, until convergence to a given total surface root mean square (rms) roughness. This algorithm allows to obtain a model surface with selected rms and higher-order moment surface parameters (skewness and kurtosis) depending on the initial random distribution of z coordinates. In agreement with the value commonly observed on the surface of polymer or inorganic dielectric materials for in-plane devices[7, 63, 218], a model surface with a rms roughness of 0.3 nm was generated, with relatively large skewness and kurtosis values (0.098 and -0.414, respectively) to enhance the effects of local molecule/surface interactions. All atoms of the model surface were assigned non-bonded parameters of graphite carbon atoms, to mimic the effect of hydrophobic substrate/molecule weak forces, and were kept frozen throughout all simulations. A supercell of the multi-layer crystalline PTCDI-C13 aggregate, with lateral dimension of about

TABLE 5.1: Lattice parameters of PTCDI-C13 crystals (a,b,c: Å; α,β,γ:degrees), computed at the DFT level, and total electronic relative energies (kJ mol^{-1}).

		a	b	c	α	β	γ	Energy
Lay-on	CF	4.300	8.470	25.875	95.91	102.39	95.76	0
	ST	3.604	8.672	30.272	84.66	91.19	94.45	+44.1
Interdigitated	CF	4.230	8.461	28.658	103.34	89.83	98.21	+86.8
	ST	3.290	9.868	31.762	98.59	91.50	81.90	+111.2

5x5 nm, was first relaxed in vacuum, then put in close contact with the model surface, and subsequently equilibrated at room temperature by MD for 10 ns. This simulation time was found to be sufficient for the formation of a stable interface between the PTCDI-C13 aggregate and the model surface. Transfer integrals were computed on the equilibrated system for all molecule pairs. The effect of annealing on the morphology of PTCDI-C13 aggregates on a model surface was further evaluated by analyzing relevant structural parameters upon annealing at 400 K followed by relaxation for 5 ns. As expected, thermal disorder broadens the distribution of transfer integrals for both electrons and holes[122], also slightly lowering the average value by about 22 and 6 meV for electrons and holes, respectively. The distribution of transfer integrals for holes is further broadened and shifted to lower values for an ordered bilayer of PTCDI-C13 aggregates relaxed on surfaces (See Figure 5.4).

However, electron transfer integrals are essentially unchanged with respect to the crystal for the first layer of the PTCDI-C13 in contact with the surface, whereas lower values are observed for the second layer. Indeed, in the first PTCDI-C13 layer ordered packing is maintained by the interplay between strong π-stacking interactions and flexibility of alkyl chains, which induce a bulk-like interlayer interaction and adapt to the morphology of the underlying surface. Moreover, in the particular case of interaction with a model surface, the morphology of PTCDI-C13 aggregates is slightly affected by annealing at 400 K, as suggested by computed structural parameters. Despite the slight lowering of intermolecular transfer integrals related to thermal and structural disorder, computed values suggest remarkable charge transport properties for multi-layer aggregates of PTCDI-C13 in realistic environments. In particular, transport of electrons exhibits a lower propensity to degradation upon structural modifications with respect to holes.

TABLE 5.2: Intermolecular transfer integrals in meV for electrons (coupling of LUMO orbitals) and holes (coupling of HOMO orbitals) for dimers extracted from the DFT-optimised PTCDI-C13 crystal structures (a), average values for dimers of the PTCDI-C13 MD crystal structure at 300 K (b), first layer (c) and second layer (d) at the interface with a model surface.

		τ_e	τ_h
Lay-on	CF	127[a]	213[a]
		105[b]	207[b]
		109[c]	170[c]
		86[d]	180[d]
	ST	38[a]	112[a]
Interdigitated	CF	146[a]	328[a]
	ST	82[a]	18[a]

5.5 Conclusions

In summary, an integrated computational approach, based on MD and DFT calculations, allowed to understand the details of the morphology in PTCDI-C13 aggregates, to evaluate the related stability and energetics and to correlate structure to charge transport properties. The most stable ordered bulk crystal structure found corresponds to a CF lay-on configuration. Computed crystal parameters are in excellent agreement with available structural data. The CF lay-on configuration is also prevalent in bilayers of PTCDI-C13, mimicking the situation occurring in thin-films or at interfaces. Our calculations also indicate local energy minima for interdigitated (CF and ST) and for asymmetric ST structures, where the π-cores of perylene diimide arrange in pairs of rotated units. These configurations, however, are more than 40 kJ mol^{-1} higher than the global energy minimum. Indeed, metadynamics calculations and simulation of heat treatments suggest a likely interconversion path from local minima configurations to the thermodynamically stable CF lay-on structure. In particular, the formation of interdigitated aggregates of PTCDI-C13 is found to be unfavored with respect to lay-on structures, with C13 alkyl chains assisting intra-layer aggregation. Nevertheless, the possible occurrence of different structures in nanoscale aggregates of PTCDI-C13 confirms experimental evidence, where an interplay between layered and three dimensional growth is observed, as a function of processing conditions. Moreover, the thermodynamically stable CF lay-on configuration exhibits remarkable charge transport properties, as suggested by intermolecular charge transfer integral calculations. A broadening of the distribution of transfer integral values for electrons and holes and a lowering of the average is observed for PTCDI-C13 layers equilibrated at room temperature and at the interface with a model substrate. However, computed values suggest remarkable charge transport properties for the CF lay-on

configuration also in partially disordered morphologies, suggesting this configuration as responsible of the observed high conductivities in layered aggregates of PTCDI-C13.

Chapter 6

Coarse-grain model of PTCDI-C13

In Chapters 4 and 5, the morphology of PTCDI-C13 2D and 3D phases were simulated. Detailed information about the polymorphism and the thin-film aggregation of the organic semiconductor were obtained, together with the charge transport properties of the different phases, applying MD and DFT methods. This was a first step towards the study of the thin-film aggregation of the PTCDI-C13 at the interfaces in devices. The large-scale morphology of these interfaces can be investigated by applying MD simulation techniques, enabling the study of phenomena occurring at the nanoscale with atomistic precision (see Chapter 7).

However, atomistic models limit the size of the systems studied and the time scale of the simulations, usually shorter than relevant processes occurring in materials at the nanoscale (see Section 3.4). The computational cost required to simulate systems with sizes comparable to the real devices would be too demanding even for HPC infrastructures. For this reason, the simulation of large-scale morphologies of materials and interfaces used in organic electronics, can be performed by developing CG models, allowing the investigation of systems with increased size and time scales. This approach has been applied to the case of PTCDI-C13 aggregates in thin-films.

In this chapter, the development of a preliminary coarse-grain model of the PTCDI-C13 molecule is presented. The first step is to develop a CG model of the PTCDI-C13 which resembles the atomistic properties of the material, decreasing its complexity. The atomistic information obtained by the MD simulations of PTCDI-C13 2D and 3D phases (Chapters 4 and 5) was used to generate a coarse-grain potential able to lower the complexity of the system by maintaining the molecular properties, by performing a proper fitting procedure. The first step consists in the choice of the beads, which are not commonly used spheres, but rather ellipsoids with unconventional interaction potentials (Section 6.1.1). The electrostatics of the coarse-grain model will be considered by fitting the atomistic charges on the beads (Section 6.1.2). Finally, the interaction of each bead with the others will be parametrized by proper fittings of the atomistic potential for non-bonded and bonded interactions, including the bonds, angles and dihedral components (Section 6.1.3). The coarse-grained model obtained was then validated by performing simulations of bulk structures, comparing the results obtained with the atomistic models of Chapters 4 and 5.

The simulations presented in this chapter were performed by using LAMMPS package [184].

6.1 Coarse-graininig procedure

6.1.1 Choice of the beads

The PTCDI-C13 molecule has been represented with Gay-Berne (GB) beads [219]. Namely, one larger ellipsoid represented the rigid perylene diimide core, smaller ones represented the C_3H_6 groups constituting the alkyl chains, while the -CH_3 terminal groups were described with a sphere. The coarse-grained model obtained is shown in Figure 6.1. As can be seen from the figure, this model allows to represent the PTCDI-C13 with 11 beads for each molecule, instead of 118 atoms of the atomistic PTCDI-C13, hence substantially decreasing the complexity of the system and related computational costs.

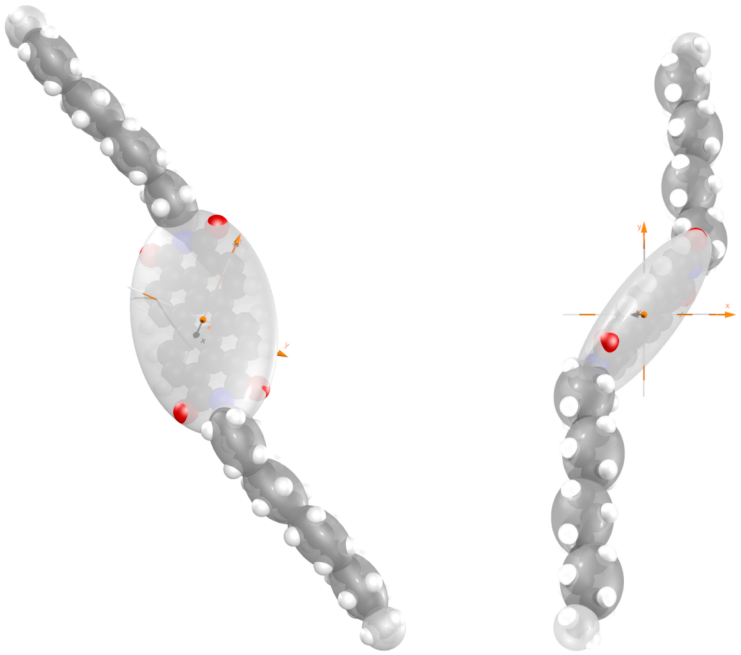

FIGURE 6.1: Coarse-grain model of the PTCDI-C13 molecule. One ellipsoid for the core, one ellipsoid for the C_3H_6 groups of the alkyl chains and one sphere for the CH_3.

6.1.2 Effective charges

A set of effective charges has also been fitted on the atomistic potential, using a genetic algorithm described in Ref. [139]. With the chosen set of effective charges, a coarse-grained fitted electrostatic potential was obtained (Figure 6.2b) starting from the atomistic electrostatic potential (represented in Figure 6.2a). The effective positive (red) and negative (blue) charges were then placed within the ellipsoid representing the perylene core, as shown in Figure 6.2c. This off-center electrostatic potential has been implemented in LAMMPS[184, 220].

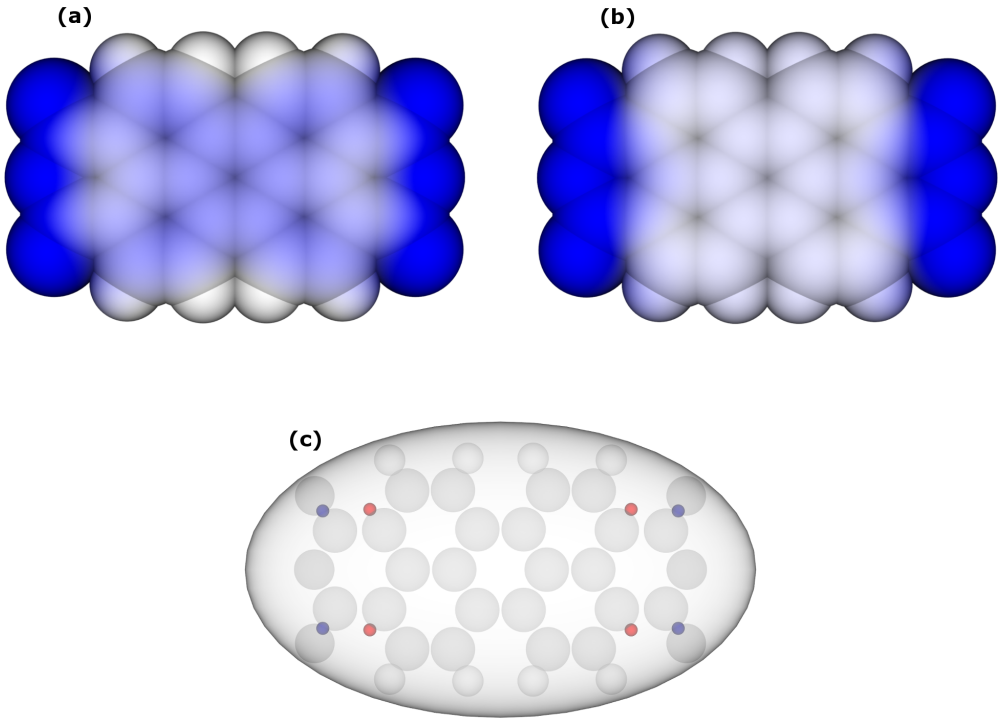

FIGURE 6.2: Atomistic (a) and fitted (b) electrostatic potentials are represented as charge density on the perylene diimide core. The positions of the effective positive and negative coarse-grained charges are depicted in red and blue, respectively (c).

6.1.3 Flexible force field

In order to maintain the atomistic information of PTCDI-13 molecule, the beads modeled were constrained to act as chemically bonded with a set of bonded potential terms, including effective bonds, angles and dihedrals[219]. In particular, the parametrization of this bonded potential was carried out by performing an MD simulation of 1 ns at 500 K in the NVT ensemble of a single molecule of PTCDI-C13 in vacuum. This allowed the bonds, angles and dihedrals to explore all the possible conformations within the atomistic force field. Bonds, angles and diedrals parameters were extracted from the MD trajectory and the data obtained were parametrized to effective potentials with the application of an Inverse Boltzmann procedure, as described in section 3.4, following the equation:

$$U_{eff}(x) = -k_B T \ln[p(x)] \tag{6.1}$$

allowing the probability to be converted into energy profiles. An example of this conversion is represented in Figure 6.3.

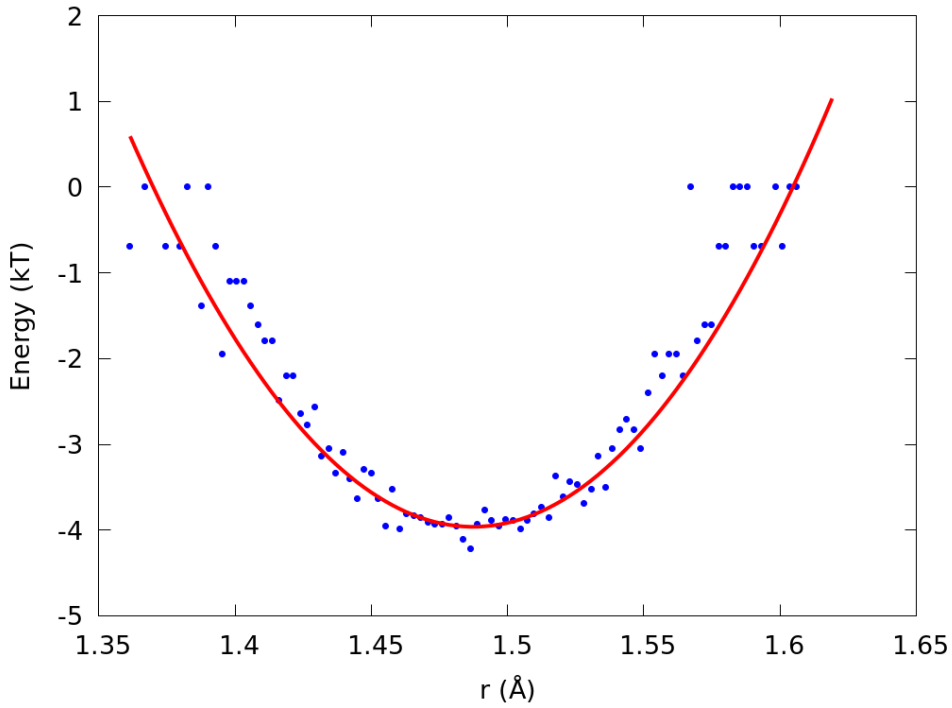

FIGURE 6.3: Parametrization of the bond between the perylene core and the first C_3H_6 of the alkyl chains. Blue dots are the probability extracted via the Boltzmann inversion, the red curve is the fitted data.

6.2 Coarse-grained simulations

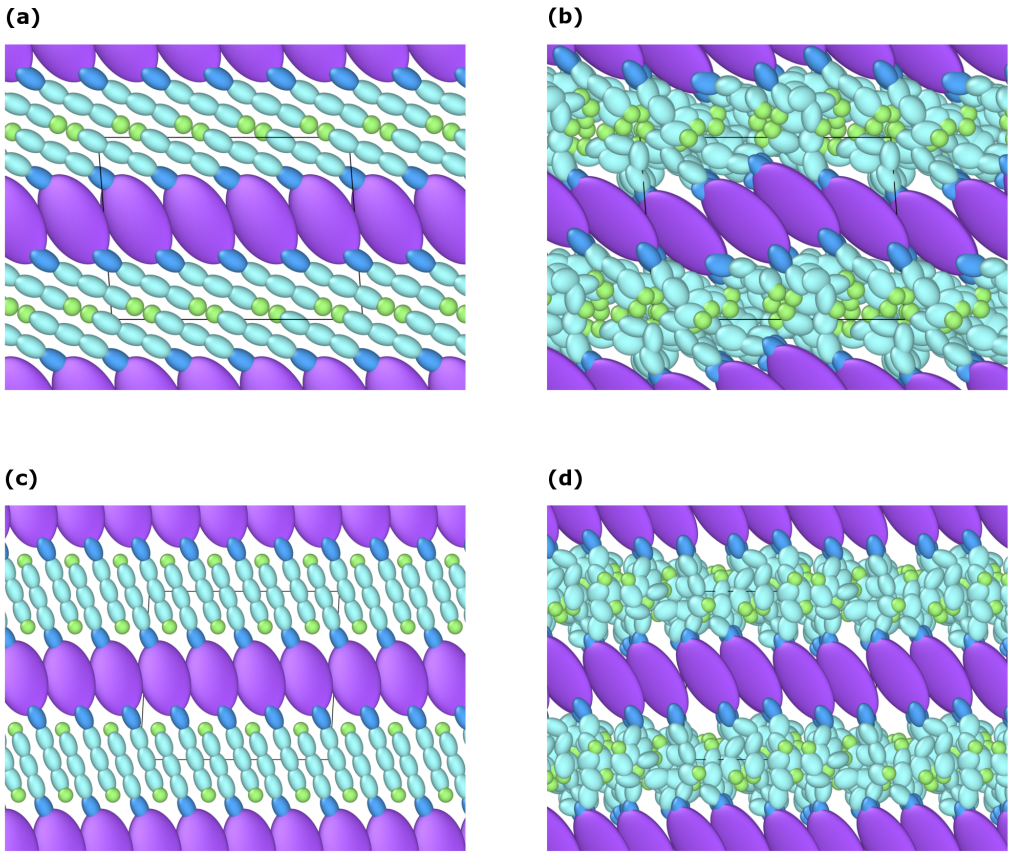

FIGURE 6.4: Coarse-grained simulations of bulk CF PTCDI-C13 structures. Starting ((a) layon (c) interdigitated) and final ((b) layon (d) interdigitated) configurations are represented.

To correlate the CG model developed, the 3D equilibrated bulk structures of PTCDI-C13 (obtained in Chapter 5) were used as a starting point for the coarse-grained simulations. In particular, simulations of the coarse-grained 3D PTCDI-C13 bulk were run at room temperature in the NVT ensemble for 1 ns with a timestep of 0.2 fs. The starting and final structures of the PTCDI-C13 structures are represented in Figures 6.4 and 6.5. All the bulk structures maintained their layon or interdigitated characteristic, apart from the ST interdigitated, which appeared to be the most disordered (Figure 6.5d). The aggregation of the CF and ST layon bulk after equilibration is structurally similar to the atomistic counterparts. To evaluate the correlation between the coarse-grained and the atomistic model, radial distribution function were computed between central bead (the one representing the perylene core) and compared with the atomistic, computed between PTCDI-C13 centers of mass. Even if the simulations were very short and still need further equilibration, results are promising and in good agreement with the atomistic data (Figure 6.6).

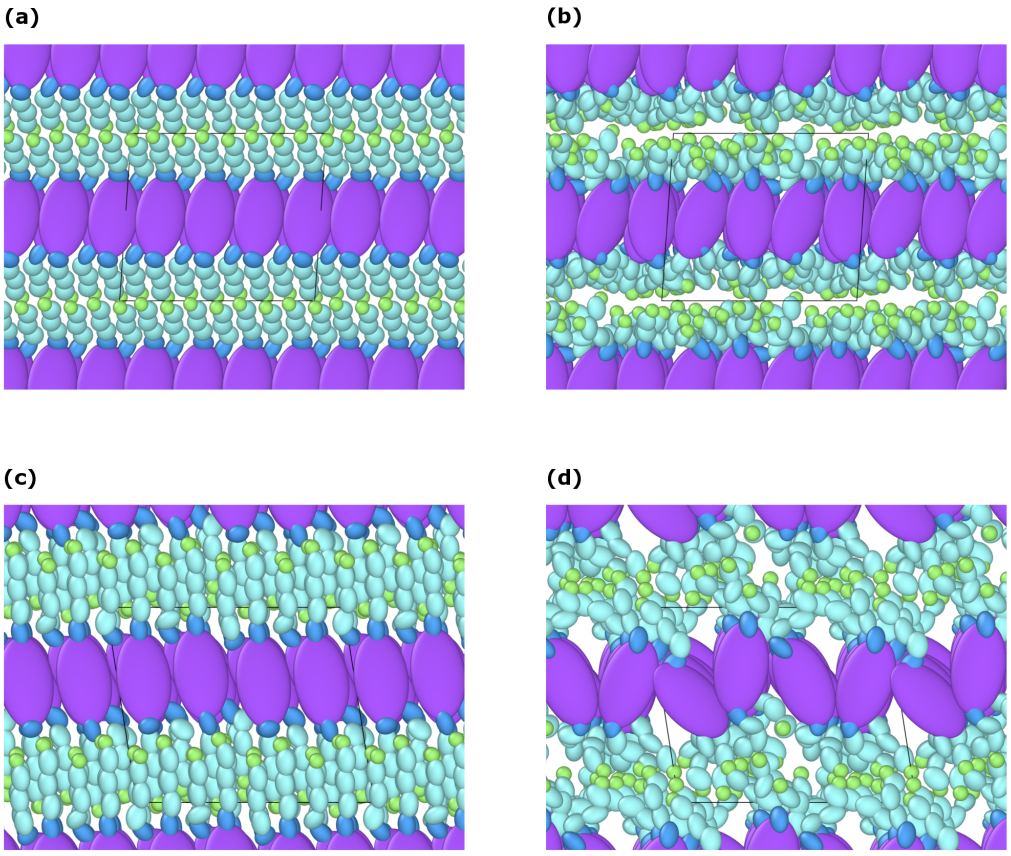

FIGURE 6.5: Coarse-grained simulations of bulk ST PTCDI-C13 structures. Starting ((a) layon (c) interdigitated) and final ((b) layon (d) interdigitated) configurations are represented.

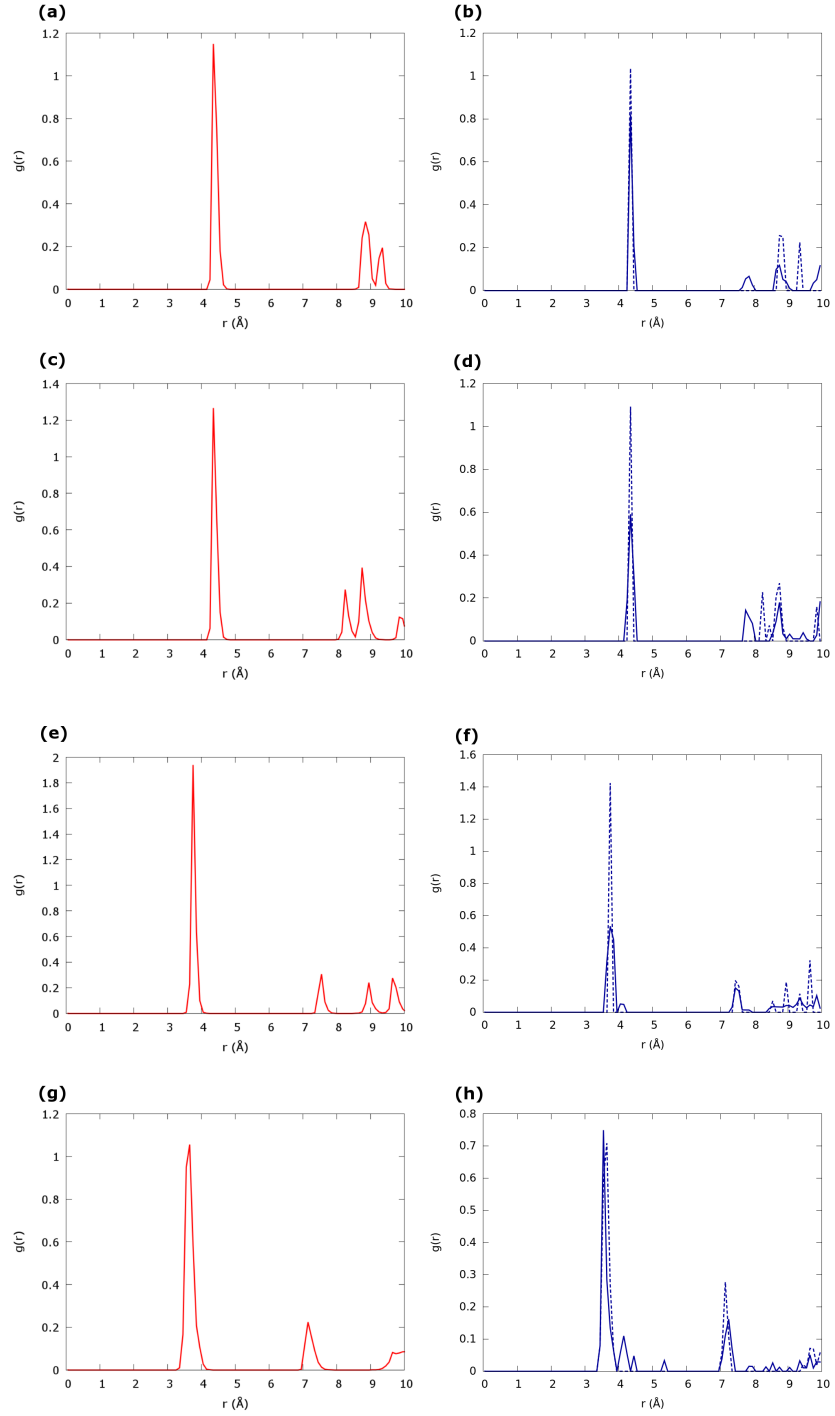

FIGURE 6.6: Radial distribution functions of atomistic (a:CF layon; c:CF interdigitated; e:ST layon; g:ST interdigitated) MD equilibrated structures and coarse-grained (b:CF layon; d:CF interdigitated; f:ST layon; h:ST interdigitated) initial (blue dashed) and final (blue solid) structures.

6.3 Conclusions

In this chapter, a preliminary coarse-grain model of PTCDI-C13 has been presented, including the choice of the beads for representing the atomistic structure and the consequent fitting of the atomistic charges and potential. In particular, the choice of modelling ellipsoid beads instead of conventional spheres allowed the correct description of the perylene core and its interactions. The CG model developed was then validated by performing a first set of simulations on the 3D bulk structures of PTCDI-C13, comparing the results with the atomistic simulations. The results obtained have demonstrated the feasibility of reducing the complexity of the atomistic model by developing a CG model, encouraging us to further develop the coarse-grain parameters in order to obtain a quantitative description of the structural properties of PTCDI-C13. Once the atomistic properties and interactions will be correctly represented by the the CG model, the simulation of large-scale aggregation of PTCDI-C13 will be possible, allowing to increase the size and time scale of the system under investigation. The procedure presented in this chapter can be potentially applied to other organic materials, starting from the atomistic information obtained by MD simulations and developing a coarse-grain model consistent with the atomistic properties.

Chapter 7

Interface morphology of PTCDI-C13 nanoscale aggregates

In organic electronic and optoelectronic devices based on thin films, one of the most important factors influencing the charge transport properties of active layers and hence the overall performance of devices, is the polycrystalline aggregation of organic semiconducting materials at the interfaces[9, 11, 20, 29]. The aggregation at the interface can be affected by several factors, like the deposition rate and the substrate temperature during the growth of the thin film, the application of thermal treatments on the active layer, the fabrication conditions, the degradation of the organic materials, and so on[5, 6, 24, 25, 63]. A detailed knowledge on the process occurring at the molecular level of the interfaces constituting the organic devices is crucial for a better understanding on the morphological properties of the organic materials, which can lead to the engineering of the materials and fabrication processing to build devices, and, in turn, to enhanced performance.

In this respect, computational tools can be useful for investigating the atomistic process occurring at the interfaces[127, 135, 136, 221, 222], based on the atomistic knowledge of the structural and electronic properties of the organic materials studied.

In this chapter, the interface morphology between PTCDI-C13 and other materials commonly used in organic devices, namely PMMA and graphene, was investigated by performing MD simulations using the GROMACS package[183]. In particular, the morphological properties of PTCDI-C13 at the interface with PMMA and graphene were investigated, mimicking the experimental processing, based on the information on structural and electronic properties in 2D and 3D aggregates obtained in Chapters 4 and 5. The results obtained by these simulations were also correlated with experimental available data.

The simulations presented in this chapter were performed at HPC facilities Cyfronet (Poland) and CINECA (Italy) through a PRACE-DECI and an ISCRA project, respectively.

7.1 PTCDI-C13 at the interface with PMMA

In OFETs, charge transport depends strongly on the morphology of the interface between the organic semiconductor and the insulator layer. The first few layers of semiconductor are the ones responsible for the charge transport in OFETs[9, 11, 20]. In particular, the layer at the interface with the dielectric plays a crucial role in the determination of the active layer morphology and hence to the performance of the final device. In this regard, a good control of the molecular structure and morphology of the organic semiconductor at the semiconductor/insulator interface is thus critical for enhancing the performance of OFETs[6, 10]. Detailed atomistic information, obtained by using computational tools, can assist the investigations on the nanoscale phenomena occurring at the interface related to the growth of organic materials on the insulator surface. This information, in turn, can be used to correlate simulated morphology with experimental characterizations. In this work, a computational study on the interface between an organic semiconductor and the dielectric layer at the atomistic scale was carried out, performing simulations based on molecular dynamics. Namely, PTCDI-C13 and PMMA were modeled as organic semiconductor and organic dielectric material, respectively. In order to understand how the growth of a second layer would affect the morphology of the first one, bilayers of PTCDI-C13 were equilibrated on the same surface of PMMA and the morphological properties were compared with the previous case. To investigate the kinetic growth of PTCDI-C13 on the PMMA surface, the growth of single PTCDI-C13 molecules on PMMA, mimicking the vapor deposition technique, was performed. Furthermore, simulations of islands formation and dynamics on both PMMA and PTCDI-C13/PMMA were performed, observing grain boundaries and coalescence of islands.

7.2 PTCDI-C13 monolayer on PMMA

The morphology at the interface between a monolayer of PTCDI-C13 and PMMA was firstly investigated by performing MD simulations. In particular, an equilibrated monolayer of PTCDI-C13 was relaxed on top of a 10x10 nm layer of PMMA, modeled in a previous work[126]. The molecules constituting the PTCDI-C13 monolayer was in the CF configuration, i.e. the most stable 2D phase of this material (see Chapter 4). The PTCDI-C13 monolayer was inserted in the simulation box at a distance of 10 Å from the PMMA surface. The system was then equilibrated for 5 ns at 300 K in a NPT ensemble. Furthermore, to study the effects of temperature on the morphology of PTCDI-C13 at the interface with PMMA, the PTCDI-C13 monolayer was annealed for 5 ns at 400 K, maintaining the PMMA slab at 300 K, mimicking the annealing applied experimentally to improve the molecular packing of PTCDI-C13[25]. The morphology of the interface was then investigated by evaluating structural parameters of the PTCDI-C13 monolayer. Namely, the distance between centers of mass (COM) in the monolayer, the average tilt angle of PTCDI-C13 molecules, the radial pair distribution function (g(r)), the density molecular profile along the z direction and the angular structural parameters (θ and φ) described in Chapter 4 were calculated. The morphology of the PTCDI-C13/PMMA interface after the 300 K equilibration is represented in Figure 7.1a. The PTCDI-C13 monolayer adapted on the surface of PMMA, with a partially ordered aggregation, and disordered configuration of akyl chains, but maintaining an overall packing through a strong π-π stacking. The flexibility of the alkyl chains, by modulating their length in order to improve the alignment of perylene cores along the monolayer, assist the aggregation of PTCDI-C13 at the interface with PMMA. By applying an annealing to the PTCDI-C13 monolayer at 400 K for 5 ns, the molecular packing of the monolayer at the interface improved remarkably, as shown in Figure 7.1b. The alkyl chains lined up in a very ordered fashion, with the perylene cores assuming an almost perfect CF configuration.

The aggregation at different temperatures was then compared by calculating the density profile of the system along the z direction, the g(r) between PTCDI-C13 molecules and the angular structural parameters. The results are reported in Figure 7.2. The density profiles (Figure 7.2a) shows, between 4

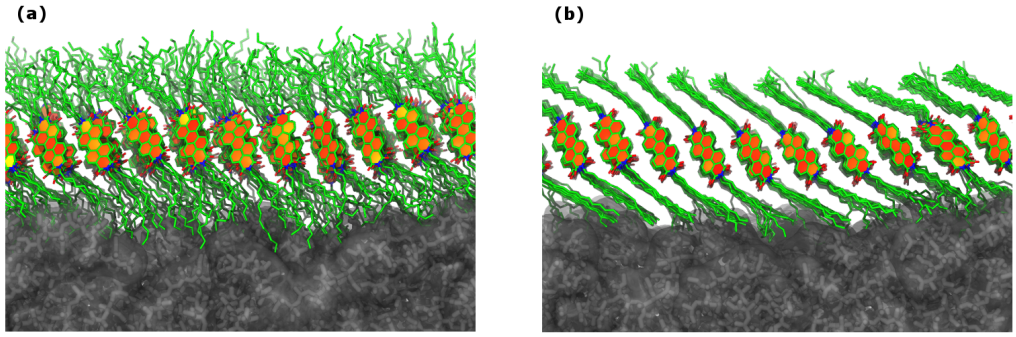

FIGURE 7.1: Monolayer of PTCDI-C13 equilibrated on PMMA slab at 300 K (a) and at 400 K (b).

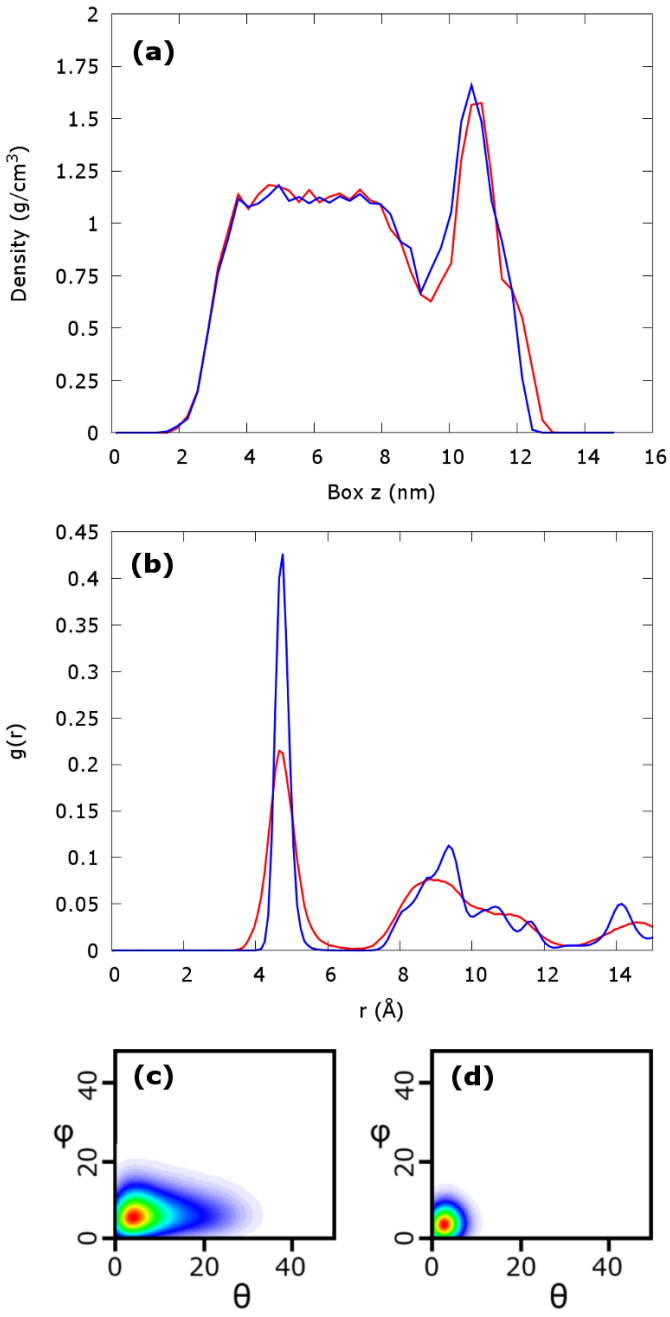

FIGURE 7.2: Density profiles (a) and g(r) (b) calculated for the PTCDI-C13 monolayer equilibrated on PMMA at 300 K (red) and at 400 K (blue). Angular structural parameters for the PTCDI-C13 monolayer equilibrated on PMMA at 300 K (c) and at 400 K (d).

and 9 nm, the PMMA slab (density ≈ 1.20 g/cm^3[97, 151]), and between 10 and 12 nm the PTCDI-C13 monolayer. The density profile of the monolayer at 400 K appeared less broaden and slightly shifted towards the PMMA surface. The g(r) is considerably different, with the main peak (related to the distance between COMs) of the annealed monolayer a lot sharper and more intense than the main peak at 300 K. The secondary peaks (representing the long-range ordering) are also quite different. The annealed monolayer presented sharp, well defined secondary peaks, whereas the one equilibrated at 300 K showed broaden undefined secondary peaks. Angular structural parameters at 300 K(see Figure 7.2c) show an interplay between the CF and ST configurations, with a general CF aggregation. This partial transition of some molecules from the CF to the ST configuration can be ascribed to the increased disorder due to the interaction with the polymeric rough surface. The more disordered aggregation of the PTCDI-C13 monolayer on PMMA surface is confirmed by the higher average distance between COMs of 4.80 Å respect to the 4.57 Å of the ideal 2D case. The average tilt angle calculated between PTCDI-C13 cores and z axis is 39.74°. The angular structural parameters calculated at 400 K (Figure 7.2d), instead, shows a complete presence of CF configuration in the monolayer. The average tilt angle increase, becoming 43.6°, probably due to the more space between the aligned chains and hence the need to tilt for maximize the contacts. These comparisons confirm the increased order in the aggregation of PTCDI-C13 monolayer at the interface with PMMA upon application of annealing at high temperature, as observed in experimental studies on this material[7, 24, 25].

7.3 PTCDI-C13 bilayer on PMMA

The organic semiconductor layer at the interface with the dielectric layer is the main responsible for the performance of the OFET devices. As described in the previous section, indeed, the morphology of this layer is one of the main features affecting the charge transport properties in organic devices. The interaction with the substrate and the temperature are the first factors influencing the morphology of the interface. However, the morphology of the first layer can be affected also by the subsequent layers of organic materials. In this section, the effects on the nanoscale 3D morphology of the PTCDI-C13 on the PMMA surface were investigated. In particular, PTCDI-C13 bilayers in the CF layon and interdigitated configurations were considered (as the 3D most stable structures observed in Chapter 5). The bilayers were firstly equilibrated in vacuum and then inserted in the simulation box at a distance of 10 Å from PMMA, as described before. Then, a simulation of 5 ns at 300 K was carried out. Furthermore, after the equilibration at 300 K, the effects of temperature were analysed by annealing the system at 400 K for 5 ns. All these simulations were carried out in the NPT ensemble (where the cell parameters a,b and γ were allowed to relax) in order to let the box parameters to adapt to the modification of the layer morphology upon the interaction with the rough surface. The final morphologies at different temperatures were then analysed by evaluating the same structural parameters as before. The structure of the layon PTCDI-C13 bilayer

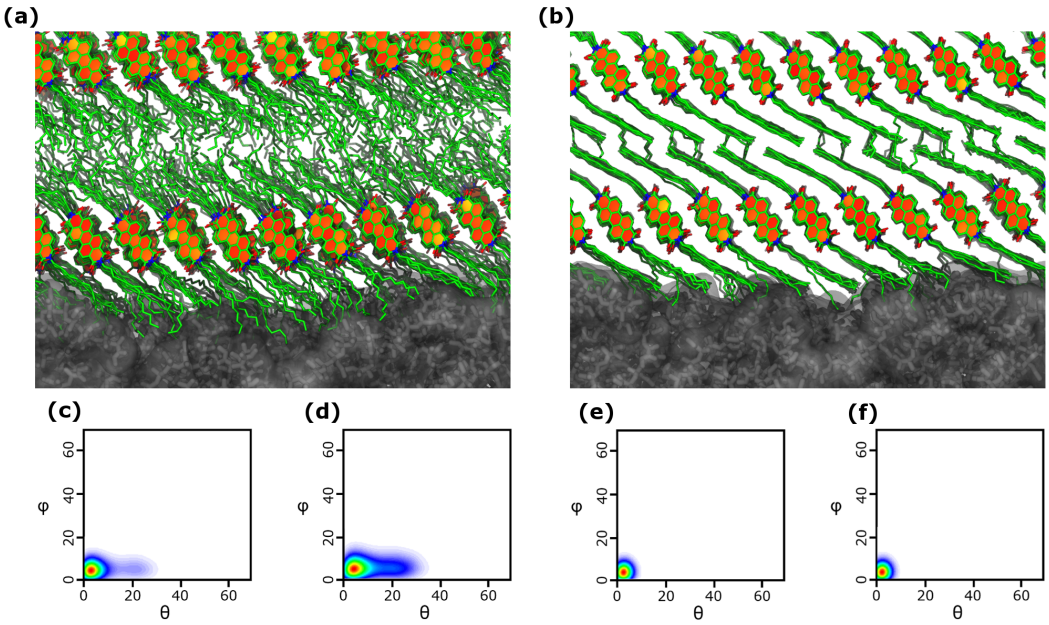

FIGURE 7.3: Structures of layon PTCDI-C13 bilayers equilibrated on PMMA at 300 K (a) and at 400 K (b), together with the angular structural parameters of the first (c) and second (d) layer at 300 K and of the first (e) and second (f) layer at 400 K.

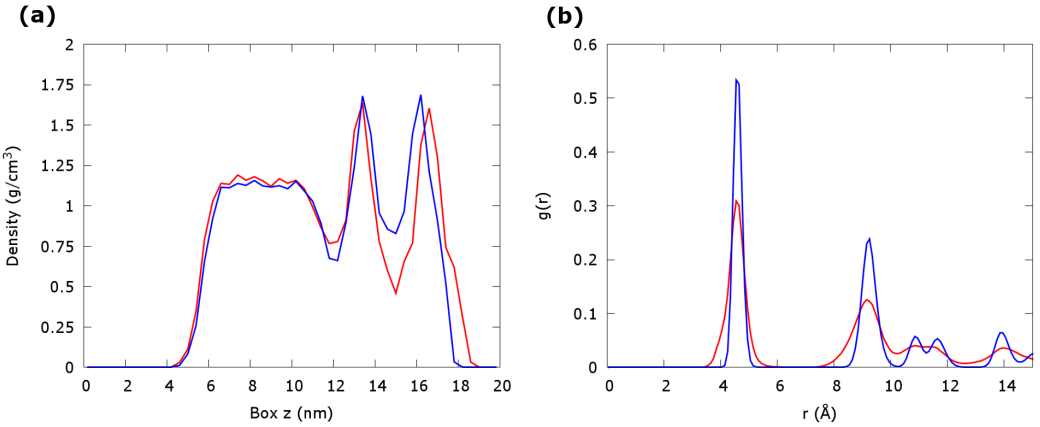

FIGURE 7.4: Density profiles (a) and g(r) (b) calculated for the layon PTCDI-C13 equilibrated on PMMA at 300 K (red) and at 400 K (blue).

equilibrated at 300 K on PMMA is represented in Figure 7.3a. The aggregation appeared similar as the case of monolayer equilibrated on PMMA at 300 K, with an increased disorder upon equilibration on PMMA, with the long alkyl chains that assist the packing of PTCDI-C13. The angular structural parameters of the first and the second layer are represented in Figure 7.3c and 7.3d, respectively. The layer at the interface with the PMMA shown a more ordered aggregation with respect to the second one, with an almost total CF configuration. This difference is ascribable to both the presence of vacuum above the second layer, and to the increased packing of the layer at the interface because of the sandwich between the two materials.

The application of the annealing at 400 K led to similar results as the monolayer case, with an increased molecular packing and order of the bilayer, as can be seen from Figure 7.3b. The angular structural parameters, reported in Figure 7.3e and 7.3f are the same for the two layers, showing the presence of the CF configuration only. The average COMs distance of the bilayer at 300 K and 400 K were very similar, with values around 4.60 Å. The tilt angle, as in the monolayer case, increased with the equilibrated temperature of the system, passing from 43.0° of the CF layon at 300 K to 47.0° upon annealing. The most impressive difference is related to the interlayer distance, which changes a lot upon annealing, decreasing from 32.5 Å at 300 K to 26.3 Å after annealing. The latter value is very similar to the experimental calculated value in PTCDI-C13 thin films after applying thermal treatments[5, 7, 25]. The density profiles and g(r) in the two cases, represented in Figure 7.4, reproduce similar results with the monolayer case. In bilayers, though, the difference in the density profiles are more emphasized. Above all, the density profile of the second layer is sharper and more shifted toward the PMMA surface. The g(r) resembled the same sharpening of the main and secondary peaks upon application of annealing.

The equilibrated structure of interdigitated PTCDI-C13 bilayer on PMMA is shown in Figure 7.5a. The interdigitated characteristic of the configuration is preserved after the equilibration on the rough surface, with the perylene cores maintaining an almost perfect packing in the bilayer, as confirmed by the angular structural parameters (see Figure 7.5c and 7.5d). The situation does not significantly change after the annealing at 400 K, as shown in Figure 7.5b and is confirmed, as before, by angular structural parameters (Figure 7.5e and 7.5f). Unlike the layon PTCDI-C13 case, in the interdigitated configuration, the first and second layer maintain the same molecular packing and aggregation, both at 300 K and at 400 K. This is probably due to the interdigitation itself, which makes the molecules more rigidly packed. This tendency to maintain the same molecular packing at room temperature and at 400 K can be also appreciated by observing the density profiles in Figure 7.6a, in which the profiles at different temperatures are almost exactly overlapped. Some differences are appreciable by observing the g(r) at different temperature. As a matter of fact, the peaks at 400 K are sharper and more defined respect to the ones at 300 K, even if they still are quite similar.

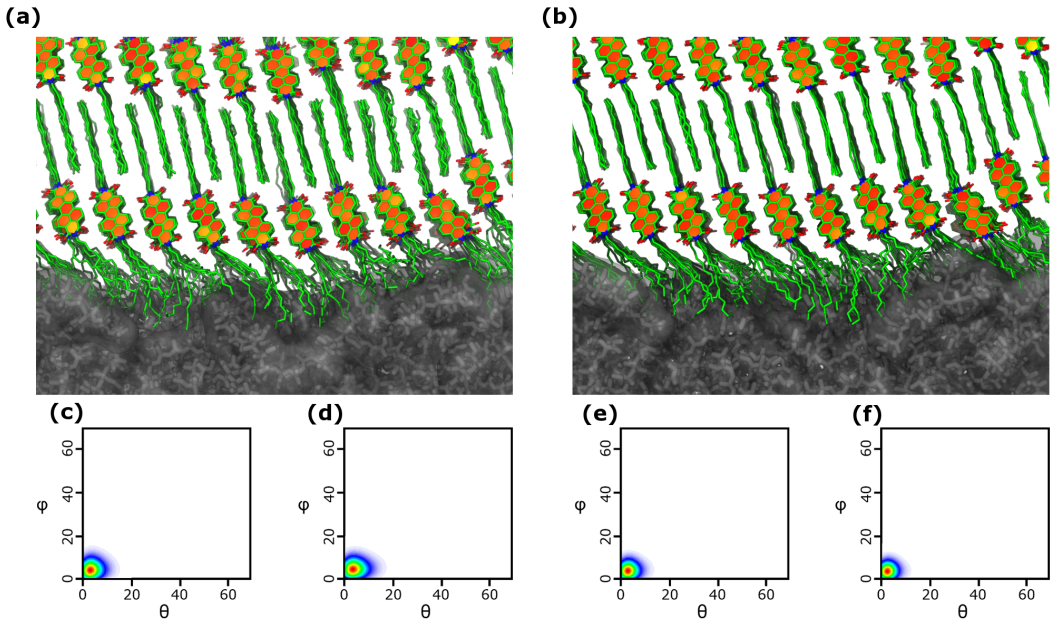

FIGURE 7.5: Structures of layon PTCDI-C13 bilayers equilibrated on PMMA at 300 K (a) and at 400 K (b), together with the angular structural parameters of the first (c) and second (d) layer at 300 K and of the first (e) and second (f) layer at 400 K.

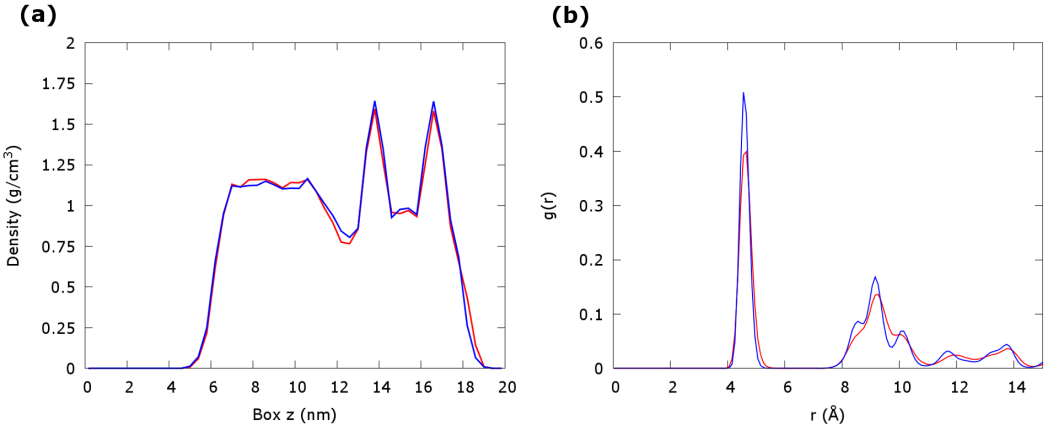

FIGURE 7.6: Density profiles (a) and g(r) (b) calculated for the layon PTCDI-C13 equilibrated on PMMA at 300 K (red) and at 400 K (blue).

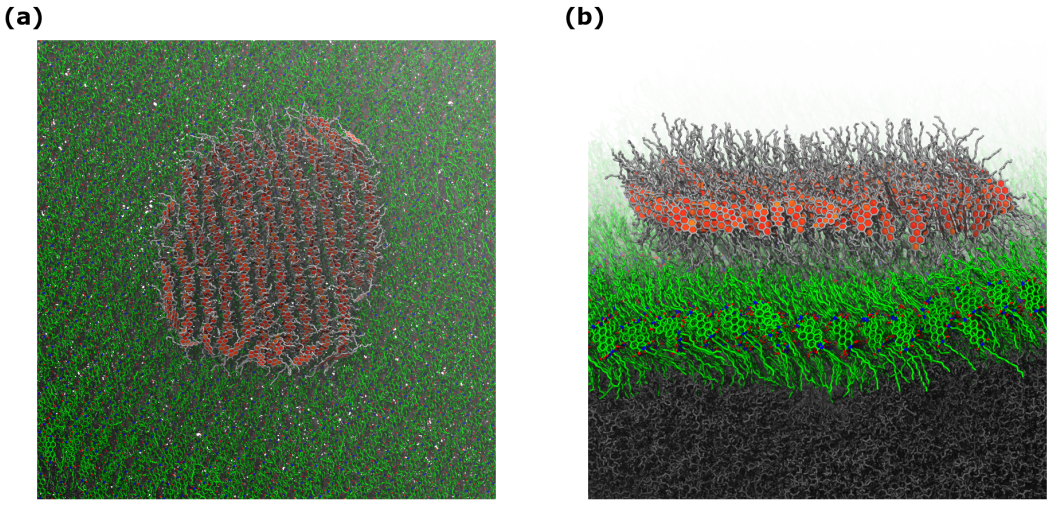

FIGURE 7.7: Top view (a) and side view (b) of a PTCDI-C13 island equilibrated on the first PTCDI-C13 layer at the interface with PMMA.

7.4 Formation and growth of PTCDI-C13 islands

From experimental characterization performed during the growth of PTCDI-C13 on a dielectric layer (SiO_2) in organic devices, Vasseur *et al.*[5] observed that the PTCDI-C13 grows according to a Stranski-Krastanov mode, i.e. a layer-plus-island growth. This means that, after the first complete monolayer grown on the substrate, the subsequent molecules will firstly aggregate in ordered islands on the PTCDI-C13 monolayer, and then, increasing the number of molecules of the system, they will coalesce to form bigger clusters of islands and, finally, the second complete monolayer will be formed (as described in section 2.7). These observations are mainly based on scanning probe techniques, such as AFM and STM, or by GIXD. These advanced techniques are able to follow the growth of materials during the deposition on a substrate, obtaining structural information. Here, atomistic MD simulations aiming at the modelling of the coalescence of two islands and the dynamics of a single island on the first complete monolayer of PTCDI-C13 on PMMA, were performed. Firstly, a 20x20 nm monolayer of PTCDI-C13 at the interface with PMMA was equilibrated for 10 ns at 300 K in an NVT ensemble. The morphology and dynamics of an isolated island grown on top of the first complete monolayer was studied by inserting an aggregate containing 250 PTCDI-C13 molecules (that is the average number of molecules forming a complete monolayer on a 10x10 PMMA slab) on top of the equilibrated PTCDI-C13 monolayer on PMMA, at a distance of 10 Å. The system was then equilibrated at 300 K for 5 ns in an NVT ensemble. In Figure 7.7 the equilibrated island is represented. The edges of the island are rounded, because the molecules try to minimize the contacts with the external vacuum, leading to a more compact aggregation. The shape of the PTCDI-C13 island resembles the topology of islands of PTCDI-C13 observed by AFM characterizations[7, 70, 215]. The angular structural parameters show

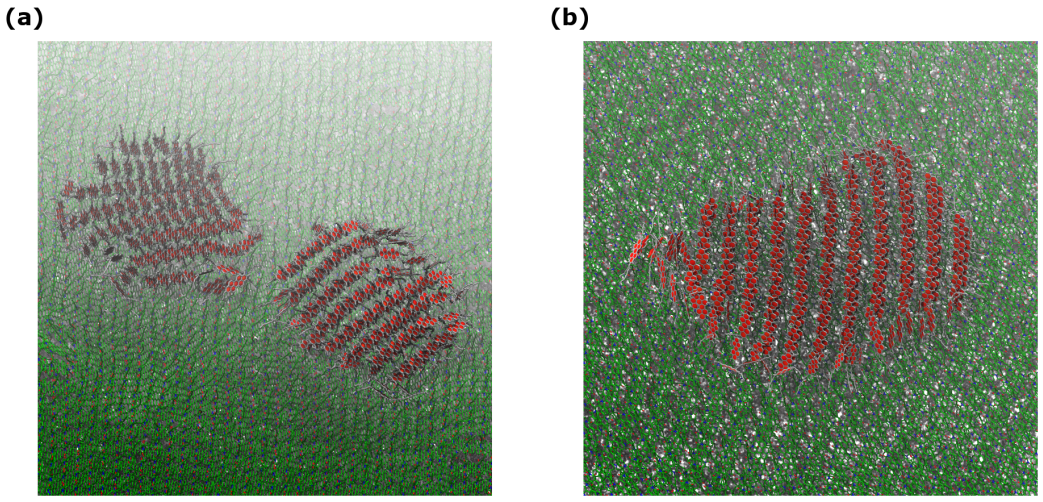

FIGURE 7.8: Top view of two different snapshots of the simulation of the coalescence between two small PTCDI-C13 islands on the PTCDI-C13/PMMA system:(a) the first interaction between the two islands and (b) the formation of the coalesced island.

a quite disordered aggregation, due to the particular shape of the islands, with a more ordered packing at the center, in which there is an interplay between CF and ST configurations.

In another set of simulations, two small PTCDI-C13 islands, containing 96 molecules each, were equilibrated on the same PTCDI-C13/PMMA surface as before. In the initial configuration, the two islands was at 10 Å from the surface and 5 Å from each other. The system was then equilibrated for 10 ns a t 300 K in an NVT ensemble. During equilibration, after an initial diffusion over the surface, the two islands approach and coalescence occurred, resulting in a bigger island. After an initial formation of a grain boundary between two distinct configurations, the PTCDI-C13 molecules packed in a single cluster, as shown in Figure 7.8b.

7.5 Kinetically-driven aggregation of PTCDI-C13 on PMMA

The morphology for the kinetic growth of PTCDI-C13 at the interface with PMMA was modeled (with a similar approach then developed in MIRTO, see Appendix A). Namely, each PTCDI-C13 molecule was initially inserted, with random rotation and random initial position along the x and y axes, in the vacuum region above a 10x10 nm PMMA surface, at a distance of 5 nm along the z axis. For each molecule insertion, a short non-equilibrium MD deposition run was initially performed, adding a constant value of 0.4 nm/ps to the z component of all atomic velocities of PTCDI-C13. A total simulation at 300 K for 500 ps in NVT ensemble was performed for each molecule inserted.

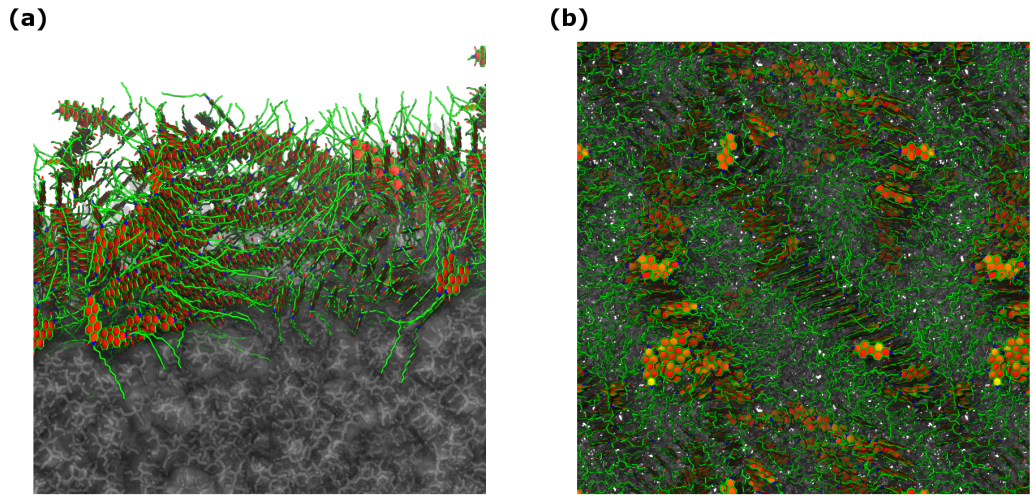

FIGURE 7.9: Side view (a) and top view (b) of the kinetically-driven aggregation of PTCDI-C13 on PMMA.

The first few PTCDI-C13 molecules deposited interact with the PMMA surface arranging in a flat-lying configuration, without interacting with the other molecules deposited. The first aggregates of PTCDI-C13 are observed when 50 molecules have been deposited on the surface, with cores interacting through π-π interactions, in a 3D-like growth. The first needle-like 1D stack aggregate of PTCDI-C13 molecules is observed with 100 molecules on the surface. This aggregate is formed by stacked PTCDI-C13 molecules packed along the [1 0 0] direction of the crystalline PTCDI-C13. This 1D aggregate enlarges by increasing the number of PTCDI-C13 molecules on the surface, initially increasing the 1D stacking along the [1 0 0] direction, and eventually, during deposition, adding stacked molecules along the [0 1 0] direction. The formation of another 1D aggregate occurred with increasing the number of molecules on the surface. At the end of the simulation, with 300 molecules deposited and relaxed on the PMMA surface, the two needle-like aggregates present defined configurations of the stacked molecules, ST and CF, with a preference for the more kinetic form ST. The main needle-like aggregate presents a more ordered aggregation than the second one. This is due to the less extension of the second aggregate along the [0 1 0] direction respect to the first one, as observed in the section 4.

7.6 PTCDI-C13 at the interface with graphene

In recent years, many organic electronic devices using graphene as electrode have been fabricated[102, 115, 154, 155, 223], due to its high flexibility and transparency, chemical and thermal stability, and high conductivity[224]. All these properties make graphene as one of the best candidates for devices where a transparent electrode is needed, like organic field-effect transistors. Moreover, graphene has also been found to be a good substitute for ITO in organic light-emitting diodes[100, 115, 131, 154, 156, 223]. The interface between perylene diimide derivatives and graphene has also been studied from both the experimental and the computational point of view. In particular, the interaction between PTCDA and PTCDI with graphene has been investigated[225]. All of them observed the formation of an interfacial layer of flat-lying molecules of the organic material on the graphene surface, due to the strong π-π interactions between the perylene cores and the graphene polyaromatic conjugated structure. Jeong *et al.*[24] reported an OFET fabrication in which graphene has been used as a transparent electrode and PTCDI-C13 as organic semiconductor, studying the effect of thermal treatments on the morphology and crystallinity of PTCDI-C13 at the interface with graphene. They observed a strong correlation between ordered aggregation of PTCDI-C13 molecules and annealing at high temperatures. Namely, whereas the PTCDI-C13 deposited on graphene at room temperature presented a disordered morphology, without a preferential aggregation, applying thermal treatments to the system formation of terraces of PTCDI-C13 was observed, hence related to the transition between flat-lying molecules to stand-up ordered aggregates. In this work, the nanoscale aggregation of PTCDI-C13 at the interface with the graphene was investigated by means of atomistic MD simulations by performing a fast deposition of PTCDI-C13 molecules on the surface of a graphene layer, in order to obtain a kinetic aggregation of the organic molecules on the surface. Furthermore, the effects of the temperature have been investigated by applying thermal treatments to the system, mimicking the experimental processing[24].

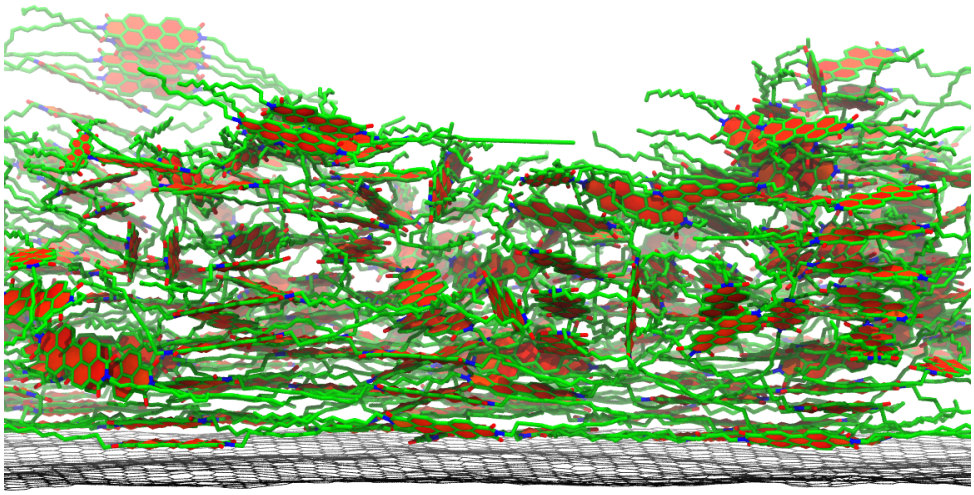

FIGURE 7.10: Morphology of the kinetically-driven aggregation of PTCDI-C13molecules on graphene.

7.7 Morphology of the PTCDI-C13/graphene interface

The interface between PTCDI-C13 and graphene was modeled by performing MD simulations. Firstly, a 10x10 nm graphene monolayer was modeled based on the OPLS force field[226] and equilibrated for 5 ns at 300 K. Then, each PTCDI-C13 molecule was initially inserted, with random rotation and random initial position along the x and y axes, in the vacuum region above the surface, at a distance of 5 nm. For each molecule insertion, a short non-equilibrium MD deposition run was initially performed, adding a constant value of 0.4 nm/ps to the z component of all atomic velocities of PTCDI-C13. A total simulation at 300 K for 100 ps in NVT ensemble was performed for each molecule inserted. The short equilibration time for each molecule mimic an experimental very fast deposition rate, which is known to result in a kinetic aggregation. The final system, consisting of 350 PTCDI-C13 molecules on graphene, is shown in Figure 7.10. The molecules exhibited a typical kinetic aggregation at the interface, presenting highly disordered clusters, with the formation of very small crystallites and no preferential configuration.

The strong π-π interactions between PTCDI-C13 and graphene surface act as an energy barrier to the ordered aggregation of PTCDI-C13 material. In order to allow the molecules to overcome this energy barrier, in analogy with experiments[24], thermal treatments were applied. In particular, the PTCDI-C13 molecules were annealed at 600 K for 150 ns in an NVT ensemble, whereas the graphene substrate was maintained at 300 K. At the end of the simulation, the system was cooled to 300 K and equilibrated for 10 ns. In the first ns of the simulation, PTCDI-C13 molecules, especially the ones more distant from the graphene substrate, began to stand up and aggregate in a layered configuration. The first layer of PTCDI-C13 at the interface with graphene remained in the flat-lying configuration, forming the interfacial layer.

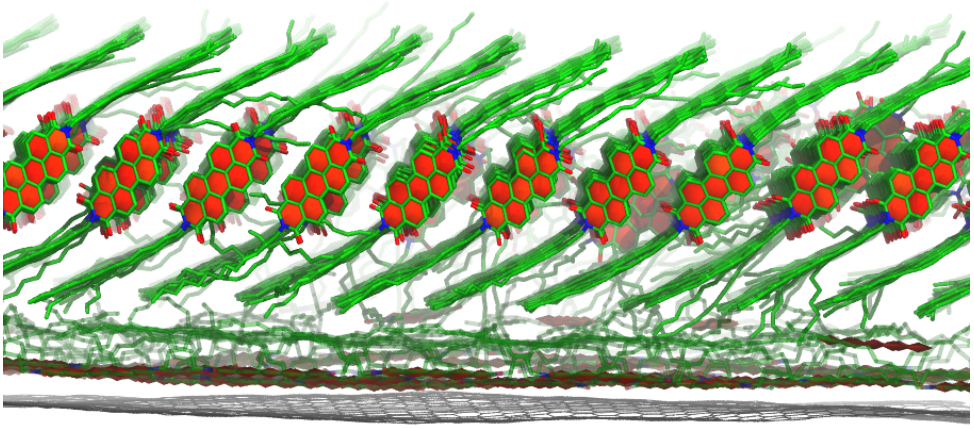

FIGURE 7.11: Formation of a complete monolayer after the application of thermal annealing, with the presence of an interfacial layer composed of flat-lying PTCDI-C13 interacting with the graphene layer.

During the annealing, the molecules above the interfacial layer aggregated to form a monolayer on top of the interfacial layer. The monolayer formed improved its order by interacting with other PTCDI-C13 molecules, increasing the π-π stacking interactions, eventually reaching a stable configuration, with an almost completely ordered CF molecular packing, as shown in Figure 7.11. The height of the monolayer was found to be about 25.8 Å, in good agreement with calculated height of PTCDI-C13 terraces in experiments[5, 7, 24, 25, 63]. The formation of an interfacial layer with the growth of layers above it has been observed in other research on organic materials grown on graphene[33, 81, 100, 115].

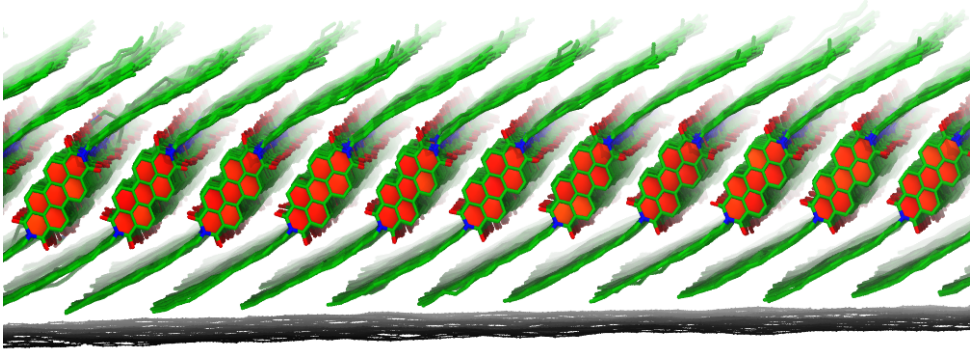

FIGURE 7.12: Formation of a complete monolayer after the application of thermal annealing and potential switching.

In order to obtain the most thermodynamically stable form of aggregation of the PTCDI-C13 at the interface with graphene substrate, the same thermal

treatments were applied to the PTCDI-C13 molecules, modifying the interaction potential between PTCDI-C13 and graphene. Namely, the ε term of the Lennard-Jones potential (see section 3.3.6) of graphene was decreased by one order of magnitude (1/10), resulting in a lower interaction with the PTCDI-C13 cores, thus turning the graphene in an almost 2D inert surface. This potential switch was intended to allow the PTCDI-C13 at the interface with graphene to overcome the high energy barrier between the flat-lying and stand-up configurations, without the presence of the interfacial layer. Physically, the lower interaction between PTCDI-C13 and graphene obtained by this potential modification, can represent the occurrence of defects or the chemical functionalization of the graphene surface. In this regard, to obtain a complete monolayer at the interface without the presence of the interfacial layer, this simulation was performed on a system composed of 250 PTCDI-C13 molecules in a kinetic aggregation on the graphene surface (obtained with the same approach described before). In the first steps of the simulation, the PTCDI-C13 molecules began to form an ordered monolayer on the surface of graphene, without the formation of the interfacial layer. The monolayer presented some grain boundaries, due to the different PTCDI-C13 ordered clusters interacting with each other. During the annealing, the PTCDI-C13 molecules ordered in a monolayer with a single configuration. At the end of the simulation, the PTCDI-C13/graphene interaction potential was restored and the system equilibrated for 10 ns at 300 K. The final morphology of the PTCDI-C13 monolayer, shown in Figure 7.12, can be defined as the most thermodynamically stable for PTCDI-C13 molecules on graphene. The results obtained by MD simulations were found in good agreement with the paper by Jeong *et al.*[24]. In this paper, the authors studied the effects of thermal treatments to the PTCDI-C13 grown on graphene. They performed XRD experiments before and after the thermal treatments, observing a remarkable improvement of the structural properties of the aggregate, with well defined spikes in the XRD patterns (see Figure 7.13a). They also found, by performing AFM imaging, that the morphology of as-cast PTCDI-C13 on graphene resulted in ellipsoidal ball-like small grains, disordered and without the presence of terraces (see Figure 7.13b), as we obtained by the fast deposition of the PTCDI-C13 molecules (see Figure 7.10). By the application of thermal treatments at 130 °C (about 400 K), however, they observed an increasing in the crystallinity of PTCDI-C13 and also an improvement of the morphology and structure of aggregates (see Figure 7.13c), with the appearance of terraces with height of about 25.5 Å, in good agreement with the results we obtained by MD simulations (25.8 Å). Although Jeong *et al.* did not observed the presence of an interfacial layer in this system, our simulations indicate the likely occurrence of flat-lying molecules between graphene and PTCDI-C13 ordered islands.

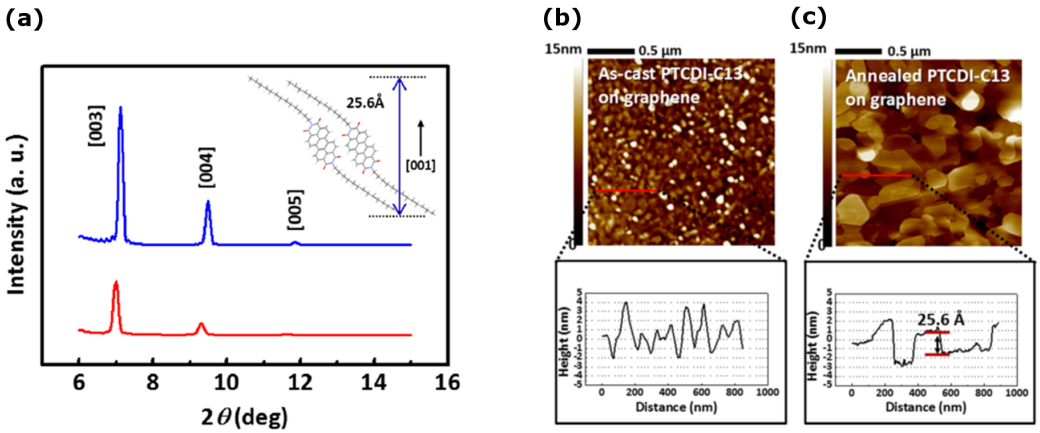

FIGURE 7.13: XRD spectrum (a) of the as-cast (red curve) and the annealed (blue curve) PTCDI-C13 on graphene. AFM topologies of the as-cast (b) and annealed (c) PTCDI-C13 on graphene. Adapted from Ref. [24].

7.8 Conclusions

In the first part of the Chapter, the morphology of PTCDI-C13 monolayer in the CF configuration at the interface with PMMA was investigated. In particular, the interaction between the two materials was analysed by computing structural parameters, comparing the results obtained at 300 K with the ones obtained by applying thermal treatments (400 K), observing an improvement on the morphology of PTCDI-C13 upon the application of annealing, as also observed in experiments[5, 25, 198]. Furthermore, the 3D layered aggregation was investigated by equilibrating structures of PTCDI-C13 bilayer in the layon and interdigitated configurations. The layon bilayer exhibited the same behaviour of PTCDI-C13 monolayer, with enhancement in the aggregation upon annealing, showing an interlayer distance in good agreement with experiments. Interdigitated bilayer shown a stable configuration either at 300 K and at 400 K, with a slightly improved aggregation at 400 K.

The formation and aggregation of islands on top of the PTCDI-C13 monolayer on PMMA was studied, observing that the island maintained the morphology of the monolayer, with a small increase of disorder. Moreover, the coalescence of two islands was simulated by equilibrating two little islands on top of the same surface.

Finally, the kinetically-driven aggregation of PTCDI-C13 on the PMMA surface was studied by performing a fast growth simulation, obtaining PTCDI-C13 aggregates with a kinetic morphology, which can be correlated to a very fast growth of PTCDI-C13 on a dielectric layer.

The interface between PTCDI-C13 and grapehene was also investigated. In particular, the PTCDI-C13 molecules were equilibrated, one-by-one, on the graphene surface, with fast simulations at 300 K, in order to obtain the most kinetic aggregation of the molecules at the surface. After that, applying an annealing at high temperature, the formation of an ordered monolayer on top of

an interfacial layer was observed. Furthemore, we obtained the most thermodynamic aggregation of PTCDI-C13 on the graphene by performing the same annealing and simultaneously decreasing the interaction potential between PTCDI-C13 and graphene, observing the formation of the ordered monolayer without the presence of the interfacial layer. Calculating the height of the monolayer obtained, we found them in good agreement with experiments on the same interface[24].

Chapter 8

Nanoscale morphology and charge injection rates at the interface between DPBIC and ITO

Organic light-emitting diodes are nowadays expanding in the popular market, with applications ranging from displays to lighting. Nevertheless, many aspects affecting their lifetime and efficiency, and thus the overall performances of devices, are poorly studied, both theoretically and experimentally. In particular, one of these issues is related to the processes leading to degradation of materials constituting the layers of OLEDs, mostly occuring at the interfaces[4, 23, 48, 227]. In this respect, computational models provide useful tools to gain a better understanding about the nanoscale morphology of interfaces and the charge injection from metallic electrodes to the organic semiconductor layer, in order to develop devices with enhanced performances[52, 55–57, 228]. In this chapter, an integrated multiscale approach based on molecular dynamics (MD) and density functional theory (DFT) was applied to model realistic metal/semiconductor interfaces and the electronic processes occuring upon charge injection in OLEDs. In particular, the morphology and charge injection properties at the interface between the metallic anode and the organic layer in an electrode/organic junction were analysed. Namely, the hole injection from a thin-film of indium tin oxide (ITO), commonly used as anode electrode, to an hole-transport (and electron-blocking) layer constituted by an amorphous undoped thin-film of the Iridium complex DPBIC (Tris[(3-phenyl-1H-benzimidazol-1-yl-2(3H)-ylidene)-1,2-phenylene]Ir) was targeted. The understanding of charge injection processes at the metal/organic interface, in complex morphologies, requires an in-depth analysis of intrinsically different phenomena. In the presented approach, large-scale molecular dynamics (MD) calculations were first performed to simulate the morphology of nanoscale aggregates at the metal/organic interface. In particular, a realistic description of interfaces between the metal electrode and the amorphous organic material was achieved through the application of an innovative simulation protocol, based on equilibrium and non-equilibrium MD, using the GROMACS package[183]. The morphology obtained by MD simulations was then used to evaluate structural properties, in the form of distributions, and for the subsequent evaluation of electronic properties and injection mechanism at interfaces. To this end, DFT calculations were used to compute energy level alignments and electronic couplings at the metal/organic interface. These values were then used to compute the distribution of injection rates for

nanoscale aggregates of DPBIC molecules at the interface with ITO. This approach allows to correlate the morphological properties of materials at interfaces with electronic processes, including charge injection and transport, leading to a multiscale computational model able to link simulations and experiments.

This work has been carried out in the framework of the H2020 project "Modeling Stability of Organic Phosphorescent Light Emitting Diodes" (MOSTOPHOS) under the Grant Agreement No. 646259.

TABLE 8.1: Calibration DFT calculations on the In_2O_3 cubic bulk structure. US: UltraSoft pseudopotentials. MT: Martins-Troulliers pseudopotentials. Energy cut-off (rcut: wavefunction, dcut: electron density) in Ry; cell parameter (a) in Å.

XC functional	Pseudo	r_{cut}	d_{cut}	k-point sampling	a
LDA	US	30	120	3 3 3	10.111
PBE	US	30	120	3 3 3	10.321
		50	200	3 3 3	10.404
	MT(In_d^{10})	50	200	3 3 3	9.864
		70	280	3 3 3	10.284
		80	320	3 3 3	10.334
	MT(In_d^0)	70	280	3 3 3	10.011
		80	320	3 3 3	10.047

8.1 Model of the ITO electrodes

In_2O_3 bulk structure

A model of the ITO electrode surface was generated from the corresponding bulk system. In turn, to obtain the bulk structure of ITO, we firstly modeled the undoped parent In_2O_3. The thermodynamically stable phase of indium oxide is a bixbyite body-centered cubic structure, with 40 atoms in the symmetric unit cell (80 in the cubic unit cell), formally related to a vacant cubic fluorite (CaF_2) crystal[152, 229, 230]. An initial model of the In_2O_3 bulk crystal was prepared according to available experimental data[231]. To calibrate simulation parameters against structural data, a set of DFT calculations with different functionals was carried out (see Table 8.1), performed by using the QUANTUM ESPRESSO package[178].

Both local-density and gradient-corrected exchange correlation functionals were tested. As expected, ultrasoft (US) pseudopotentials are able to reproduce experimental structure with good accuracy using a relatively low energy cut-off. However, the use of US pseudopotentials hampers the subsequent calculation of electronic coupling terms, in a plane-wave expansion of the wavefunction. Therefore, Martins-Troullier (MT) pseudopotentials[232] are preferred for all DFT calculations of injection rates. Excellent agreement between the optimised cell parameter (10.047 Å) and the experimental value (10.117 Å)[231] was achieved by using the PBE exchange correlation functional and MT pseudopotentials for In and O atoms with an energy cut-off of 80 Ry and, remarkably, with a valence-only pseudopotential for In (3 electrons in the valence shell). At this level of theory, the computed band gap for In_2O_3 was found to be 1.85 eV, which is about 1 eV smaller that the value currently accepted[233]. However, this discrepancy is ascribable to the well-known underestimation of the band gap related to the use of gradient-corrected XC functionals and does not affect other electronic properties, such as electron density[233].

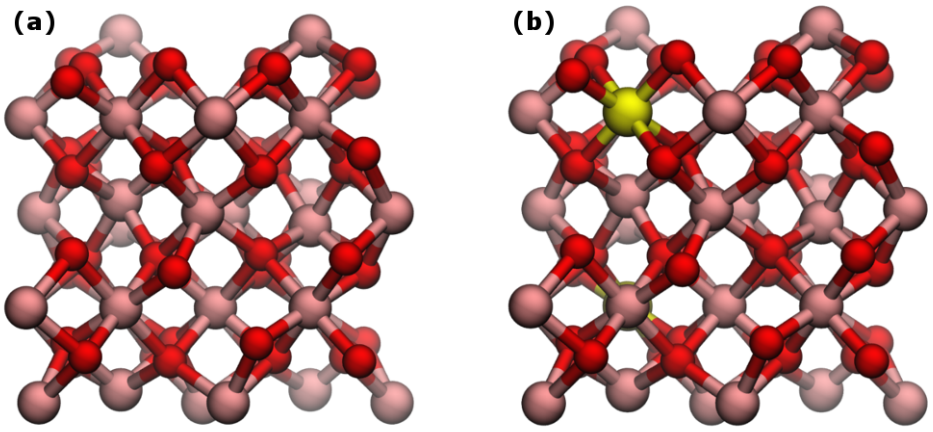

FIGURE 8.1: Unit cells of In_2O_3 (a) and ITO 5 wt% (b).

TABLE 8.2: Computed cell length (in Å) of ITO bulk models at different doping.

Doping level	Defect	a cell
5 wt%	Sn_{In}^{4+}	10.077
	$2\ Sn_{In} \cdot O_i$'	10.072
10 wt%	Sn_{In}^{4+}	10.106
	$2\ Sn_{In} \cdot O_i$'	10.092

ITO bulk structure

Models for the bulk ITO crystal were obtained from relaxed In_2O_3 structures, with a variable amount of Sn doping. Namely, two different doping modes were considered. In the electronically-compensated doping, tin ions (Sn^{4+}) substitute In^{3+} atoms, resulting in an excess positive charge. In the ionically-compensated doping, which is likely to occur at high tin concentrations and oxidizing conditions, indium ions are substituted by ($2\ Sn_{In} \cdot O_i$') defects, with interstitial oxygen atoms occupying the vacancy sites of In_2O_3[153, 233]. Doping concentrations of 5% and 10% in weight of tin content were modeled, in line with common ITO samples[153]. The position of substitutional Sn ions was randomly selected from the metallic sites of the In_2O_3 crystal. The electronic structure of ITO bulk models was simulated with the same set-up used for DFT calculations on In_2O_3, using a MT pseudopotential for the Sn sites. In Figure 8.1 In_2O_3 and ITO doped at 5wt% are represented. The cell length of DFT optimised ITO models, at different doping concentration and with both electronically- and ionically-compensated doping, is shown in Table 8.2. The variation in the cell side length of In_2O_3 upon tin doping is below 1%.

TABLE 8.3: Potential parameters used in molecular mechanics calculations of In_2O_3 and ITO systems.

Buckingham terms	Pair	A (eV)	1/B ($Å^{-1}$)	C (eV $Å^{-6}$)
	In^{3+} O^{2-}	2719.77	0.2917	0.0
	Sn^{4+} O^{2-}	2180.89	0.3076	0.0
	O^{2-} O^{2-}	25.41	0.6937	32.32
Bonded terms	Pair	K (eV $Å^{-2}$)		
	O^{2-} O^{2-}	20.53		

ITO force-field

An atomistic force-field was defined, able to reproduce the structural properties of ITO electrodes, to be used in MD simulations of metallic surfaces. For In_2O_3 and ITO, a non-bonded force-field was used. The use of non-bonded interaction terms only allows the simulation of complex morphologies, dynamical effects, heat treatments and processing, which can occur at metal surfaces. The force-field for In_2O_3 and ITO systems was defined in term of pairwise contributions to Coulomb and repulsion/dispersion energies. These latter, constituting van der Waals interactions, were described in terms of a Buckingham potential (see section 3.3.6). Coulombic terms were described as interaction between point charges, assigned to atoms on the basis of the formal ionic charge (In: 3+; Sn: 4+; O: 2-). In addition, polarization of oxygen atoms was taken into account by considering a pair of opposite point charges (core and shell), for each atomic center, attached to each other through an harmonic potential (see section 3.3.6).The set of parameter used is taken from ref. [153] and adapted to the current GROMACS implementation. The full set of parameters used is shown in Table 8.3. The optimised unit cell side lengths are 10.116Å, 10.129 Å and 10.148 Å for In_2O_3 and ITO at 5 and 10 wt% tin doping, respectively. Therefore, this set of parameters provided structural data for In_2O_3 and ITO bulk crystals in excellent agreement with experimental values[153]. Moreover, short MD equilibrations at room temperature in an NPT ensemble (in which all cell parameters were allowed to relax) and annealing at 500 K (in the same ensemble) suggested a remarkable structural stability of the simulated systems, as indicated by the computed In-In and O-O radial distribution functions, shown in Figure 8.2.

ITO surface

From the bulk system, a metal slab was obtained by cleaving the cubic crystal along the (111) low-index surface, which is the most thermodynamically stable one [152] Both oxygen-terminated and metal-terminated surfaces were considered, with an overall slab thickness of about 6-7 Å, corresponding to 9 atomic layers. Moreover, the effect of hydrogen saturation of O-terminated surfaces was also considered. The resulting slab, with an hexagonal unit cell (from 162

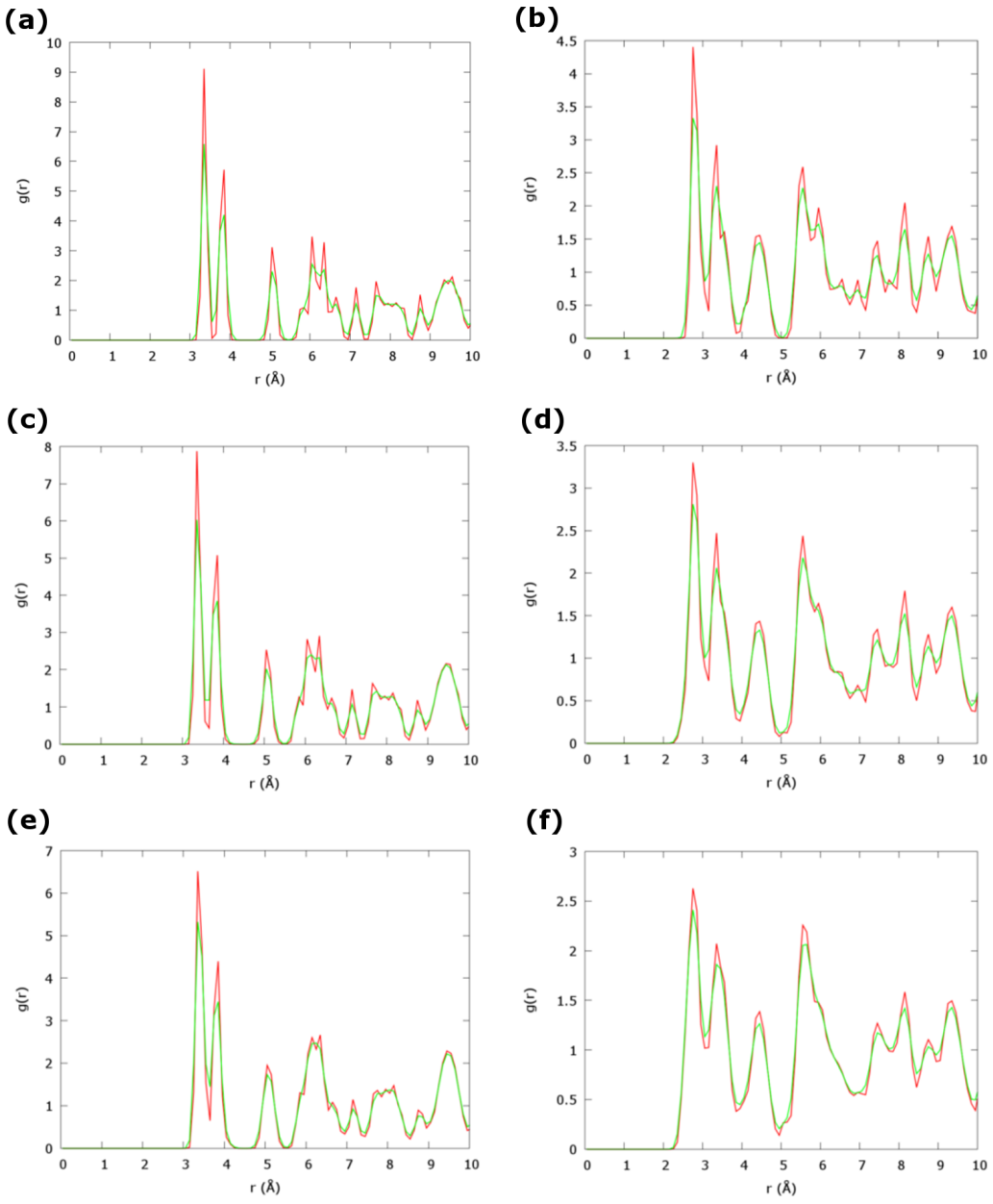

FIGURE 8.2: Computed radial distribution function for In_2O_3 In-In (a) and O-O (b), ITO 5 wt% In-In (c) and O-O (d) and ITO 10 wt% In-In (e) and O-O (f) bulk crystals, as a function of temperature, at 300K (red) and 700K (green).

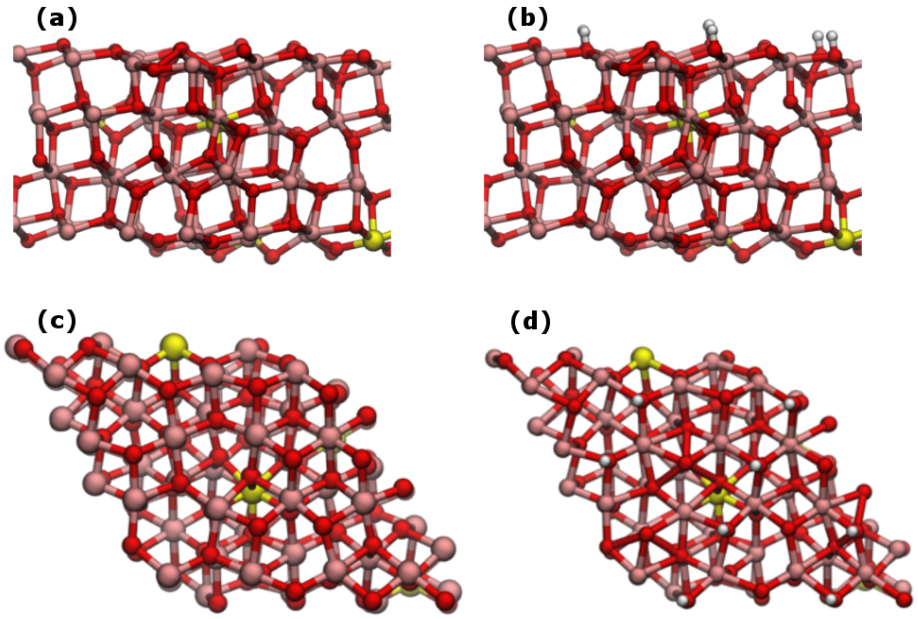

FIGURE 8.3: DFT optimised geometry of the 5 wt% ITO slabs exposing the (111) surface, both oxygen-terminated (side view (a) and top view(c)) and hydrogen-terminated (side view (b) and top view (d)).

to 164 atoms, depending on the doping level), was optimised by DFT, with fixed cell volume and constraining the position of the four bottom-most atomic layers. The optimised geometries of 5 wt% ITO slabs models exposing the (111) surface, both O- and H- terminated, are shown in Figure 8.3. For the simulations described in this chapter, only the 5 wt% O-terminated slab was used. From this slab, a 2-dimensional supercell was generated by replicating the DFT unit cell. The size of the slab was chosen large enough to allow for subsequent growth of an amorphous organic layer of DPBIC molecules. Moreover, the supercell approach allows a reduction of the slab unit cell symmetry, leading to a change of the angle between the crystal axis from 120°to 90°. A vacuum region of about 10 nm was inserted in the direction of the box orthogonal to the ITO surface, to avoid spurious interaction between slab images. The cell length of the ITO slab obtained was about 5x5 nm. The metal slab supercell were relaxed by constant-volume (NVT) MD simulations. An annealing/quenching cycle of 1 ns at a temperature of 500 K was also performed to improve surface relaxation, followed by relaxation at room temperature.

8.2 DPBIC model

DPBIC force-field

The DPBIC molecule was modeled with the OPLS-AA force field[226], using both bonded and non-bonded terms. Non-bonded parameters for Iridium were taken from the Universal force-field. Atomic charges were obtained by a RESP fit of the DFT electronic density, computed at the B3LYP/6-31G* level of theory. Unfortunately, accurate experimental structural data on the DPBIC molecule is not available. However, the overall RMS deviation of atomic positions against the DFT optimised geometry is about 0.15 Å for non-hydrogen atoms. The electronic structure of the organic molecule was assessed with a computational set-up that is compatible with that used in calculations of the bulk metal. Namely, MT pseudopotentials (taken from http://www.quantum-espresso.org) were used for all atomic species (Ir, N, C, H) of the DPBIC molecule, with the PBE exchange-correlation functional and a wavefunction cut-off of 80 Ry. For subsequent accurate evaluation of weak molecule/substrate or molecule/molecule interactions, the Grimme approximation[214] to dispersion interactions was included in calculations. The computed HOMO and LUMO energies are 3.7 and 1.0 eV, respectively. The resulting computed HOMO-LUMO gap is of 2.6 eV. On the basis of this force-field, amorphous bulk aggregates of DPBIC were simulated by MD. To this end, DPBIC molecules were inserted into a cubic simulation box, annealed at 500 K and subsequently equilibrated at room temperature in the NPT ensemble. Model systems containing 100, 200 and 500 molecules in the simulation box were prepared, to monitor convergence of the bulk properties as a function of the system size. The resulting equilibrated aggregate exhibits a density of about 1.41 g/cm^3 (1.40 g/cm^3 for the 100 molecule model) and a radial distribution function for molecular centers of mass peaked at about 11Å, as shown in Figure 8.4.

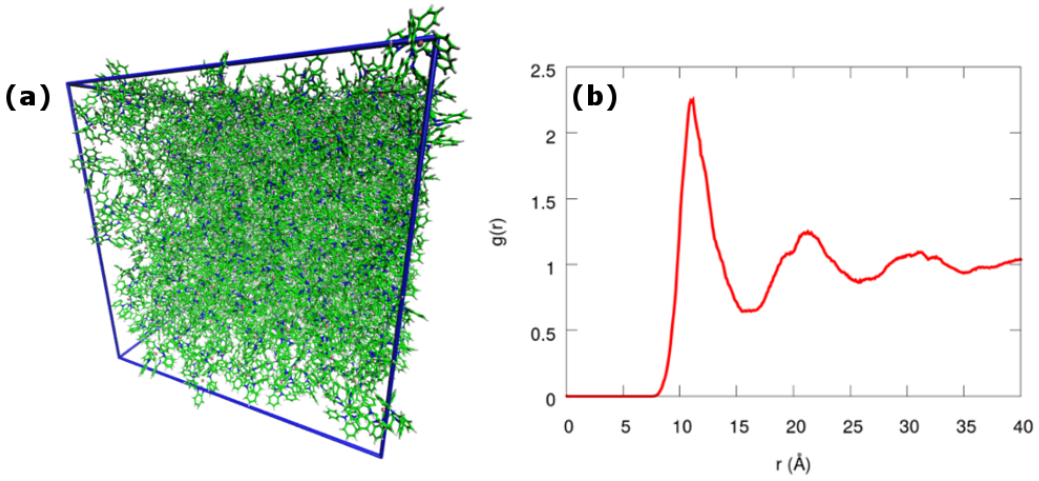

FIGURE 8.4: Box of 500 equilibrated DPBIC molecules (a) and resulting g(r) for the molecular centers of mass (b) at 300K.

Force-field for the metal-molecule interaction

The interaction between DPBIC molecules and the ITO was described in terms of an interaction potential including Lennard-Jones and Coulomb parameters. For consistency with the atomistic interaction potentials of the isolated metallic and molecular moieties, respectively, atomic charges are taken from the force-fields used in the isolated species. For the DPBIC molecule, LJ parameters are used as described above. For ITO, parameters are taken from the Universal Force Field for metal atoms and from OPLS for the oxygen atoms. Cross terms are obtained by standard Lorentz-Berthelot rules. The implementation of two distinct functional forms for van der Waals interactions (Buckingham (see section 3.3.6 terms for the metallic systems and LJ (see section 3.3.6) terms for the organic molecule and for the metal/molecule interaction, respectively) requires the implementation of tabulated potentials in GROMACS. This force-field provides interaction energies and equilibrium distances that are in good agreement with values computed at the DFT level, including dispersion corrections, as shown in Figure 8.5. It is worth noting, however, that also DFT calculations can be affected by inaccuracies in evaluating the interaction between weakly-bounded systems.

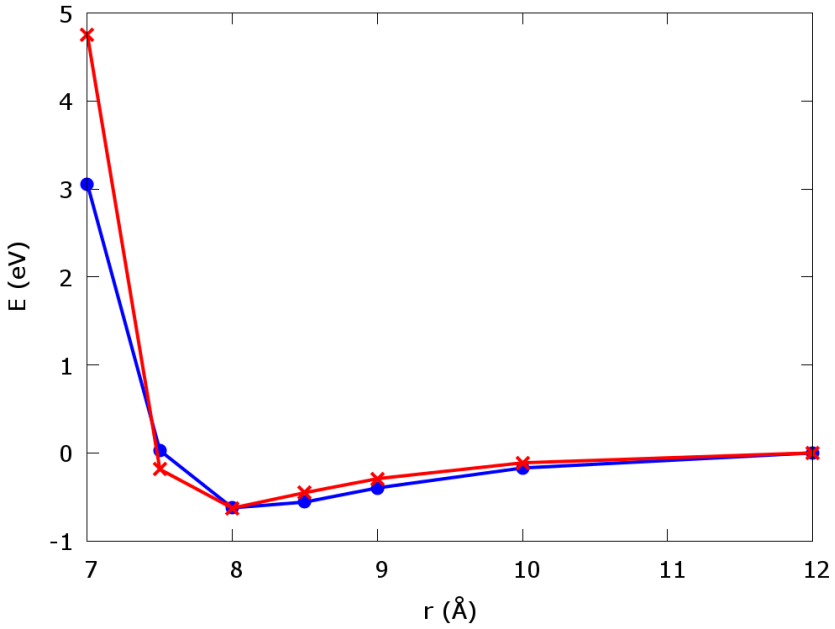

FIGURE 8.5: Comparison between the interaction energy, as a function of distance, for a DPBIC molecule adsorbed onto an ITO surface, computed at the DFT (red) and FF (green) levels.

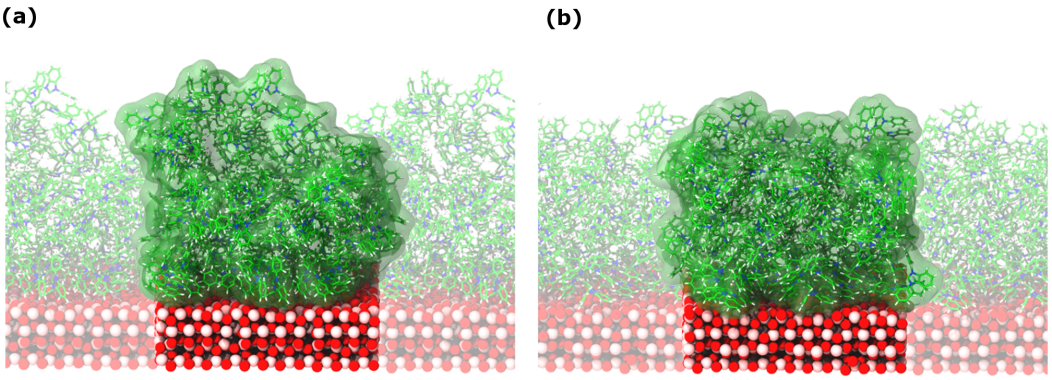

FIGURE 8.6: Representative configurations of kinetic (a) and thermodynamic (b) aggregates of DPBIC molecules on the model ITO surface. The shaded area represents periodic images of the simulation box.

8.3 Modelling of the ITO/DPBIC interface morphology

The interface morphology between DPBIC and the electrode was modeled by simulating the growth of an amorphous layer of organic molecules onto a relaxed ITO slab, through a combination of non-equilibrium and equilibrium MD simulations. This approach enables the realistic description of complex interface morphologies and, at the same time, a statistical variability related to the replication of the same thermodynamical systems with different initial conditions. Namely, DPBIC molecules were consecutively added to the simulation box and relaxed onto the ITO surface, thus mimicking the growing mechanism in vapor-phase deposition techniques. Despite a much smaller time scale for the growth of the organic layer in simulations, our approach allows the correlation between growth conditions and morphology by tuning simulation times and annealing temperatures. Formation of the electrode/organic interface was realized by iteratively inserting DPBIC molecules, equilibrated at 300K, to the 5x5 nm ITO 5 wt% O-terminated slab model. Each molecule was initially positioned in the vacuum region above the slab, at a distance of about 5 nm, with a random in-plane displacement and rotation. For each molecule insertion, a short (10 ps) non-equilibrium MD run was initially performed, adding a constant value of 0.4 nm/ps to the z component of all atomic velocities of DPBIC. In our simulations, all DPBIC molecules get into contact with the surface in this MD time frame. In a first set of simulations, a short (100 ps) MD equilibration run at 300 K was performed after insertion of a new DPBIC molecule to the ITO surface. The short equilibration time between consecutive insertions of molecules to the organic layer at room temperature, simulates the experimental conditions realized at high growth rates, corresponding to a kinetically-controlled growth mode. In a second set of simulations, a longer (1 ns) MD run was performed after insertion of each new DPBIC molecule into the system, with a temperature ramp, controlled by a thermostat. In particular, after insertion of each DPBIC molecule the system was equilibrated at 300 K (200 ps), annealed to

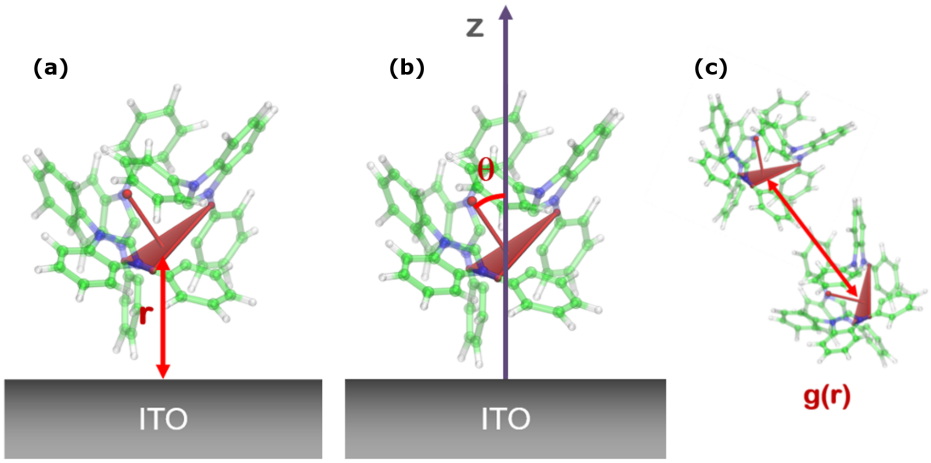

FIGURE 8.7: Radial (a) and angular (b) structural parameters defining the distance and orientation of DPBIC molecules with respect to the ITO surface; radial pair distribution function between DPBIC molecules (c).

500 K (in 100 ps), equilibrated at 500 K (300 ps), quenched to 300 K (200 ps) and equilibrated at 300 K (200 ps). This second set of simulations aims at reproducing the conditions for thermodynamically-controlled growth of DPBIC aggregates on the ITO surface, which experimentally occur at low growth rates or upon application of heat treatments. Indeed, annealing at high temperature, is expected to increment the diffusion of DPBIC molecules on the ITO surface, improving aggregation and molecular packing. For each simulation sequence, about 50 DPBIC molecules were deposited onto the 5x5 nm ITO model, generating an organic layer with a thickness of about 5 nm. Each simulation process was repeated 100 times with different initial conditions. Representative configurations of DPBIC aggregates on ITO for the two growth modes considered are shown in Figure 8.6.

8.4 Distribution of the structural parameters

The morphology of the DPBIC/ITO interaction was analysed in terms of radial and angular structural parameters, identifying the distance and the orientation of individual DPBIC molecules with respect to the underlying metal surfaces. The distance between a DPBIC molecule and the ITO surface is defined as the difference between the z coordinate of the center of mass of the DPBIC (coinciding essentially with the Ir center) and the average value of the z component of the coordinates of the topmost atomic layer of the ITO slab (see Figure 8.7). The orientation of the DPBIC with respect to the ITO slab is defined in terms of the three-fold axis, orthogonal to the average plane connecting the C-N vector of the ligands to the metal center. The orientation of a DPBIC molecule is thus defined as the angle between this plane and the z axis (see Figure 8.7). In addition, the molecular aggregation of DPBIC is also assessed in terms of the radial distribution function of the centers of mass (see Figure 8.7). The set

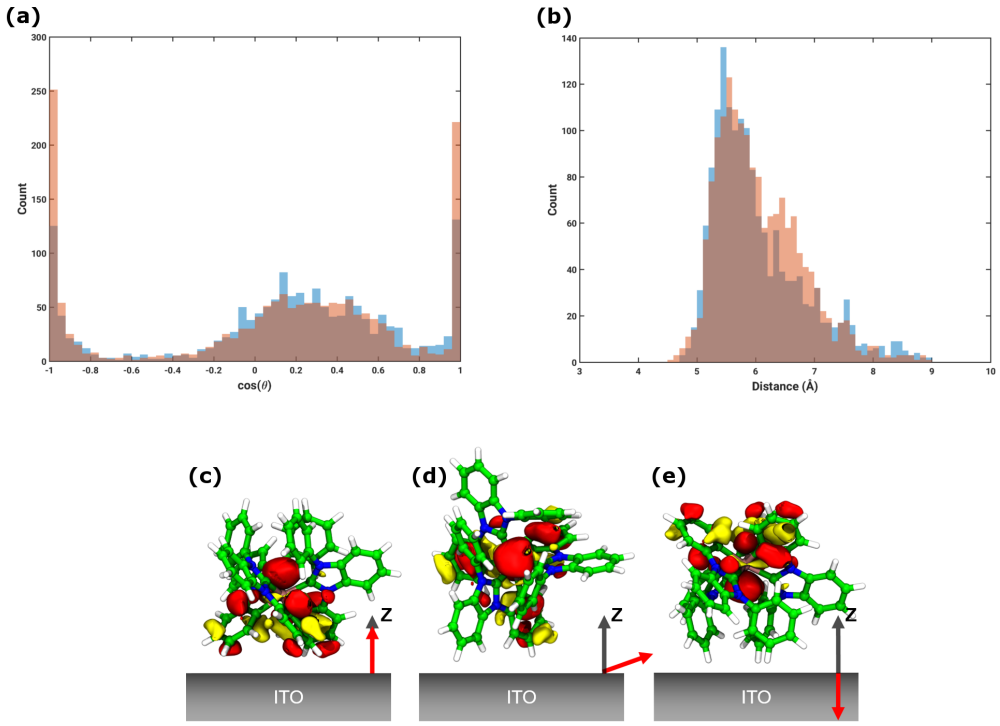

FIGURE 8.8: Histograms of the distribution of the DPBIC/ITO distance (a) and orientation (b), defined in terms of the radial and angular parameters described above, for molecules at the interface in the kinetic (blue bars) and thermodynamic (red bars) growth modes. Molecular configuration and HOMO isosurface for the three most likely orientations of DPBIC with respect to the ITO surface: (c) $\theta = 0°$ (d) $\theta = 75°$ (e) $\theta = 180°$.

of morphologies obtained by the MD simulations described above was analysed in terms of these structural parameters, considering molecules at the interface (within a distance of 0.9 nm from the ITO surface) only. The resulting distribution of the radial and angular structural parameters for the two growth modes considered is shown in Figure 8.8. The analysis of interface configurations suggests a distribution of DPBIC/ITO distances peaked at about 6 Å in both (kinetic and thermodynamic) growth modes. This distance is about 1.5 Å lower than the equilibrium distance for an isolated DPBIC surface on ITO, thus indicating a collective effect of DPBIC aggregates in inducing a stronger interaction with the surface. Moreover, the distribution of DPBIC orientations at the interface with ITO exhibits three major maxima, peaked at about 0, 75, and 180° respectively, with a preference for the 0/180° orientation. In particular, the 0 and 180 ° orientations seem more favourite in the thermodynamic growth respect to the kinetic, as shown in the distributions in Figure 8.8 The occurrence of three preferential orientations can be ascribed to the peculiar symmetry of DPBIC substituents.

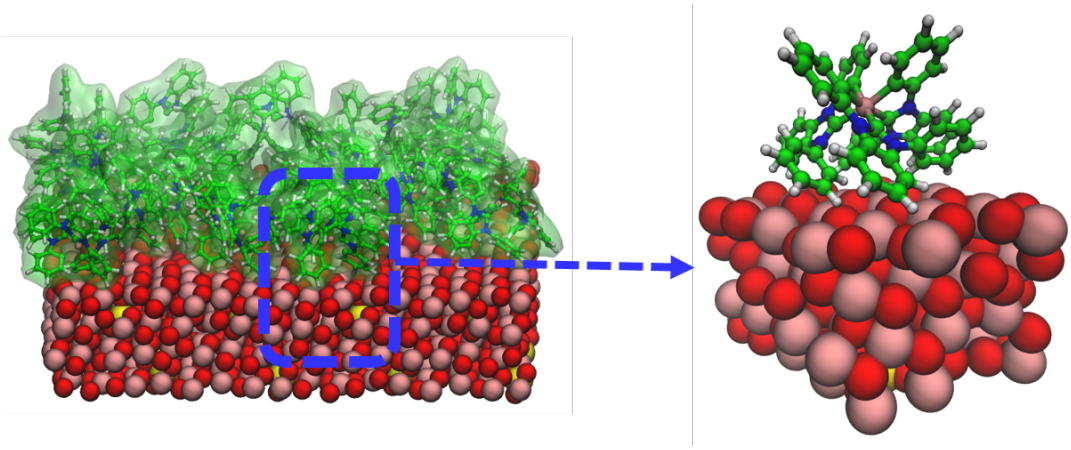

FIGURE 8.9: Representation of the extraction of a DPBIC molecule on a unit cell of ITO slab from the MD simulation box.

8.5 Extraction of representative structures for the evaluation of charge injection rates

From the DPBIC/ITO interface morphology, a set of DPBIC configurations were randomly extracted for the evaluation of charge injection rates. In particular, 100 configurations were considered. This approach allows the evaluation of charge injection rates on realistic DPBIC configurations at the interface, obtained by the relaxation of the molecules on the surface of ITO by MD simulations, and, in turn, to correlate the rates distribution with the distributions of structural parameters, namely DPBIC/ITO distances and orientations. Upon selection of a given DPBIC molecule at the interface, representing a pair of distance/orientation values, a smaller model was defined by centering the simulation box on the center of mass of DPBIC and re-cutting a portion of the underlying ITO slab, using the hexagonal cell parameters of the smaller DFT optimized slab as reference (see Figure 8.9). In particular, the selected ITO portion was fitted onto the DFT optimized structure of the ITO unit cell, obtaining a DPBIC single molecule on the DFT optimized ITO hexagonal unit cell. It is worth recalling that the ITO slab, used in MD simulations for the growth of the organic layer, was built as a supercell of the DFT model, and constant-volume MD equilibrations were only performed, thus keeping the cell parameters unchanged. Consequently, the re-cut operation applied to the MD model leads to a slab with the same periodicity of the initial DFT model.

8.6 Electronic coupling and injection rates

The hole electronic coupling between ITO and DPBIC molecules was evaluated by computing the transfer integral between ITO Bloch states around the Fermi energy and the molecular HOMO state. The contribution of individual transfer integrals V_{ij}, which measures the coupling between each of the electrode levels

and the molecular HOMO level, is renormalized by the electrode density of states (DOS) and assuming Fermi-Dirac distribution of occupancies:

$$J_{ij} = \frac{2\pi}{h}|V_{ij}|^2[1 - f(E_i)]\rho(E_i) \tag{8.1}$$

where V_{ij} is the transfer integral between the metal state i and the molecular state j, *f(Ei)* is the Fermi-Dirac distribution and *ρ(Ei)* is the density of states at the electrode. Transfer integrals were computed at the DFT level on configurations extracted from MD calculations, for isolated DPBIC molecules on the periodic ITO slab, as explained before. DFT transfer integrals calculations were performed by using the Quantum Espresso package[178], applying the PBE functional[209] and MT pseudopotentials[232] on all atoms and a wavefunction cut-off of 80 Ry. Namely, three independent calculations were performed (DPBIC molecule, ITO slab, and DPBIC/ITO) to reconstruct the effective overlap and Hamiltonian matrices. The size of the simulation cell allowed us to compute transfer integrals at the Gamma point only. Within this approximation, charge transfer rates can be computed by the Marcus-Jortner formula:

$$k_{ij} = \frac{2\pi}{h}|V_{ij}|^2\rho(E)\int dE[1 - f(E)]\frac{1}{\sqrt{4\pi kT\lambda}}exp\left[-\frac{(E_{ij} - \lambda - E)^2}{4kT\lambda}\right] \tag{8.2}$$

where λ is the molecular reorganization energy, T is the temperature, k is the Boltzmann constant and E_{ij} is the energy alignment between the Fermi level of the electrode and the molecular HOMO state. The hole reorganization energy (λ) of 68 meV for DPBIC was taken from literature. Calculations were performed at room temperature (T=300 K). In this work, we assumed perfect alignment of the HOMO molecular level with respect to the electrode Fermi level (that is, E_{ij}=0) to maximize the effect of molecular configurations on electronic couplings. For a positive injection barrier, charge transfer rates are essentially renormalized by the exponential term. Contribution of all DPBIC molecules within a distance of 9 Å from the topmost surface atoms of ITO, constituting the first molecular layer in contact with the electrode, was considered.

8.7 Distributions of charge injection rates

For each configuration considered, transfer integrals and injection rates were computed as described above. The resulting distribution of injection rates, as a function of the radial and angular structural parameters, is shown in Figure 8.10. As expected, computed transfer integrals exhibit an exponential decay with the distance between the DPBIC molecule and the ITO surface, which is related to the lowering of electronic overlap. Interestingly, computed values suggest a preferential molecular orientation for injection, with a maximum at around 0° and lower rates at an orientation of 180° for DPBIC with respect to the ITO surface. This picture is compatible with the asymmetry of the HOMO level (Figure 8.8). The overall distribution of injection rates, shown in Figure 8.11, is peaked at slightly larger values for the growth of DPBIC on ITO in

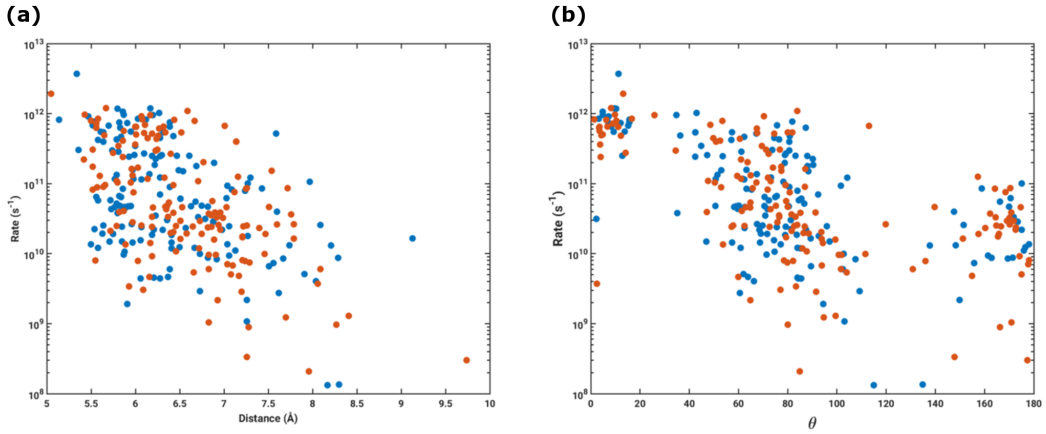

FIGURE 8.10: Variation of the injection rate as a function of the DPBIC/ITO distance (a) and orientation (b) for the kinetic (blue dots) and thermodynamic (red dots) growth modes, respectively.

thermodynamic conditions, as a result of the increased relaxation at the interface. Injection rates range are mostly located in the range from 10^{10} to 10^{12} Hz, in line with rates computed for typical metal-organic systems, considering the weak coupling between DPBIC and ITO. The distribution of injection rates as a function of distance and orientation of DPBIC molecules with respect to the ITO surface (Figure 8.11) suggests preferential configurations for optimal injection. In particular, hole injection is favored at short molecule/surface distances. However, orientation of individual molecules does also play an important role. The largest values of computed injection rates are observed for a DPBIC/ITO distances of about 6 Å with organic molecules at an orientation of about 0° with respect to the surface. The region ranging from 5.5 to 7.5 Å and θ from 40° to 100° is denser respect to the others, because it is the region in which both kinetic and thermodynamic configurations are mostly distributed. However, this region presents slightly lower values of injection rates. There are lower values also in the region at 180° which has the HOMO orbital on the other side respect to the surface. The highest values at 0° suggest that a thermodynamically-driven growth of organic molecules on the surface leads to better injection rates and hence to better performance of devices.

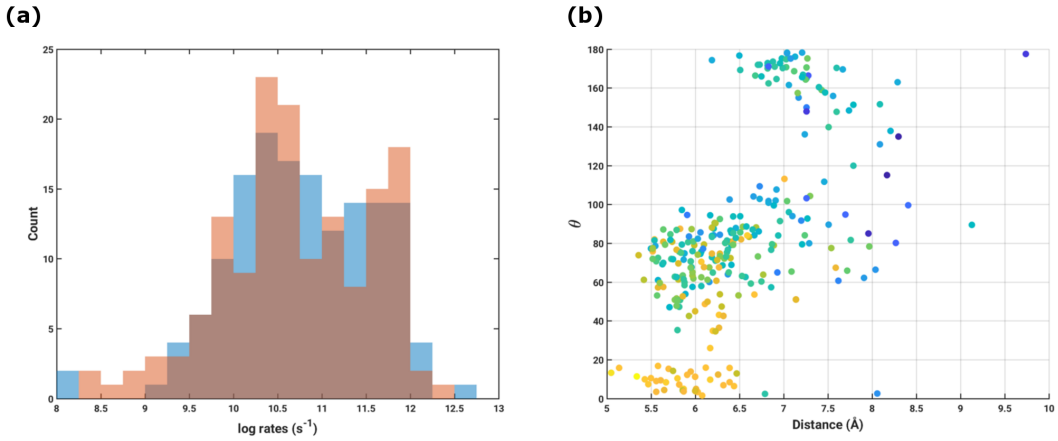

FIGURE 8.11: Distribution of injection rates (a) in kinetic (blue bars) and thermodynamic (red bars) growth conditions and distribution of injection rates (b, log scale) as a function of distance and orientation for the aggregated (kinetic and thermodynamic growth) data.

8.8 Conclusions

In summary, a realistic description of the interface between DPBIC and ITO was modeled, by applying methods based on equilibrium and non-equilibrium MD in different processing conditions. In particular, kinetic and a thermodynamic growth conditions were reproduced, including statistical sampling of interface configurations. The properties at the nanoscale of these interfaces were analysed in terms of suitable structural parameters, such as distance between DPBIC center of mass and ITO surface and orientation of DPBIC with respect to the ITO surface, resulting in distributions of structural parameters. In order to correlate morphology and charge transfer properties at the electrode/organic interface, the structures obtained by atomistic models were extracted for performing electronic properties investigation. From these investigations, in turn, the charge injection rates between ITO and DPBIC were evaluated. The distribution of the charge injection rates indicates the thermodynamic growth conditions as the one showing the highest injection rates values. Moreover, the correlation between distributions of charge injection rates and structural parameters suggests a strong relationship between molecular orientation, related to the symmetry of the HOMO orbital, and the resulting charge transfer properties at interfaces. Namely, the highest values of charge injection rates were computed for molecules at $\theta = 0°$, a value at which the thermodynamic growth distribution of structural properties is peaked. We can then speculate that thermodynamic growth conditions result in the best injection rates between ITO and DPBIC in OLEDs. This approach was also collected in a mulsticale simulation tool, MIRTO, as described in the Appendix A.

Chapter 9

Morphology and electronic properties of phosphorene at the interface with organic materials

Phosphorene is a novel 2D materials which attracted a lot of interest in researchers due to its high conductive properties, which makes it a great candidate for applications as semiconducting material in organic devices, mostly in OFETs [46, 159, 161, 163, 164, 168, 234, 235]. The major issue for the application of phosphorene in organic devices, however, is the low stability in ambient conditions, related to degradation by oxidation of phosphorous atoms of the surface. The occurrence of oxidation processes can partially be circumvented by protecting the phosphorene active layers with an overlying layer of inert materials. A common strategy to phosphorene capping consists in encapsulating the active layer with polymers or metal oxides[159, 164, 170, 171]. Another issue that can potentially alter the properties of phosphorene in devices is related to the interaction at the interface with other materials, which can exhibit a morphology far beyond the ideal planar configuration, thus altering the conformation of the overlying layers. This issue is particularly relevant in FET devices based on phosphorene, where the active layer is in contact with a dielectric material, for example a polymer or metal oxide layer[167, 169–171], to ensure electrical insulation from the gate dielectric. As a result, the intrinsic properties of phosphorene can be modified, with respect to the pristine material, upon adsorption on substrates. In this chapter, the structure, dynamics and the electronic properties of phosphorene monolayers at the interface with organic materials are investigated by a combination of molecular dynamics (MD) and density functional theory (DFT) calculations. All the MD simulations were performed using the LAMMPS package[184], whereas the DFT calculations were performed using the CP2K package[236]. In particular, the effect on the properties of phosphorene induced by overlying aggregates of linear alkanes is also investigated, to assess the possibility of using molecular materials as capping layers in phosphorene devices. In this regard, the morphology of alkane chains at the interface with phosphorene was studied. Namely, the adsorption energy of alkane chains (1 to 10 chains on the surface) on phosphorene was firstly evaluated, by applying a lateral sliding potential energy surface scan, locating the local minima of alkane chains on phosphorene, correlating the potential energy trend with orientation of the molecules on the surface. Furthermore, the aggregation of alkanes with different chain lengths at the interface with phosphorene

was investigated by performing MD simulations. In particular, pentadecane (C15), triacontane (C30) and pentatetracontane (C45) were considered. In addition, the possibility of building a phosphorene-based stacked planar device was evaluated by analysing how the structural, electronic and thermal transport properties of phosphorene would be affected by the interaction with a rough surface, representing a gate dielectric. Namely, the interaction between a phosphorene monolayer and PMMA was investigated by performing MD simulations to study structural modification of phosphorene at the interface with the polymer. Furthermore, DFT calculations were applied to assess the electronic transport properties of phosphorene upon these modifications. In order to understand if the alkane chains can be used as capping layer to protect phosphorene surface by external agents in organic electronic devices, alkane chains were also equilibrated on the phosphorene at the interface with PMMA, thus modelling the dielectric/semiconductor/capping layer interfaces in real devices.

9.1 Phosphorene model

Phosphorene layers were modelled using the interatomic potential described in Ref [124], based on the OPLS-AA force field[226]. The phosphorene structure was obtained from the bulk black phosphorus (BP) unit cell (taken from *American Mineralogist Crystal Structure Database*). The structure of the modeled BP bulk structure was equilibrated by MD simulations. Namely, the structure was equilibrated at 300 K for 1 ns in an NPT ensemble, letting the lattice parameters to relax. Thermal treatments were also performed on the equilibrated bulk structure, performing a 5 ns simulation at 500 K in an NPT ensemble. The stacking structure of the equilibrated bulk BP was AB type (see section 2.12), with a density of 2.73 g/cm^3, in good agreement with reported data (2.69 g/cm^3)[237]. The calculated interlayer distance of 3.04 Å is also in good agreement with the DFT value of 3.21 Å[238]. The BP bulk equilibrated structure is shown in Figure 9.1. From the equilibrated BP bulk structure, the phosphorene monolayer structure was extracted and equilibrated in order to be used in further simulations.

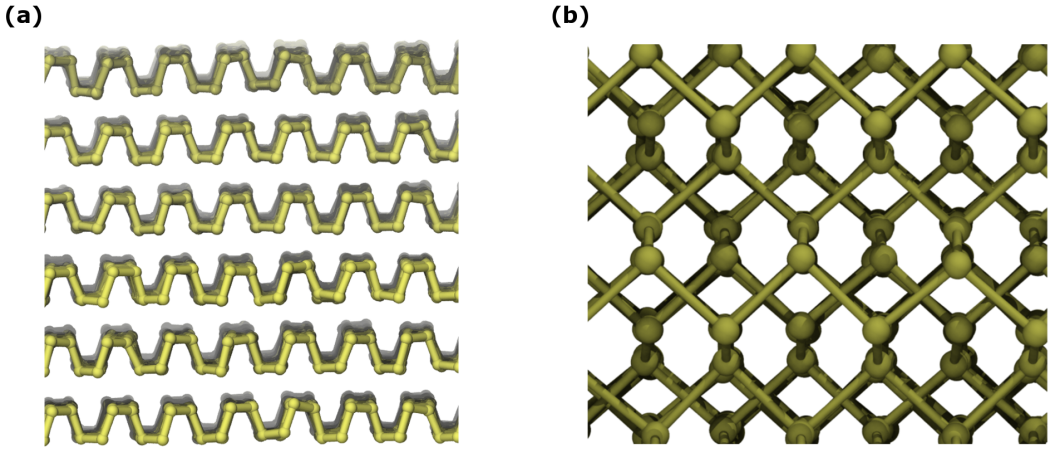

FIGURE 9.1: Side view (a) and top view (b) of the equilibrated structure of black phosphorus.

9.2 Interface between phosphorene and alkanes

To evaluate potential surface protection strategies for phosphorene, a first step is to investigate the interactions between the phosphorene surface and the material used as protection, and, in turn, how these interactions would affect the structural and electronic properties of both the phosphorene and the protective material. The protection layer should consists of an organic material, possibly cheap, inert towards phosphorene and stable in ambient conditions. Furthermore, this organic material should aggregate uniformly and ordered in contact with the phosphorene surface. This would result in a double advantage, i.e. the protection would be more efficient and less material would be needed to cover all the surface. In this regard, alkane chains could be used as protective

material, and it was also found that alkane chains form ordered, uniform aggregates on 2D materials, for example on graphene[135, 136]. To the best of our knowledge, this study constitutes the first attempt to understand the aggregation of alkane chains on the phosphorene surface. To this end, the morphology of alkane chains at the surface of the phosphorene were investigated, by means of MD simulations and molecular mechanics calculations. First, a 12x12 nm model of phosphorene was equilibrated in vacuum at room temperature by MD simulations. Standard OPLS parameters were adopted for alkanes C15, C30 and C45 molecules.

To evaluate the adsorption energy of alkane chains on phosphorene surface, a C30 alkane chain was considered. By performing molecular mechanics calculations, we estimated the optimal distance between alkane chains and phosphorene surface evaluating the adsorption energy at different heights, finding a value of 3.50 Å, in good agreement with previous calculations on similar molecules[136]. Then, we analysed the energetics driving the alignment of the alkane chains on phosphorene. The complexity of the potential energy landscape in a system composed by weakly interacting flexible species hinders the localisation of global minimum configurations using standard optimisation procedures. We then decided to tackle this problem using a two-steps approach. We started overlaying an optimised layer of alkane chains on a rigid optimised phosphorene layer. By varying the mutual orientation and positioning of the rigid layers, we estimate the potential energy landscape of the adsorption process in order to find candidate structures close to the global energy minimum. A full structural relaxation is then performed to compute the global minimum energy of the configurations. The adsorption energy is calculated as:

$$E_{ads} = E_{chains@phosphorene} - E_{chains} - E_{phosphorene}$$

The orientation angle (θ) is an order parameters computed to evaluate the orientation of alkane chains aggregates on the phosphorene surface. It is defined as the angle between the alkane chain backbone and the zigzag (ZZ) direction of phosphorene. The surface potential energy of a single alkane chain on phosphorene was evaluated by computing the potential energy of the alkane chain at different positions on the surface at a fixed θ. These calculations were repeated by changing the θ value, obtaining the most favourable orientations and positions of a single alkane chain on the phosphorene surface (see Figure 9.2a). From these calculations, energy maps representing the surface potential experienced by the alkane chain were obtained (an example of an energy map is reported in Figure 9.2b). After having located the local energy minima, a complete structural relaxation was performed to obtain the global minimum of the single alkane chain, for each θ considered in the potential energy surface calculations. This procedure was also performed for aggregates formed by multiple chains (up to 10 chains per aggregate). Namely, the aggregates were firstly optimised in vacuum and then the potential energy surface was scanned as explained previously. Observing the energy map for a rigid shift of a single C30 chain on the phosphorene surface, the most favourable orientation angle would be 54° whereas the alkane chain oriented along the ZZ direction ($\theta = 0°$) resulted a bit higher in energy. By optimising the system, though, the trend

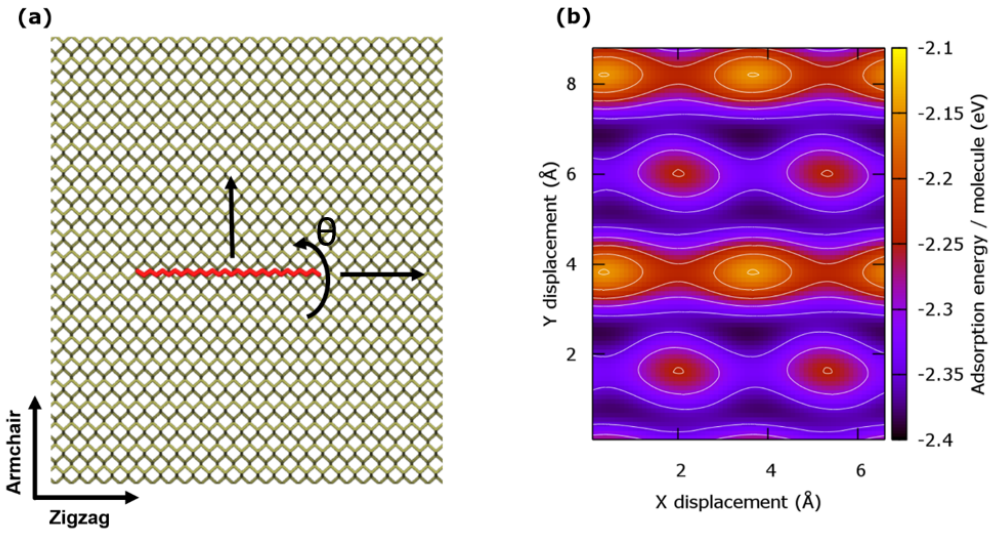

FIGURE 9.2: Representative description of the procedure to evaluate the potential energy surface (a) and the energy map obainted for a single alkane chain on phosphorene at $\theta = 0°$(b).

changes and the $\theta = 0°$ resulted the most favourable orientation (see Figure 9.3). This is ascribable mainly to the tilting of the alkane chain occurring when it interacts with the phosphorene ZZ grooves. The optimised alkane chain oriented along the ZZ direction, indeed, assumed a tilt angle between the alkane chain plane and the posphorene surface of 9° which allows it to maximize the interactions between C and P atoms. By increasing the number of chains in the aggregates examined, the 0° orientation angle confirmed to be the most favourable, with a lowering in potential energy per molecule due to the lateral alkane-alkane interactions (see Figure 9.3), with an E_{ads}=3.55 eV per molecule for 10 C30 chains. The calculated equilibrium lateral distance between alkane chains, 4.39 Å, almost coincides with the phosphorene lattice constant (4.38 Å). This may be another reason for the arrangement of the alkane chains along the ZZ direction. In fact, due to this orientation, the alkane chains are always located in their local minima, while this is not the case in other orientations.

In order to validate the results obtained by the adsorption energy evaluation, MD simulations of alkane chains equilibrated on the phosphorene surface were carried out. Namely, C15, C30 and C45 alkane chains were equilibrated on a phosphorene 12x12 nm bilayer. One layer of phosphorene was maintained fixed during all the simulations, while the layer above it was unbiased. This was done to simulate other layers of a device underneath the phosphorene monolayer. In order to mimic the experimental process related to the aggregation of alkane chains on a surface, similar to the procedure developed for other interface models (MIRTO, see Appendix A), each alkane molecules was firstly positioned above the phosphorene surface, at a distance of 50 Å along z, with random rotation and initial position on the xy axis. An initial velocity component toward phosphorene, ranging from 5 to 6 Å/ps, was assigned to the

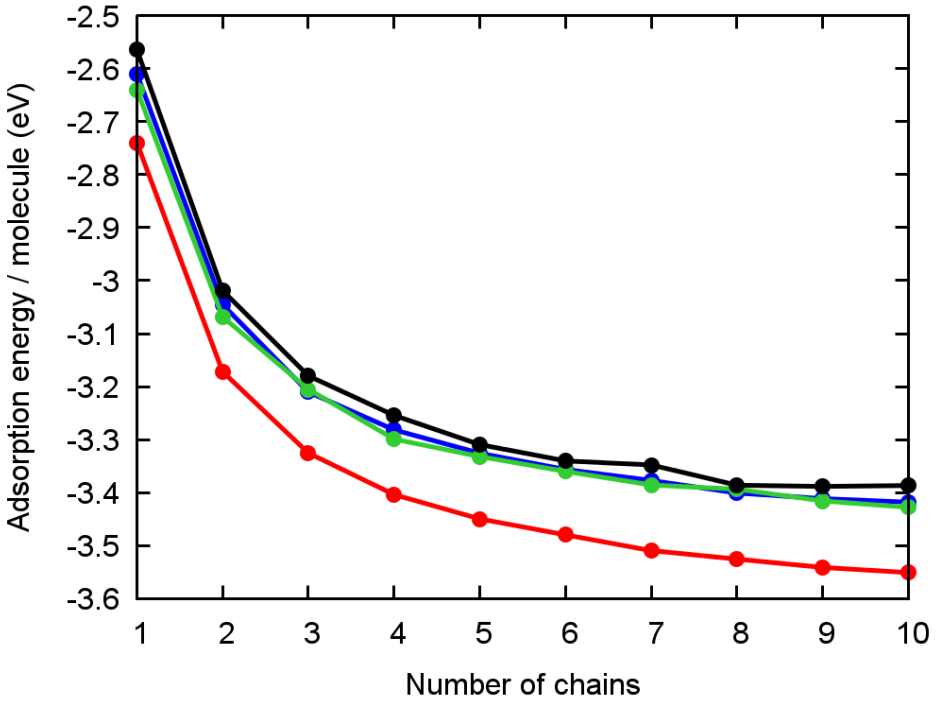

FIGURE 9.3: Optimised energies of alkane chains at $\theta = 0°$(red), $\theta = 20°$(blue), $\theta = 50°$(green), $\theta = 90°$(black).

molecule. This procedure was repeated for each molecule inserted, until a complete coverage of the phosphorene surface was obtained. For each new molecule, an MD simulation at 300 K for 50 ps in an NVT ensemble was performed, in order to obtain a n initially disordered aggregation of alkanes on phosphorene. The system was then propagated in an NVT ensemble for 20 ns at 300 K. Alternatively, to simulate the experimental procedure, an annealing at 400 K for 10 ns followed by cooling and equilibration at 300 K for 10 ns was performed. In Figure 9.4, the final structures of C15,C30 and C45 alkanes on phosphorene after the initial deposition, equilibration and annealing, are represented, together with their θ histograms. The aggregation of the alkane chains immediately after the deposition on the surface appeared disordered, with some chains forming small oriented clusters (moslty in the case of C15 chains), but without a clear preferential orientation. The more the alkane chain is long, the more disordered appeared to be the aggregation (see Figure 9.4a, 9.4b and 9.4c). By equilibrating the systems at 300 K, the alkane chains diffuse over the surface, clustering in more ordered aggregates, with a clear propensity to the orientation along the ZZ direction ($\theta = 0°$) of phosphorene. In particular, as shown in Figure 9.4d, almost every C15 alkane chain aggregates along the ZZ direction, while C30 presents two orientations, $\theta = 0°$ and $\theta \approx 55°$(see Figure 9.4e). C45 chains orient along the ZZ direction, with some amorphous aggregates, due to the length of the chains (see Figure 9.4f). By applying thermal treatments, C30 and C45 alkane chains arrange with almost every chain oriented along the ZZ direction (see Figure 9.4h and 9.4i), validating the results obtained by the adsorpion energy evaluation. This result is evident by observing the θ histograms

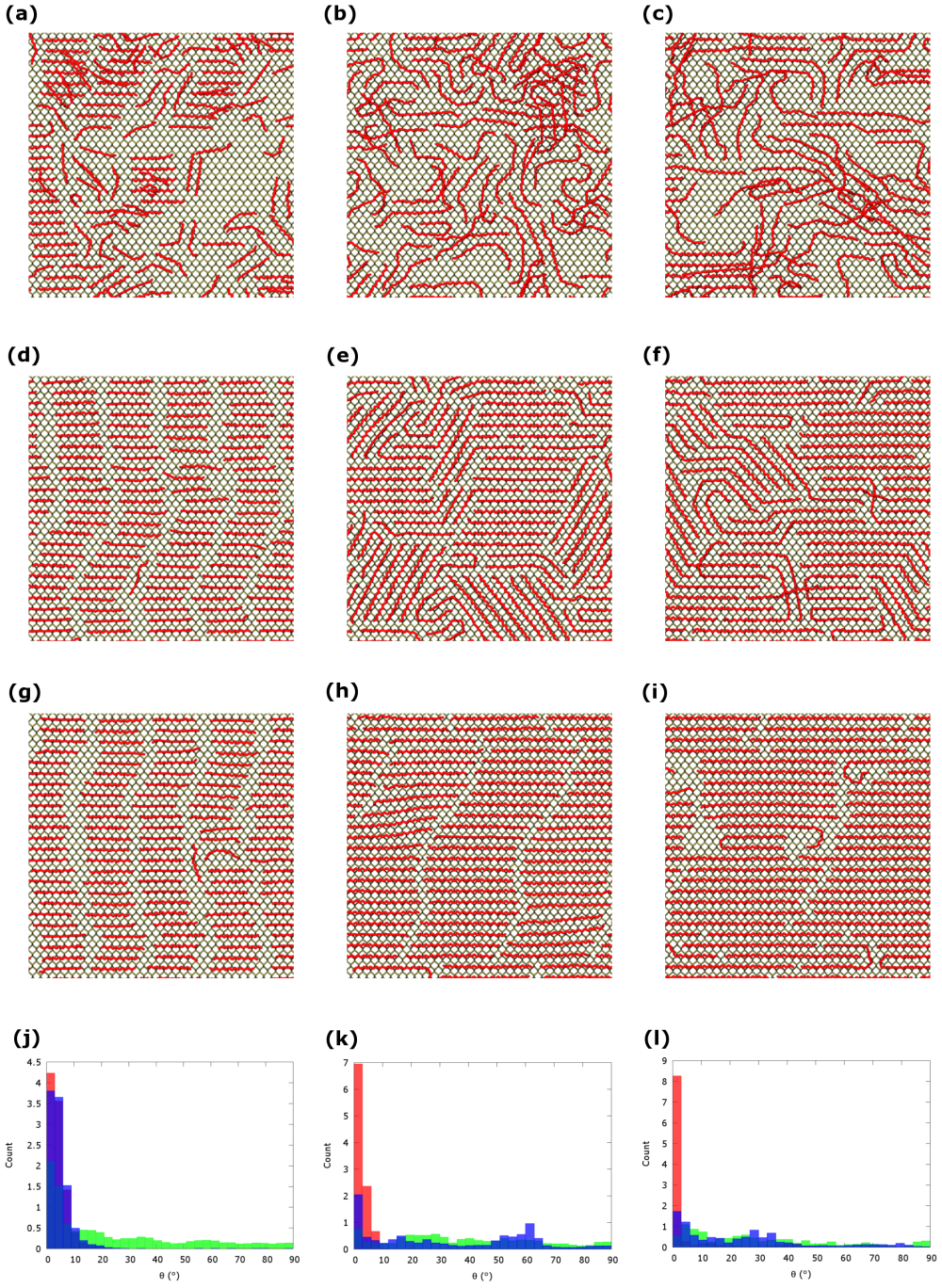

FIGURE 9.4: Final structures of C15 (left panels),C30 (middle panels) and C45 alkanes 8right panels) after deposition (a,b and c), after equilibration at 300 K (d,e and f), and after application of annealing at 400 K (g,h and i). C atoms of alkane chains are represented in red. Hydrogens are not shown for the sake of clarity. Histograms of θ after deposition (green), equilibration at 300 K (blue) and annealing at 400 K (red) are reported for C15 (j), C30 (k) and C45 (l).

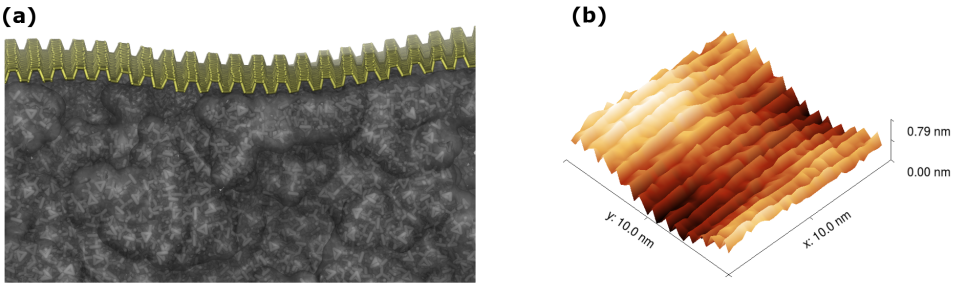

FIGURE 9.5: Phosphorene equilibrated on the PMMA surface (a) and simulated surface profile of the phosphorene layer (b).

(see Figure 9.4k and 9.4l).

These results confirmed the anisotropic properties of the phosphorene surface. Moreover, the alkane chains aggregated in a uniform ordered morphology, important property for the application as protective layer. The thermal treatments were found to be crucial in order to obtain the better aggregation of alkane chains at the interface. This is an important aspect that should also be taken into account in experiments.

9.3 Morphology and electronic properties of phosphorene at the interface with PMMA

Another important interface for phosphorene to be used as organic semiconductor layer in electronic devices is with the dielectric layer. The interaction with a polymeric organic material, for example, could affect the structure and hence the electronic properties of phosphorene, leading to the degradation of performance in devices. In this regard, a detailed atomistic model of the process occurring at the interface between phosphorene and the gate dielectric layer could highlight how this interaction would affect the structural and electronic properties of phosphorene in organic devices. In this work, the interface between phosphorene and PMMA (see section 2.12, was investigated by performing MD simulations and DFT calculations. In particular, MD simulations were carried out to understand how the interaction with a rough surface would change the structural properties of phosphorene. The morphology obtained by MD simulations has been used, in turn, to evaluate how this interaction affect the electronic properties, by performing DFT calculations. The 10x10 nm PMMA model used in this Chapter was obtained in a previous work[126]. A 10x10 nm equilibrated phosphorene monolayer was inserted at 10 Å distance from the PMMA surface along the z non-periodic direction and equilibrated at room temperature for 10 ns in the NVT ensemble. Electrostatic interactions were treated by the particle-particle particle-mesh (pppm) method and a cut-off of 10.0 Å were used for both Coulomb and van der Waals interactions. The Nose-Hoover thermostat[185, 186] was used for simulations in the canonical ensemble (NVT) with time constant of 0.1 ps and timestep of 1.0 fs. As shown in Figure 9.5, phosphorene monolayer adheres and adapt very well on the PMMA

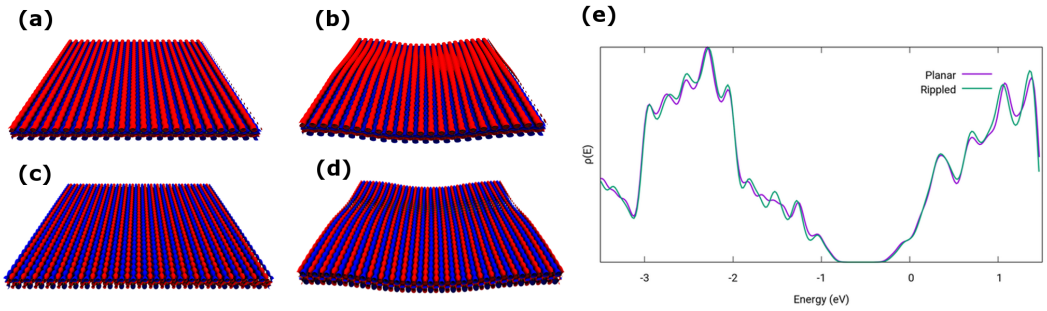

FIGURE 9.6: Topology of HOMO and LUMO of the ideal case (a and c) and the distorted (b and d) together with density of states plot (e).

surface, losing its perfect planarity, especially along the armchair direction, but maintaining an overall stable structure. The structural properties of the phosphorene layer upon equilibration on the PMMA surface were then evaluated by simulating a surface profile (see Figure 9.3), by which we extracted the average rms roughness (0.17 nm) and the rms roughness over the armchair (0.065 nm) and zigzag (0.025 nm) components. The average surface rms roughness resulted much smaller than in the rough substrate, meaning that the phosphorene does not follow completely the surface topography of PMMA, in fact maintaining a stable structure at the interface with the polymer. Moreover, the rms components showed more propensity for the armchair direction to bend, adapting to the underlying substrate, whereas the zigzag appeared more rigid. The structure of phosphorene at the interface with PMMA, obtained by MD simulations, was then extracted to evaluate how the structural distortions affects the electronic properties. Namely, large-scale DFT calculations were carried out on the phosphorene layer, composed of 2668 atoms, for both planar and distorted structures. This calculations were performed at the gradient-corrected level by applying the PBE[209] exchange-correlation functional within the GPW approach[239, 240] as implemented in the CP2K program package[236]. Electronic states were expanded by a double-ζ plus polarisation basis set (DZVP)[241] with norm-conserving pseudo-potentials for the description of core levels and a plane-wave representation of the charge density[242–244] with a cut-off of 300 Ry. The HOMO and LUMO topologies (see Figure 9.6) did not presented substantial modifications between ideal and distorted structure of phosphorene. Furthermore, the density of the states plot (see Figure 9.6e) showed very similar features for both cases, in the region around band gap, with very few differences at higher and lower energies. Given this similarity, we can assume that the electronic properties of phosphorene are essentially not affected by the interaction with the PMMA rough surface.

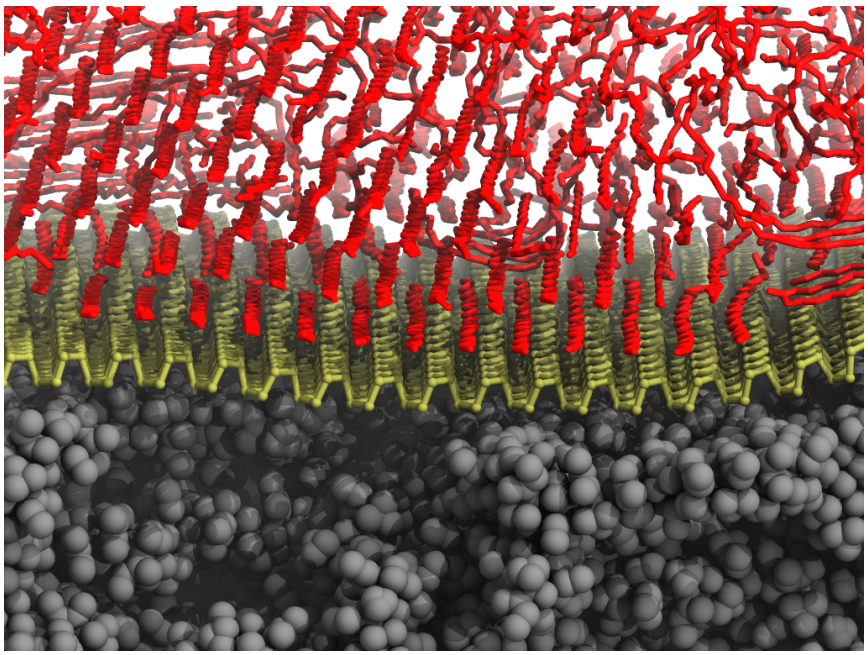

FIGURE 9.7: Alkane chains (in red) equilibrated on phosphorene on top of a PMMA slab.

9.4 Phosphorene at the interface between PMMA and alkanes

To simulate interfaces in the real systems, we considered alkane chains as protective layers of phosphorene at the interface with PMMA, investigating if the distortion of the phosphorene upon interaction with a rough surface would affect the aggregation of the alkane chains. In a first set of simulations, 66 C24 alkanes were equilibrated on the surface of phosphorene on PMMA, observing the same features of the interface morphology of alkanes on phosphorene. In another set of simulations, 500 C24 alkane chains were deposited, one-by-one at room temperature, on the phosphorene surface at the interface with the PMMA obtained previously. The system was then equilibrated for 10 ns at 300 K, allowing the alkane chains to relax on the phosphorene surface. The equilibrated structure of this interface is represented in Figure 9.7. The first layers of alkanes at the interface with phosphorene exhibit aggregation along the ZZ direction, with the presence of amorphous clusters in the layers above the first ones. This result demonstrates that even at high coverage the features of the interface morphology between alkanes and phosphorene are maintained.

9.5 Conclusions

The structural, dynamics and electronic properties of phosphorene at the interface with other organic materials were investigated by performing MD, DFT and molecular mechanics calculations. In particular, to evaluate the use of alkane chains as a protective material for phosphorene, the aggregation of alkanes on phosphorene was investigated. By MD simulations, we observed a uniform, ordered aggregation of alkane chains on the phosphorene surface along one preferential direction (the ZZ direction), creating an almost complete coverage of the surface, which improves upon application of thermal treatments. The interface of phosphorene with PMMA was simulated in order to investigate the modifications of the structural and electronic properties of phosphorene upon interaction with the rough surface of a polymer. From MD simualtions performed on this system, we found that the structure of phosphorene were distorted but not significantly altered, as also observed by simulating a surface profile. Furthermore, the comparison between the electronic properties of phosphorene at the interface with PMMA with the pristine case shows that the interaction with the polymeric surface does not affects the electronic properties. Finally, in view of device applications, alkanes were probed as capping layer for phosphorene at the interface with PMMA. MD results indicated the formation of ordered layers of alkane chains at the interface, confirming the possible application of these molecules as a protective material for device applications. Experiments are being carried out to validate the results obtained with our simulations, addressing the possibility of using alkane chains as a capping layer for phosphorene.

Chapter 10

Conclusions and outlook

In this thesis, the morphology and the electronic properties of materials and interfaces of relevance in organic electronics and optoelectronics devices were investigated by advanced modelling tools. In organic devices based on thin films, the morphology of interfaces between layers is of paramount important, influencing the overall performance of devices. A detailed knowledge on the processes occurring in materials at the interfaces enable the optimization of organic materials and the development of novel fabrication process leading to devices with enhanced performance. In a multiscale approach, the aim of the thesis was to develop computational tools able to investigate the nanoscale morphology of materials at the interfaces, further correlating the morphology obtained with electronic processes in materials, including charge transport. The length and time scale of involved phenomena require the application of a set of computational tools, ranging from the atomistic simulations of electronic properties to device-scale modelling in which the molecular information are mandatory in order to understand the phenomena occurring at higher scales. In this respect, HPC enabled us to access information at different scales with unprecedented possibilities, widening the typical domain of different simulation techniques.

A wide range of organic and inorganic materials was investigated, comprising small molecules, polymers, metal oxides and 2D materials. In particular, the morphology, stability and charge transport properties of 2D and 3D phases of PTCDI-C13 were studied by performing MD and DFT calculations, and the information obtained were used to develop a coarse-grain model of the organic semiconducting material. Furthermore, the morphology of PTCDI-C13 aggregates at the interface with a polymer dielectric layer, PMMA, and a 2D material, graphene, used in organic electronics was studied, mimicking realistic fabrication and processing conditions. Moreover, the hybrid interface between a layer of organic small molecules, DPBIC, and a doped metal oxide, ITO, representing the hole transport layer and the anode in a OLED, respectively, was simulated, and the interfacial structures were used to compute charge injection rates at the interface. The relationship between structural and electronic properties at the interface was then assessed by correlating nanoscale morphology with charge injection rates. Finally, the structure, dynamics and electronic properties of phosphorene (a 2D inorganic semiconductor), at the interface with organic materials, namely alkanes and PMMA, were investigated by a combination of MD and DFT calculations.

The computational tools developed in this thesis have been integrated in a

computational tool (MIRTO, Modeler of Interfaces and charge injection RaTes calculatOr, see Appendix A) for the simulation of realistic morphologies of materials at the interfaces, extracting structural and injection properties. This tool was implemented in the software VOTCA[245].

This thesis outlined a first step towards a comprehensive understanding of materials properties at the interfaces, in order to make use of these computational tools for the investigation of new frontiers of organic electronics, especially in the field of unconventional devices, such as large-area lighting, automotive, wearable electronics, bioelectronics. This latter, in particular, is an emerging field for addressing the challenges related to health. Progress in the modelling of organic electronic materials and devices at the interface with complex environments is expected to define new prospects for the development of next-generation multifunctional devices for technological applications.

Appendix A

Development of the computational tool MIRTO: Modeler of Interfaces and chaRge injection raTes calculatOr

The modelling of the morphology and charge injection rates at the interface between DPBIC and ITO (see Chapter 8), led to the development of a multiscale computational tool, called MIRTO (Modeler of Interfaces and chaRge injection raTes calculatOr). This tool is able to model the interface between two materials, organic or inorganic, by performing advanced non-equilibrium and equilibrium MD simulations, in order to obtain the morphology of a material grown on a surface. Furthermore, the same tool extracts the morphology of the interface and calculates suitable structural parameters, providing the statistical distributions. Moreover, the morphology obtained by MD is used to investigate the electronic properties by performing DFT calculations. From these calculations, the tool computes the charge injection rates between the two materials at the interface, with their distributions. In particular, the tool correlates the rates distributions with structural parameters previously calculated, directly comparing the electronic and structural properties of the interface, and therefore obtain a structure/properties relationship. The tool was firstly tested on the case study of DPBIC on ITO, though it can in principle be used for the modelling of other materials for organic electronic applications. Moreover, MIRTO is being implemented in the open-source software suite VOTCA (Versatile Object-oriented Toolkit for Coarse-graining Applications)[245]. MIRTO was firstly based on shell (bash), Fortran90, C and python scripts. The scripts were then parsed in python for the implementation in VOTCA. In this appendix, only scripts of the first version will be treated.

Modelling of heterointerfaces

The script *deposition* allows the user to obtain realistic morphologies of heterointerfaces starting from a surface and a single molecule. To this aim, the script needs the structures of the surface and the molecule, together with their force field and topology files (the cell parameters will be that of the surface structure file). The user will then decide how many molecules will be deposited on the surface and with which growth mechanism (kinetic or thermodynamic). With these inputs, the script will firstly compute the system parameters (number of atoms of the surface and the molecule, cell parameters and highest atoms of the surface in the box). The deposition of the molecules on the surface can now begin. To do so, the first molecule is randomly rotated and inserted in the simulation box with random initial position on x and y axis, and with a defined distance along z axis. Moreover, an initial velocity toward the surface (-z direction) will be assigned to the inserted molecule. The script will then run the deposition simulation applying the relaxation method chosen by the user. This deposition process will be repeated until the target number of molecules (decided by the user) is obtained. Once the target number of molecules are being obtained, the script will store the final morphology for further investigation.

```
deposition routine

read surface structure
read molecule structure
initialize parameters
insert the number of molecules to deposit
read n
define the growth condition (kinetic or thermodynamic)

for i=0,n do
    insert new molecule in the simulation box
    initialize velocities
    start deposition
done

save morphology
```

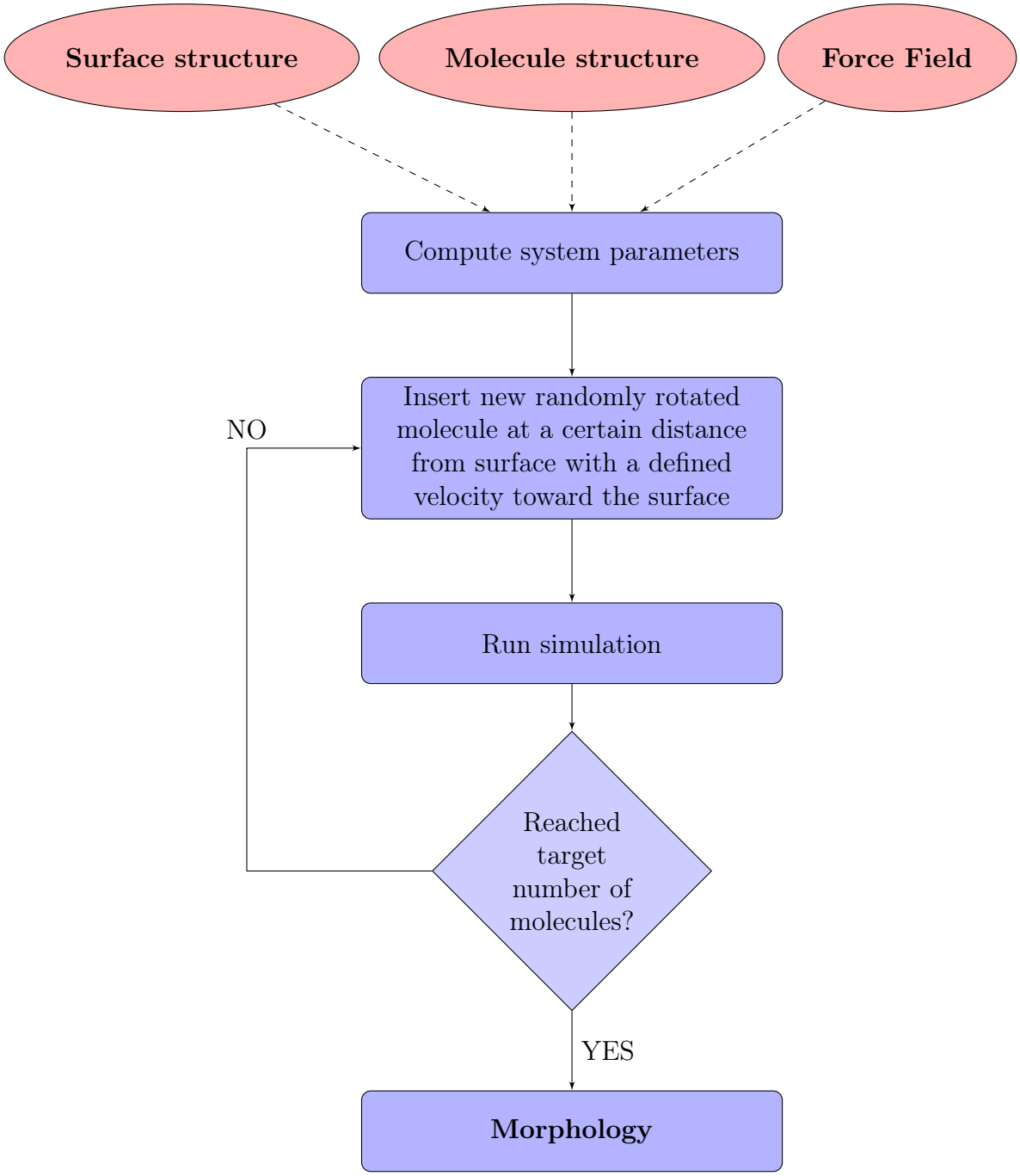
Surface structure
Molecule structure
Force Field
Compute system parameters
Insert new randomly rotated molecule at a certain distance from surface with a defined velocity toward the surface
NO
Run simulation
Reached target number of molecules?
YES
Morphology

Assessment of structural and electronic properties

Structural parameters

The script *postprocessing* will take in input the morphology obtained by the script *deposition* to investigate structural and electronic properties at the interface. In particular, the script will firstly extract the morphology of the interface and compute structural properties of the molecules at the interface with the surface, such as orientation of molecules with respect to the surface, the distance between molecules and surface, and the radial pair distribution function (g(r)) between molecules. The script will then collect these parameters in the form of distributions.

```
postprocessing routine

read morphology
extract interface morphology

compute orientations
compute distances
compute g(r)

print orientations histogram
print distances histograms
print g(r) plot
```

Electronic properties

In order to obtain structures on which electronic properties will be evaluated, the script will also extract the single molecules at the interface with a small portion of the surface. These structures will be used by the script *rundft* for performing DFT calculations. These calculations will provide electronic information that will be used to compute charge injection rates.

```
rundft routine

read interface morphology
extract single molecule on surface

compute electronic properties
```

Charge injection rates

Finally, the script *computerates* will compute charge injection rates from these DFT calculations. Structure/properties relationship will be assessed by associating these charge injection rates with structural parameters previously calculated. These distributions, in turn, can be used in a large KMC model able to investigate for example the degradation of materials at the interface.

```
computerates routine

read electronic properties

compute injection rates

print injection rates distributions

correlate injection rates distributions with structural distributions

print structural/injection distributions
```

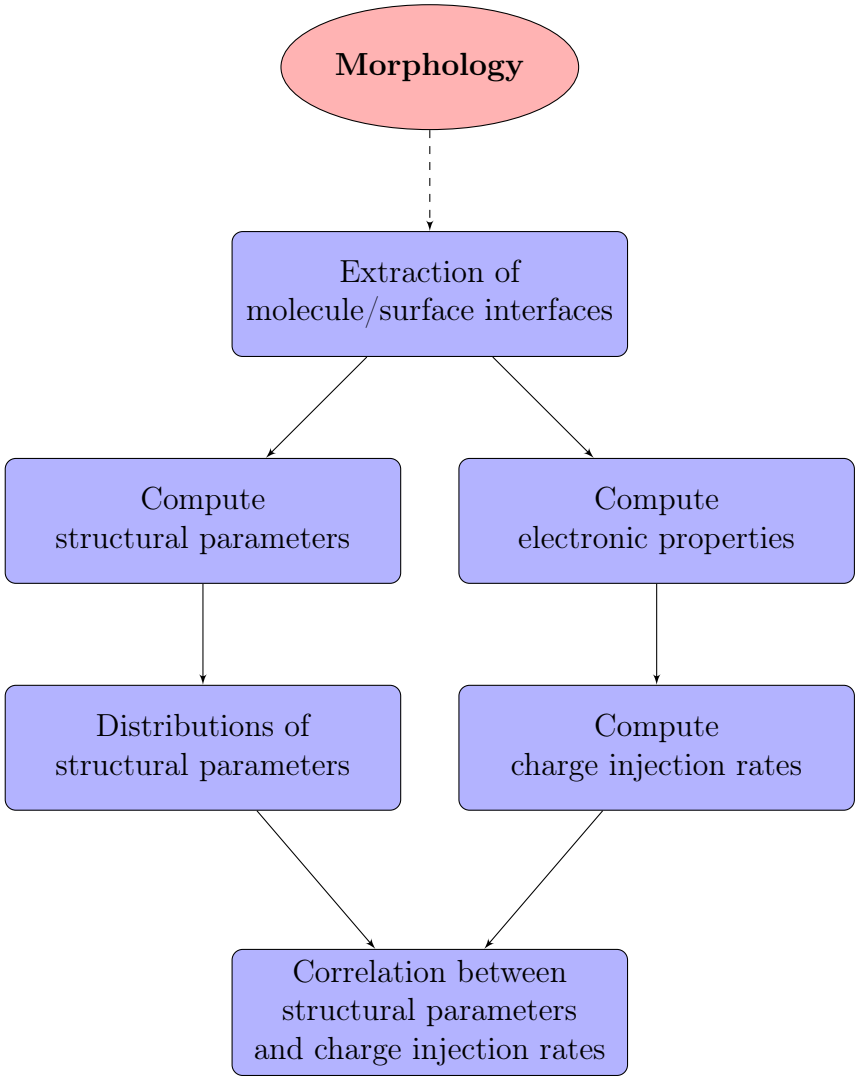
Morphology
Extraction of molecule/surface interfaces
Compute structural parameters
Compute electronic properties
Distributions of structural parameters
Compute charge injection rates
Correlation between structural parameters and charge injection rates

Bibliography

(1) Shirakawa, H.; Louis, E. J.; MacDiarmid, A. G.; Chiang, C. K.; Heeger, A. J. *Journal of the Chemical Society, Chemical Communications* **1977**, 578.

(2) Tang, C. W.; Vanslyke, S. A. *Applied Physics Letters* **1987**, *51*, 913–915.

(3) Koezuka, H.; Tsumura, A.; Ando, T. *Synthetic Metals* **1987**, *18*, 699–704.

(4) Stolz, S.; Zhang, Y.; Lemmer, U.; Hernandez-Sosa, G.; Aziz, H. *ACS Applied Materials & Interfaces* **2017**, *9*, 2776–2785.

(5) Vasseur, K.; Rolin, C.; Vandezande, S.; Temst, K.; Froyen, L.; Heremans, P. *Journal of Physical Chemistry C* **2010**, *114*, 2730–2737.

(6) Virkar, A. A.; Mannsfeld, S.; Bao, Z.; Stingelin, N. *Advanced Materials* **2010**, *22*, 3857–3875.

(7) Jang, J.; Nam, S.; Chung, D. S.; Kim, S. H.; Yun, W. M.; Park, C. E. *Advanced Functional Materials* **2010**, *20*, 2611–2618.

(8) Bolognesi, M.; Prosa, M.; Tessarolo, M.; Donati, G.; Toffanin, S.; Muccini, M.; Seri, M. *Solar Energy Materials and Solar Cells* **2016**, *155*, 436–445.

(9) Wang, C.; Dong, H.; Hu, W.; Liu, Y.; Zhu, D. *Chemical Reviews* **2012**, *112*, 2208–2267.

(10) Facchetti, A.; Yoon, M.-H.; Marks, T. J. *Advanced Materials* **2005**, *17*, 1705–1725.

(11) Facchetti, A. *Materials Today* **2007**, *10*, 28–37.

(12) Muccini, M. *Nature Materials* **2006**, *5*, 605–613.

(13) Someya, T.; Bao, Z.; Malliaras, G. G. *Nature* **2016**, *540*, 379–385.

(14) Zang, Y.; Zhang, F.; Di, C.-a.; Zhu, D. *Mater. Horiz.* **2015**, *2*, 140–156.

(15) Berggren, M.; Richter-Dahlfors, A. *Advanced Materials* **2007**, *19*, 3201–3213.

(16) Kelley, T. W.; Baude, P. F.; Gerlach, C.; Ender, D. E.; Muyres, D.; Haase, M. A.; Vogel, D. E.; Theiss, S. D. *Chemistry of Materials* **2004**, *16*, 4413–4422.

(17) Patel, S.; Park, H.; Bonato, P.; Chan, L.; Rodgers, M. *Journal of NeuroEngineering and Rehabilitation* **2012**, *9*, 21.

(18) Woon Park, J, *Largearea OLED lighting panels and their applications*; Woodhead Publishing Limited: 2013, 572608e.

(19) Malliaras, G.; Abidian, M. R. *Advanced Materials* **2015**, *27*, 7492.

(20) Sirringhaus, H. *Advanced Materials* **2014**, *26*, 1319–1335.

(21) Melzer, C.; Von Seggern, H. *Nature Materials* **2010**, *9*, 470–472.

(22) Newman, C. R.; Frisbie, C. D.; Da Silva Filho, D. A.; Brédas, J. L.; Ewbank, P. C.; Mann, K. R. *Chemistry of Materials* **2004**, *16*, 4436–4451.

(23) Scholz, S.; Kondakov, D.; Lüssem, B.; Leo, K. Degradation mechanisms and reactions in organic light-emitting devices., 2015.

(24) Jeong, Y. J.; Jang, J.; Nam, S.; Kim, K.; Kim, L. H.; Park, S.; An, T. K.; Park, C. E. *ACS Applied Materials and Interfaces* **2014**, *6*, 6816–6824.

(25) Tatemichi, S.; Ichikawa, M.; Koyama, T.; Taniguchi, Y. *Applied Physics Letters* **2006**, *89*, 112108.

(26) Gbabode, G.; Dohr, M.; Niebel, C.; Balandier, J. Y.; Ruzié, C.; Négrier, P.; Mondieig, D.; Geerts, Y. H.; Resel, R.; Sferrazza, M. *ACS Applied Materials and Interfaces* **2014**, *6*, 13413–13421.

(27) Maini, L.; Gallino, F.; Zambianchi, M.; Durso, M.; Gazzano, M.; Rubini, K.; Gentili, D.; Manet, I.; Muccini, M.; Toffanin, S.; Cavallini, M.; Melucci, M. *Chemical Communications* **2015**, *51*, 2033–2035.

(28) Diao, Y.; Lenn, K. M.; Lee, W.-y.; Blood-forsythe, M. A.; Xu, J.; Mao, Y.; Kim, Y.; Reinspach, J. A.; Park, S.; Xue, G.; Clancy, P. *Journal of American Chemical Society* **2014**, *136*, 17046–17057.

(29) Don Park, Y.; Lim, J. A.; Lee, H. S.; Cho, K. *Materials Today* **2007**, *10*, 46–54.

(30) Frank, C.; Novák, J.; Banerjee, R.; Gerlach, A.; Schreiber, F.; Vorobiev, A.; Kowarik, S. *Physical Review B - Condensed Matter and Materials Physics* **2014**, *90*, 045410.

(31) Liscio, F.; Milita, S.; Albonetti, C.; D'Angelo, P.; Guagliardi, A.; Masciocchi, N.; Della Valle, R. G.; Venuti, E.; Brillante, A.; Biscarini, F. *Advanced Functional Materials* **2012**, *22*, 943–953.

(32) Hiroshiba, N.; Hill, J. P.; Hayakawa, R.; Ariga, K.; Matsuishi, K.; Wakayama, Y. *Thin Solid Films* **2014**, *554*, 74–77.

(33) Krauss, T. N.; Barrena, E.; De OteyzaDimas, G.; Zhang, X. N.; Major, J.; Dehm, V.; Würthner, F.; Dosch, H. *Journal of Physical Chemistry C* **2009**, *113*, 4502–4506.

(34) Perez-Rodriguez, A.; Barrena, E.; Fernández, A.; Gnecco, E.; Ocal, C. *Nanoscale* **2017**, *9*, 5589–5596.

(35) Lorenzoni, A.; Gallino, F.; Muccini, M.; Mercuri, F. *RSC Adv.* **2016**, *6*, 40724–40730.

(36) Lorenzoni, A.; Muccini, M.; Mercuri, F. *Journal of Physical Chemistry C* **2017**, *121*, 21857–21864.

(37) Shan, B.; Miao, Q. *Tetrahedron Letters* **2017**, *58*, 1903–1911.

(38) Beaujuge, P. M.; Fréchet, J. M. J. *Journal of the American Chemical Society* **2011**, *133*, 20009–20029.

(39) Bendikov, M.; Wudl, F.; Perepichka, D. F. *Chemical Reviews* **2004**, *104*, 4891–4945.

(40) Anthony, J. E. *Chemical Reviews* **2006**, *106*, 5028–5048.

(41) Iino, H.; Usui, T.; Hanna, J.-i. *Nature Communications* **2015**, *6*, 6828.

(42) Gasparini, N.; Lucera, L.; Salvador, M.; Prosa, M.; Spyropoulos, G. D.; Kubis, P.; Egelhaaf, H.-J.; Brabec, C. J.; Ameri, T. *Energy Environ. Sci.* **2017**, *10*, 885–892.

(43) Gedefaw, D.; Prosa, M.; Bolognesi, M.; Seri, M.; Andersson, M. R. *Advanced Energy Materials* **2017**, *7*, 1–38.

(44) Prosa, M.; Sagnella, A.; Posati, T.; Tessarolo, M.; Bolognesi, M.; Cavallini, S.; Toffanin, S.; Benfenati, V.; Seri, M.; Ruani, G.; Muccini, M.; Zamboni, R. *RSC Adv.* **2014**, *4*, 44815–44822.

(45) Ho, S.; Chen, Y.; Liu, S.; Peng, C.; Zhao, D.; So, F. *Advanced Materials Interfaces* **2016**, *3*, 1–6.

(46) Viani, L.; Risko, C.; Toney, M. F.; Breiby, D. W.; Brédas, J. L. *ACS Nano* **2014**, *8*, 690–700.

(47) Zhan, C.; Yu, G.; Lu, Y.; Wang, L.; Wujcik, E.; Wei, S. *J. Mater. Chem. C* **2017**, *5*, 1569–1585.

(48) Wu, Q. H. *Critical Reviews in Solid State and Materials Sciences* **2013**, *38*, 318–352.

(49) Xu, T.; Zhou, J. G.; Huang, C. C.; Zhang, L.; Fung, M. K.; Murtaza, I.; Meng, H.; Liao, L. S. *ACS Applied Materials and Interfaces* **2017**, *9*, 10955–10962.

(50) Hanson, E. L.; Guo, J.; Koch, N.; Schwartz, J.; Bernasek, S. L. *Journal of the American Chemical Society* **2005**, *127*, 10058–10062.

(51) Fung, M.-K.; Li, Y.-Q.; Liao, L.-S. *Advanced Materials* **2016**, *28*, 10381–10408.

(52) Bobbert, P.; Coehoorn, R. *Europhysics News* **2013**, *44*, 21–25.

(53) Smith, A. R.; Ruggles, J. L.; Cavaye, H.; Shaw, P. E.; Darwish, T. A.; James, M.; Gentle, I. R.; Burn, P. L. *Advanced Functional Materials* **2011**, *21*, 2225–2231.

(54) Hershey, K. W.; Suddard-Bangsund, J.; Qian, G.; Holmes, R. J. *Applied Physics Letters* **2017**, *111*, 113301.

(55) Coehoorn, R.; Van Eersel, H.; Bobbert, P. A.; Janssen, R. A. *Advanced Functional Materials* **2015**, *25*, 2024–2037.

(56) Mesta, M.; Carvelli, M.; De Vries, R. J.; Van Eersel, H.; Van Der Holst, J. J.; Schober, M.; Furno, M.; Lüssem, B.; Leo, K.; Loebl, P.; Coehoorn, R.; Bobbert, P. A. *Nature Materials* **2013**, *12*, 652–658.

(57) Kordt, P.; Van Der Holst, J. J. M.; Al Helwi, M.; Kowalsky, W.; May, F.; Badinski, A.; Lennartz, C.; Andrienko, D. *Adv. Funct. Mater.* **2015**, *25*, 1955–1971.

(58) Petit, M.; Hayakawa, R.; Wakayama, Y.; Chikyow, T. *Journal of Physical Chemistry C* **2007**, *111*, 12747–12751.

(59) Jeon, H. G.; Hattori, J.; Kato, S.; Oguma, N.; Hirata, N.; Taniguchi, Y.; Ichikawa, M. *Journal of Applied Physics* **2010**, *108*, 124512.

(60) Kish, E. R.; Nahm, R. K.; Woll, A. R.; Engstrom, J. R. *Journal of Physical Chemistry C* **2016**, *120*, 6165–6179.

(61) Sirringhaus, H. *Advanced Materials* **2005**, *17*, 2411–2425.

(62) Oh, J. H.; Sun, Y. S.; Schmidt, R.; Toney, M. F.; Nordlund, D.; Könemann, M.; Würthner, F.; Bao, Z. *Chemistry of Materials* **2009**, *21*, 5508–5518.

(63) Jang, M.; Baek, K. Y.; Yang, H. *Journal of Physical Chemistry C* **2013**, *117*, 25290–25297.

(64) Capelli, R.; Toffanin, S.; Generali, G.; Usta, H.; Facchetti, A.; Muccini, M. *Nature Materials* **2010**, *9*, 496–503.

(65) Gedefaw, D.; Tessarolo, M.; Bolognesi, M.; Prosa, M.; Kroon, R.; Zhuang, W.; Henriksson, P.; Bini, K.; Wang, E.; Muccini, M.; Seri, M.; Andersson, M. R. *Beilstein Journal of Organic Chemistry* **2016**, *12*, 1629–1637.

(66) Aghamohammadi, M.; Fernández, A.; Schmidt, M.; Pérez-Rodríguez, A.; Goñi, A. R.; Fraxedas, J.; Sauthier, G.; Paradinas, M.; Ocal, C.; Barrena, E. *Journal of Physical Chemistry C* **2014**, *118*, 14833–14839.

(67) Lin, Y. Y.; Gundlach, D. J.; Nelson, S. F.; Jackson, T. N. *IEEE Electron Device Letters* **1997**, *18*, 606–608.

(68) Nguyen, N. N.; Jo, S. B.; Lee, S. K.; Sin, D. H.; Kang, B.; Kim, H. H.; Lee, H.; Cho, K. *Nano Letters* **2015**, *15*, 2474–2484.

(69) Tatemichi, S.; Ichikawa, M.; Kato, S.; Koyama, T.; Taniguchi, Y. *Physica Status Solidi - Rapid Research Letters* **2008**, *2*, 47–49.

(70) Kim, S. H.; Jang, M.; Yang, H.; Anthony, J. E.; Park, C. E. *Advanced Functional Materials* **2011**, *21*, 2198–2207.

(71) Laquindanum, J. G.; Katz, H. E.; Lovinger, A. J. *Journal of the American Chemical Society* **1998**, *120*, 664–672.

(72) Wang, C.; Dong, H.; Li, H.; Zhao, H.; Meng, Q.; Hu, W. *Crystal Growth and Design* **2010**, *10*, 4155–4160.

(73) Zhang, K. K.; Tan, K.; Zou, C.; Wikberg, M.; McNeil, L. E.; Mhaisalkar, S. G.; Kloc, C. *Organic Electronics: physics, materials, applications* **2010**, *11*, 1928–1934.

(74) Zeis, R.; Besnard, C.; Siegrist, T.; Schlockermann, C.; Chi, X.; Kloc, C. *Chemistry of Materials* **2006**, *18*, 244–248.

(75) Shklyarevskiy, I. O.; Jonkheijm, P.; Stutzmann, N.; Wasserberg, D.; Wondergem, H. J.; Christianen, P. C.; Schenning, A. P.; De Leeuw, D. M.; Tomović, Ž.; Wu, J.; Müllen, K.; Maan, J. C. *Journal of the American Chemical Society* **2005**, *127*, 16233–16237.

(76) Kline, R. J.; McGehee, M. D.; Kadnikova, E. N.; Liu, J.; Fréchet, J. M. J.; Toney, M. F. *Macromolecules* **2005**, *38*, 3312–3319.

(77) Zen, A.; Saphiannikova, M.; Neher, D.; Grenzer, J.; Grigorian, S.; Pietsch, U.; Asawapirom, U.; Janietz, S.; Scherf, U.; Lieberwirth, I.; Wegner, G. *Macromolecules* **2006**, *39*, 2162–2171.

(78) Keg, P.; Lohani, A.; Fichou, D.; Lam, Y. M.; Wu, Y.; Ong, B. S.; Mhaisalkar, S. G. *Macromolecular Rapid Communications* **2008**, *29*, 1197–1202.

(79) Sirringhaus, H.; Brown, P. J.; Friend, R. H.; Nielsen, M. M.; Bechgaard, K.; Langeveld-Voss, B. M. W.; Spiering, A. J. H.; Janssen, R. A. J.; Meijer, E. W.; Herwig, P.; De Leeuw, D. M. *Nature* **1999**, *401*, 685–688.

(80) Sakamoto, Y.; Suzuki, T.; Kobayashi, M.; Gao, Y.; Fukai, Y.; Inoue, Y.; Sato, F.; Tokito, S. *Journal of the American Chemical Society* **2004**, *126*, 8138–8140.

(81) Kaneda, Y.; Stawasz, M. E.; Sampson, D. L.; Parkinson, B. A. *Langmuir* **2001**, *17*, 6185–6195.

(82) Rekab, W.; Stoeckel, M. A.; El Gemayel, M.; Gobbi, M.; Orgiu, E.; Samorì, P. *ACS Applied Materials and Interfaces* **2016**, *8*, 9829–9838.

(83) Karmel, H. J.; Garramone, J. J.; Emery, J. D.; Kewalramani, S.; Bedzyk, M. J.; Hersam, M. C. *Chem. Commun.* **2014**, *50*, 8852–8855.

(84) Zykov, A.; Bommel, S.; Wolf, C.; Pithan, L.; Weber, C.; Beyer, P.; Santoro, G.; Rabe, J. P.; Kowarik, S. *Journal of Chemical Physics* **2017**, *146*, 052803.

(85) Krauss, T. N.; Barrena, E.; Zhang, X. N.; De Oteyza, D. G.; Major, J.; Dehm, V.; Würthner, F.; Cavalcanti, L. P.; Dosch, H. *Langmuir* **2008**, *24*, 12742–12744.

(86) Shukla, D.; Nelson, S. F.; Freeman, D. C.; Rajeswaran, M.; Ahearn, W. G.; Meyer, D. M.; Carey, J. T. *Chemistry of Materials* **2008**, *20*, 7486–7491.

(87) Gawrys, P.; Boudinet, D.; Zagorska, M.; Djurado, D.; Verilhac, J. M.; Horowitz, G.; Pécaud, J.; Pouget, S.; Pron, A. *Synthetic Metals* **2009**, *159*, 1478–1485.

(88) Lutsyk, P.; Janus, K.; Sworakowski, J.; Generali, G.; Capelli, R.; Muccini, M. *Journal of Physical Chemistry C* **2011**, *115*, 3105–3114.

(89) Carmen Ruiz Delgado, M.; Kim, E. G.; Da Silva Filho, D. A.; Bredas, J. L. *Journal of the American Chemical Society* **2010**, *132*, 3375–3387.

(90) Dimitrakopoulos, C. D.; Malenfant, P. R. *Advanced Materials* **2002**, *14*, 99–117.

(91) Li, M.; Marszalek, T.; Zheng, Y.; Lieberwirth, I.; Müllen, K.; Pisula, W. *ACS Nano* **2016**, *10*, 4268–4273.

(92) Rivnay, J.; Jimison, L. H.; Northrup, J. E.; Toney, M. F.; Noriega, R.; Lu, S.; Marks, T. J.; Facchetti, A.; Salleo, A. *Nature Materials* **2009**, *8*, 952–958.

(93) Molinari, A. S.; Alves, H.; Chen, Z.; Facchetti, A.; Morpurgo, A. F. *Journal of the American Chemical Society* **2009**, *131*, 2462–2463.

(94) Chen, X. K.; Fu, Y. T.; Li, H.; Bredas, J. L. *Advanced Materials Interfaces* **2014**, *1*, n/a–n/a.

(95) Choi, J.; Song, H.; Kim, N.; Kim, F. S. Development of n-type polymer semiconductors for organic field-effect transistors., 2015.

(96) Chesterfield, R. J.; McKeen, J. C.; Newman, C. R.; Ewbank, P. C.; Da Silva Filho, D. A.; Brédas, J. L.; Miller, L. L.; Mann, K. R.; Frisbie, C. D. *Journal of Physical Chemistry B* **2004**, *108*, 19281–19292.

(97) Tanida, S.; Noda, K.; Kawabata, H.; Matsushige, K. *Thin Solid Films* **2009**, *518*, 571–574.

(98) Desai, T. V.; Kish, E. R.; Woll, A. R.; Engstrom, J. R. *Journal of Physical Chemistry C* **2011**, *115*, 18221–18234.

(99) Castellanos-Gomez, A.; Vicarelli, L.; Prada, E.; Island, J. O.; Narasimha-Acharya, K. L.; Blanter, S. I.; Groenendijk, D. J.; Buscema, M.; Steele, G. A.; Alvarez, J. V.; Zandbergen, H. W.; Palacios, J. J.; Van Der Zant, H. S. J. *2D Materials* **2014**, *1*, 025001.

(100) Wang, Q. H.; Hersam, M. C. *Nature Chemistry* **2009**, *1*, 206–211.

(101) Xu, R.; Yang, J.; Zhu, Y.; Yan, H.; Pei, J.; Myint, Y. W.; Zhang, S.; Lu, Y. *Nanoscale* **2016**, *8*, 129–135.

(102) Matković, A.; Kratzer, M.; Kaufmann, B.; Vujin, J.; Gajić, R.; Teichert, C. *Scientific Reports* **2017**, *7*, 9544.

(103) Prosa, M.; Tessarolo, M.; Bolognesi, M.; Cramer, T.; Chen, Z.; Facchetti, A.; Fraboni, B.; Seri, M.; Ruani, G.; Muccini, M. *Advanced Materials Interfaces* **2016**, *3*, 1–8.

(104) Forrest, S. R. *Nature* **2004**, *428*, 911–918.

(105) Hartnett, P. E.; Timalsina, A.; Matte, H. S.S. R.; Zhou, N.; Guo, X.; Zhao, W.; Facchetti, A.; Chang, R. P. H.; Hersam, M. C.; Wasielewski, M. R.; Marks, T. J. *Journal of the American Chemical Society* **2014**, *136*, 16345–16356.

(106) Teichler, A.; Perelaer, J.; Schubert, U. S. *Journal of Materials Chemistry C* **2013**, *1*, 1910.

(107) Søndergaard, R.; Hösel, M.; Angmo, D.; Larsen-Olsen, T. T.; Krebs, F. C. *Materials Today* **2012**, *15*, 36–49.

(108) Søndergaard, R. R.; Hösel, M.; Krebs, F. C. *Journal of Polymer Science, Part B: Polymer Physics* **2013**, *51*, 16–34.

(109) Zhang, Z.; Qiu, J.; Wang, S. *Manufacturing Letters* **2016**, *8*, 6–10.

(110) Idé, J.; Méreau, R.; Ducasse, L.; Castet, F.; Olivier, Y.; Martinelli, N.; Cornil, J.; Beljonne, D. *Journal of Physical Chemistry B* **2011**, *115*, 5593–5603.

(111) Friederich, P.; Coehoorn, R.; Wenzel, W. *Chemistry of Materials* **2017**, *29*, 9528–9535.

(112) Gryn'ova, G.; Nicolaï, A.; Prlj, A.; Ollitrault, P.; Andrienko, D.; Corminboeuf, C. *J. Mater. Chem. C* **2017**, *5*, 350–361.

(113) Tea, E.; Hin, C. *Phys. Chem. Chem. Phys.* **2016**, *18*, 22706–22711.

(114) Menichetti, G.; Colle, R.; Gatti, C.; Grosso, G. *Journal of Physical Chemistry C* **2016**, *120*, 12083–12091.

(115) He, D. et al. *Nature Communications* **2014**, *5*, 5162.

(116) Coropceanu, V.; Cornil, J.; da Silva Filho, D. A.; Olivier, Y.; Silbey, R.; Brédas, J. L. *Chemical Reviews* **2007**, *107*, 926–952.

(117) Zhao, H. M.; Pfister, J.; Settels, V.; Renz, M.; Kaupp, M.; Dehm, V. C.; Würthner, F.; Fink, R. F.; Engels, B. *Journal of the American Chemical Society* **2009**, *131*, 15660–15668.

(118) Banerjee, S.; Pati, S. *Phys. Chem. Chem. Phys.* **2016**, *18*, 16345–16352.

(119) Troisi, A. *Chemical Society Reviews* **2011**, *40*, 2347.

(120) Coropceanu, V.; Li, H.; Winget, P.; Zhu, L.; Brédas, J.-L. *Annual Review of Materials Research* **2013**, *43*, 63–87.

(121) Ding, Y.; Wang, Y. *Journal of Physical Chemistry C* **2015**, *119*, 10610–10622.

(122) Vehoff, T.; Baumeier, B.; Troisi, A.; Andrienko, D. *Journal of the American Chemical Society* **2010**, *132*, 11702–11708.

(123) Cacelli, I.; Prampolini, G.; Tani, A. *The journal of physical chemistry. B* **2005**, *109*, 3531–3538.

(124) Sresht, V.; Pádua, A. A.; Blankschtein, D. *ACS Nano* **2015**, *9*, 8255–8268.

(125) Marcon, V.; Breiby, D. W.; Pisula, W.; Dahl, J.; Kirkpatrick, J.; Patwardhan, S.; Grozema, F.; Andrienko, D. *Journal of the American Chemical Society* **2009**, *131*, 11426–11432.

(126) Lorenzoni, A.; Muccini, M.; Mercuri, F. *RSC Advances* **2015**, *5*, 11797–11805.

(127) Do, K.; Ravva, M. K.; Wang, T.; Brédas, J. L. *Chemistry of Materials* **2017**, *29*, 346–354.

(128) May, F.; Marcon, V.; Hansen, M. R.; Grozema, F.; Andrienko, D. *Journal of Materials Chemistry* **2011**, *21*, 9538.

(129) Muccioli, L.; D'Avino, G.; Zannoni, C. *Advanced Materials* **2011**, *23*, 4532–4536.

(130) Zhao, Y.; Zhou, Q.; Li, Q.; Yao, X.; Wang, J. *Adv. Mater.* **2017**, *29*, 1603990.

(131) Zhao, Y.; Wang, J. *Journal of Physical Chemistry C* **2017**, *121*, 4488–4495.

(132) Yoneya, M.; Minemawari, H.; Yamada, T.; Hasegawa, T. *Journal of Physical Chemistry C* **2017**, *121*, 8796–8803.

(133) Han, G.; Shen, X.; Yi, Y. *Advanced Materials Interfaces* **2015**, *2*, 1–8.

(134) Roscioni, O. M.; Muccioli, L.; Della Valle, R. G.; Pizzirusso, A.; Ricci, M.; Zannoni, C. *Langmuir* **2013**, *29*, 8950–8958.

(135) Yu, Y. J.; Lee, G. H.; Choi, J. I.; Shim, Y. S.; Lee, C. H.; Kang, S. J.; Lee, S.; Rim, K. T.; Flynn, G. W.; Hone, J.; Kim, Y. H.; Kim, P.; Nuckolls, C.; Ahn, S. *Advanced Materials* **2017**, *29*, 1–7.

(136) Svatek, S. A.; Scott, O. R.; Rivett, J. P. H.; Wright, K.; Baldoni, M.; Bichoutskaia, E.; Taniguchi, T.; Watanabe, K.; Marsden, A. J.; Wilson, N. R.; Beton, P. H. *Nano Letters* **2015**, *15*, 159–164.

(137) Korolkov, V. V.; Baldoni, M.; Watanabe, K.; Taniguchi, T.; Besley, E.; Beton, P. H. *Nature Chemistry* **2017**, *9*, 1191–1197.

(138) Berardi, R.; Micheletti, D.; Muccioli, L.; Ricci, M.; Zannoni, C. *Journal of Chemical Physics* **2004**, *121*, 9123–9130.

(139) Berardi, R.; Muccioli, L.; Orlandi, S.; Ricci, M.; Zannoni, C. *Chemical Physics Letters* **2004**, *389*, 373–378.

(140) Lamarra, M.; Muccioli, L.; Orlandi, S.; Zannoni, C. *Physical Chemistry Chemical Physics* **2012**, *14*, 5368.

(141) Rossi, G.; Monticelli, L.; Puisto, S. R.; Vattulainen, I.; Ala-Nissila, T. *Soft Matter* **2011**, *7*, 698–708.

(142) Alessandri, R.; Uusitalo, J. J.; De Vries, A. H.; Havenith, R. W.; Marrink, S. J. *Journal of the American Chemical Society* **2017**, *139*, 3697–3705.

(143) Izvekov, S.; Voth, G. A. *Journal of Physical Chemistry B* **2005**, *109*, 2469–2473.

(144) Bayramoglu, B.; Faller, R. *Macromolecules* **2012**, *45*, 9205–9219.

(145) Zannoni, C.; Fisica, C.; Risorgimento, V. *J. Mater. Chem.* **2001**, *11*, 2637–2646.

(146) Melucci, M.; Zambianchi, M.; Favaretto, L.; Gazzano, M.; Zanelli, A.; Monari, M.; Capelli, R.; Troisi, S.; Toffanin, S.; Muccini, M. *Chemical Communications* **2011**, *47*, 11840–11842.

(147) Bonetti, S. et al. *J. Mater. Chem. B* **2016**, *4*, 2921–2932.

(148) Kordt, P.; Stodtmann, S.; Badinski, A.; Al Helwi, M.; Lennartz, C.; Andrienko, D. *Phys. Chem. Chem. Phys.* **2015**, *17*, 22778–22783.

(149) Dionigi, C.; Posati, T.; Benfenati, V.; Sagnella, A.; Pistone, A.; Bonetti, S.; Ruani, G.; Dinelli, F.; Padeletti, G.; Zamboni, R.; Muccini, M. *Journal of Materials Chemistry B* **2014**, *2*, 1424–1431.

(150) Wang, C.-H.; Hsieh, C.-Y.; Hwang, J.-C. *Advanced Materials* **2011**, *23*, 1630–1634.

(151) Brandrup, J.; Immergut, E.; Grulke, E.; Abe, A.; Bloch, D., *Polymer Handbook, 4th ed.* 2005.

(152) Walsh, A.; Catlow, C. R. A. *Journal of Materials Chemistry* **2010**, *20*, 10438.

(153) Warschkow, O.; Ellis, D. E.; Gonzalez, G. B.; Mason, T. O. *Journal of the American Ceramic Society* **2003**, *86*, 1700–1706.

(154) Park, H.; Rowehl, J. A.; Kim, K. K.; Bulovic, V.; Kong, J. *Nanotechnology* **2010**, *21*, 505204.

(155) Lee, W. H.; Park, J.; Sim, S. H.; Lim, S.; Kim, K. S.; Hong, B. H.; Cho, K. *Journal of the American Chemical Society* **2011**, *133*, 4447–4454.

(156) Macleod, J. M.; Rosei, F. *Small* **2014**, *10*, 1038–1049.

(157) Gaberle, J.; Gao, D. Z.; Shluger, A. L.; Amrous, A.; Bocquet, F.; Nony, L.; Para, F.; Loppacher, C.; Lamare, S.; Cherioux, F. *Journal of Physical Chemistry C* **2017**, *121*, 4393–4403.

(158) Eswaraiah, V.; Zeng, Q.; Long, Y.; Liu, Z. *Small* **2016**, *12*, 3480–3502.

(159) Akhtar, M.; Anderson, G.; Zhao, R.; Alruqi, A.; Mroczkowska, J. E.; Sumanasekera, G.; Jasinski, J. B. *npj 2D Materials and Applications* **2017**, *1*, 5.

(160) Liu, H.; Neal, A. T.; Zhu, Z.; Luo, Z.; Xu, X.; Tománek, D.; Ye, P. D. *ACS Nano* **2014**, *8*, 4033–4041.

(161) Qiao, J.; Kong, X.; Hu, Z. X.; Yang, F.; Ji, W. *Nature Communications* **2014**, *5*, 4475.

(162) Zhu, W.; Park, S.; Yogeesh, M. N.; McNicholas, K. M.; Bank, S. R.; Akinwande, D. *Nano Letters* **2016**, *16*, 2301–2306.

(163) Zhang, Y.-Y.; Pei, Q.-X.; Jiang, J.-W.; Wei, N.; Zhang, Y.-W. *Nanoscale* **2016**, *8*, 483–491.

(164) Carvalho, A.; Wang, M.; Zhu, X.; Rodin, A. S.; Su, H.; Castro Neto, A. H. *Nature Reviews Materials* **2016**, *1*, 16061.

(165) Kistanov, A. A.; Cai, Y.; Zhou, K.; Dmitriev, S. V.; Zhang, Y. W. *Journal of Physical Chemistry C* **2016**, *120*, 6876–6884.

(166) Warschauer, D. *Journal of Applied Physics* **1963**, *34*, 1853–1860.

(167) Du, Y.; Liu, H.; Deng, Y.; Ye, P. D. *ACS Nano* **2014**, *8*, 10035–10042.

(168) Li, L.; Yu, Y.; Ye, G. J.; Ge, Q.; Ou, X.; Wu, H.; Feng, D.; Chen, X. H.; Zhang, Y. *Nature Nanotechnology* **2014**, *9*, 372–377.

(169) Das, S.; Demarteau, M.; Roelofs, A. *ACS Nano* **2014**, *8*, 11730–11738.

(170) Kim, J. S.; Liu, Y.; Zhu, W.; Kim, S.; Wu, D.; Tao, L.; Dodabalapur, A.; Lai, K.; Akinwande, D. *Scientific Reports* **2015**, *5*, 8989.

(171) Illarionov, Y. Y.; Waltl, M.; Rzepa, G.; Kim, J. S.; Kim, S.; Dodabalapur, A.; Akinwande, D.; Grasser, T. *ACS Nano* **2016**, *10*, 9543–9549.

(172) Schrödinger, E. *Physical Review* **1926**, *28*, 1049–1070.

(173) Born, M.; Oppenheimer, R. *Annalen der Physik* **1927**, *389*, 457–484.

(174) Soler, J. M.; Artacho, E.; Gale, J. D.; García, A.; Junquera, J.; Ordejón, P.; Sánchez-Portal, D. *Journal of Physics Condensed Matter* **2002**, *14*, 2745–2779.

(175) Dovesi, R; Orlando, R; Civalleri, B; Roetti, C; Saunders, V. R.; Zicovich-Wilson, C. M. *Zeitschrift fur Kristallographie* **2005**, *220*, 571–573.

(176) Dovesi, R.; Saunders, V. R.; Roetti, C.; Orlando, R.; Zicovich-Wilson, C. M.; Pascale, F.; Civalleri, B.; Doll, K.; Harrison, N. M.; Bush, I. J.; D'Arco, P.; Llunell, M., *CRYSTAL09 User's Manual (University of Torino, Torino, 2009)*, 2009.

(177) Te Velde, G.; Bickelhaupt, F. M.; Baerends, E. J.; Fonseca Guerra, C.; van Gisbergen, S. J.; Snijders, J. G.; Ziegler, T. *Journal of Computational Chemistry* **2001**, *22*, 931–967.

(178) Giannozzi, P. et al. *Journal of Physics Condensed Matter* **2009**, *21*, 395502.

(179) Superzeure, E. X.; Superieure, E. X. *Physical Review* **1964**, *136*, 864.

(180) Kohn, W.; Sham, L. J. *Physical Review* **1965**, *140*, 1133.

(181) Stephens, P. J.; Devlin, F. J.; Chabalowski, C. F.; Frisch, M. J. *The Journal of Physical Chemistry* **1994**, *98*, 11623–11627.

(182) Kim, K.; Jordan, K. D. *The Journal of Physical Chemistry* **1994**, *98*, 10089–10094.

(183) Van Der Spoel, D.; Lindahl, E.; Hess, B.; Groenhof, G.; Mark, A. E.; Berendsen, H. J. *Journal of Computational Chemistry* **2005**, *26*, 1701–1718.

(184) Crane, M.; Boga, D., *A commentary: Rethinking approaches to resilience and mental health training*; 1; Sandia Corporation: 2017; Vol. 25, pp 30–33.

(185) Nosé, S. *The Journal of Chemical Physics* **1984**, *81*, 511–519.

(186) Hoover, W. G. *Physical Review A* **1985**, *31*, 1695–1697.

(187) Parrinello, M.; Rahman, A. *Physical Review Letters* **1980**, *45*, 1196–1199.

(188) Allen, M. P.; Tildesley, D. J., *Computer simulation of liquids*, 1989.

(189) Buckingham, R. A. *Proceedings of the Royal Society A: Mathematical, Physical and Engineering Sciences* **1938**, *168*, 264–283.

(190) Darden, T.; York, D.; Pedersen, L. *The Journal of Chemical Physics* **1993**, *98*, 10089–10092.

(191) Tozzini, V. *Current Opinion in Structural Biology* **2005**, *15*, 144–150.

(192) Gay, J. G.; Berne, B. J. *The Journal of Chemical Physics* **1981**, *74*, 3316–3319.

(193) Van Speybroeck, V.; De Wispelaere, K.; Van der Mynsbrugge, J.; Vandichel, M.; Hemelsoet, K.; Waroquier, M. *Chem. Soc. Rev.* **2014**, *43*, 7326–7357.

(194) Barducci, A.; Bonomi, M.; Parrinello, M. *Wiley Interdisciplinary Reviews: Computational Molecular Science* **2011**, *1*, 826–843.

(195) Zykova-Timan, T.; Raitei, P.; Parrinello, M. *Journal of Physical Chemistry B* **2008**, *112*, 13231–13237.

(196) Tribello, G. A.; Bonomi, M.; Branduardi, D.; Camilloni, C.; Bussi, G. *Computer Physics Communications* **2014**, *185*, 604–613.

(197) Koopmans, T *Physica* **1934**, *1*, 104 –113.

(198) Jeon, H. G.; Oguma, N.; Hirata, N.; Ichikawa, M. *Organic Electronics: physics, materials, applications* **2013**, *14*, 19–25.

(199) Rolin, C.; Vasseur, K.; Schols, S.; Jouk, M.; Duhoux, G.; Müller, R.; Genoe, J.; Heremans, P. *Applied Physics Letters* **2008**, *93*, 033305.

(200) Wan, a. S.; Kushto, G. P.; Mäkinen, a. J. *Journal of Vacuum Science & Technology A: Vacuum, Surfaces, and Films* **2010**, *28*, 1275.

(201) Wan, A. S.; Long, J. P.; Kushto, G.; Mäkinen, A. J. *Chemical Physics Letters* **2008**, *463*, 72–77.

(202) Puigdollers, J.; Della Pirriera, M.; Marsal, A.; Orpella, A.; Cheylan, S.; Voz, C.; Alcubilla, R. *Thin Solid Films* **2009**, *517*, 6271–6274.

(203) Zhang, Y.; Seo, H. S.; An, M. J.; Choi, J. H. *Organic Electronics: physics, materials, applications* **2009**, *10*, 895–900.

(204) Struijk, C. W.; Sieval, A. B.; Dakhorst, J. E.; Van Dijk, M.; Kimkes, P.; Koehorst, R. B.; Donker, H.; Schaafsma, T. J.; Picken, S. J.; Van de Craats, A. M.; Warman, J. M.; Zuilhof, H.; Sudholter, E. J. *Journal of the American Chemical Society* **2000**, *122*, 11057–11066.

(205) Kistler, K. A.; Pochas, C. M.; Yamagata, H.; Matsika, S.; Spano, F. C. *Journal of Physical Chemistry B* **2012**, *116*, 77–86.

(206) Schmidt, R.; Oh, J. H.; Sun, Y. S.; Deppisch, M.; Krause, A. M.; Radacki, K.; Braunschweig, H.; Könemann, M.; Erk, P.; Bao, Z.; Würthner, F. *Journal of the American Chemical Society* **2009**, *131*, 6215–6228.

(207) Briseno, A. L.; Mannsfeld, S. C. B.; Reese, C.; Hancock, J. M.; Xiong, Y.; Jenekhe, S. A.; Bao, Z.; Xia, Y. *Nano Letters* **2007**, *7*, 2847–2853.

(208) Mercuri, F.; Costa, D.; Marcus, P. *Journal of Physical Chemistry C* **2009**, *113*, 5228–5237.

(209) Becke, A. D. *The Journal of Chemical Physics* **1993**, *98*, 5648–5652.

(210) Lee, C; Yang, W; Parr, R. *Phys Rev B* **1988**, *37*, 785–789.

(211) Corno, M.; Busco, C.; Civalleri, B.; Ugliengo, P. *Physical Chemistry Chemical Physics* **2006**, *8*, 2464.

(212) Becke, A. D.; Edgecombe, K. E. *The Journal of Chemical Physics* **1990**, *92*, 5397–5403.

(213) Spackman, M. a.; Mitchell, A. S. *Physical Chemistry Chemical Physics* **2001**, *3*, 1518–1523.

(214) Truhlar, D. G. *Journal of computational chemistry* **2009**, *28*, 73–86.

(215) Roh, J.; Lee, J.; Kang, C. M.; Lee, C.; Jun Jung, B. *Physica Status Solidi - Rapid Research Letters* **2013**, *7*, 469–472.

(216) Balakrishnan, K.; Datar, A.; Naddo, T.; Huang, J.; Oitker, R.; Yen, M.; Zhao, J.; Zang, L. *Journal of the American Chemical Society* **2006**, *128*, 7390–7398.

(217) Perdew, J. P.; Chevary, J. A.; Vosko, S. H.; Jackson, K. A.; Pederson, M. R.; Singh, D. J.; Fiolhais, C. *Physical Review B* **1992**, *46*, 6671–6687.

(218) Meng, Q.; Dong, H.; Hu, W.; Zhu, D. *Journal of Materials Chemistry* **2011**, *21*, 11708.

(219) Lorenzoni, A.; Mercuri, F.; Querciagrossa, L.; Zannoni, C. *to be published* **2018**.

(220) Roscioni, O. M.; Ricci, M.; Querciagrossa, L.; Zannoni, C. *to be published* **2018**.

(221) Lechner, C.; Sax, A. F. *Journal of Physical Chemistry C* **2014**, *118*, 20970–20981.

(222) De Oliveira, I. S.; Miwa, R. H. *Journal of Chemical Physics* **2015**, *142*, 044301.

(223) Jo, G.; Choe, M.; Lee, S.; Park, W.; Kahng, Y. H.; Lee, T. *Nanotechnology* **2012**, *23*, 112001.

(224) Allen, M. J.; Tung, V. C.; Kaner, R. B. *Chemical reviews* **2010**, *110*, 132–45.

(225) Wang, Q. H.; Hersam, M. C. *Nano Letters* **2011**, *11*, 589–593.

(226) Jorgensen, W. L.; Maxwell, D. S.; Tirado-Rives, J. *Journal of the American Chemical Society* **1996**, *118*, 11225–11236.

(227) Wang, Q.; Aziz, H. *ACS Applied Materials and Interfaces* **2013**, *5*, 8733–8739.

(228) Cottaar, J.; Coehoorn, R.; Bobbert, P. *Organic Electronics* **2012**, *13*, 667–672.

(229) Rosen, J.; Warschkow, O. *Physical Review B - Condensed Matter and Materials Physics* **2009**, *80*, 1–10.

(230) González, G. B.; Cohen, J. B.; Hwang, J.-H.; Mason, T. O.; Hodges, J. P.; Jorgensen, J. D. *Journal of Applied Physics* **2001**, *89*, 2550–2555.

(231) Marezio, M. *Acta Crystallographica* **1966**, *20*, 723–728.

(232) Troullier, N.; Martins, J. L. *Physical Review B* **1991**, *43*, 8861–8869.

(233) Walsh, A.; Da Silva, J. L. F.; Wei, S. H.; Körber, C.; Klein, A.; Piper, L. F. J.; Demasi, A.; Smith, K. E.; Panaccione, G.; Torelli, P.; Payne, D. J.; Bourlange, A.; Egdell, R. G. *Physical Review Letters* **2008**, *100*, 2–5.

(234) Koenig, S. P.; Doganov, R. A.; Schmidt, H.; Castro Neto, A. H.; Özyilmaz, B. *Applied Physics Letters* **2014**, *104*, 103106.

(235) Das, S.; Zhang, W.; Demarteau, M.; Hoffmann, A.; Dubey, M.; Roelofs, A. *Nano Letters* **2014**, *14*, 5733–5739.

(236) Hutter, J.; Iannuzzi, M.; Schiffmann, F.; Vandevondele, J. *Wiley Interdisciplinary Reviews: Computational Molecular Science* **2014**, *4*, 15–25.

(237) Bridgman, P. W. *Journal of the American Chemical Society* **1914**, *36*, 1344–1363.

(238) Kumar, P.; Bhadoria, B. S.; Kumar, S.; Bhowmick, S.; Chauhan, Y. S.; Agarwal, A. *Physical Review B* **2016**, *93*, 195428.

(239) Vandevondele, J.; Krack, M.; Mohamed, F.; Parrinello, M.; Chassaing, T.; Hutter, J. *Computer Physics Communications* **2005**, *167*, 103–128.

(240) Lippert, G.; Hutter, J.; Parrinello, M. *Mol. Phys.* **1997**, *92*, 477–487.

(241) VandeVondele, J.; Hutter, J. *Journal of Chemical Physics* **2007**, *127*, 114105.

(242) Hartwigsen, C; Goedecker, S; Hutter, J *Physical Review B* **1998**, *58*, 3641.

(243) Krack, M. *Theoretical Chemistry Accounts* **2005**, *114*, 145–152.

(244) Goedecker, S.; Teter, M.; Hutter, J. *Physical Review B* **1996**, *54*, 1703–1710.

(245) Rühle, V.; Junghans, C.; Lukyanov, A.; Kremer, K.; Andrienko, D. *Journal of Chemical Theory and Computation* **2009**, *5*, 3211–3223.